POLITECNICO
MILANO 1863

SCUOLA DI INGEGNERIA INDUSTRIALE
E DELL'INFORMAZIONE

Nonlinear modeling and control of coaxial rotor UAVs with application to the Mars helicopter

Tesi di Laurea Magistrale in
Space Engineering - Ingegneria Spaziale

Author: **Marcello Sparasci**

Student ID: 953260
Advisor: Prof. Davide Invernizzi
Co-advisors: Prof. Mauro Massari
Academic Year: 2021/2022

Abstract

The Red Planet has been on top in the priority list of interplanetary exploration of the solar system. The Mars exploration landers and rovers have laid the foundation of our understanding of the planet atmosphere and terrain. Although the rovers have been a great help, they also have limitations in terms of their speed and exploration capabilities from the ground. Robotic planetary aerial vehicles increase the range of terrain that can be examined, compared to traditional landers and rovers, and have more near-surface capability than orbiters. Aerial mobility is a promising possibility for planetary exploration as it reduces the challenges that difficult obstacles pose to ground vehicles. The Ingenuity Mars helicopter has been designed by NASA's Jet Propulsion Laboratory to test the technical demonstration of aerial flight in the thin atmosphere of Mars. The first purpose of this thesis is to replicate Mars helicopter dynamics, building a simplified mathematical model suitable for control design based on available literature about Ingenuity and existing approaches for the modeling of small terrestrial coaxial helicopters. The second aim of this project is to develop a nonlinear control law to improve the operative range of this kind of UAVs with respect to existing control designs, which are mostly based on linear control approaches. The thesis starts with a brief introduction to the challenges encountered by the development of a Mars helicopter and then proceeds with an overview of the design of Ingenuity aiming to investigate its main components and to highlight its working principles. In the second chapter, the procedure developed to obtain a sufficiently accurate nonlinear model of the Mars helicopter, which mixes first-principle modeling and identification experiments, is discussed. In the third chapter, the control system is developed starting with the presentation of the baseline control architecture implemented in Ingenuity and following with the development of the proposed nonlinear controller. The results of numerical simulations are shown in the last chapter underling the benefits derived from the implementation of a nonlinear control system when the helicopter operates far from its hovering point.

Keywords: Ingenuity, Mars, helicopter, UAV, dynamics, control

Abstract in lingua italiana

Marte è da sempre in cima alla lista di priorità per l'esplorazione interplanetaria del nostro sistema solare. I lander e i rover per l'esplorazione di Marte hanno gettato le basi per la nostra comprensione dell'atmosfera e della superficie del pianeta. Sebbene i rover siano stati di grande aiuto, essi hanno limitazioni in termini di velocità e di capacità esplorativa. L'introduzione di veivoli per l'esplorazione marziana aumenterebbe la portata del terreno che può essere esaminata rispetto ai tradizionali rover, dando allo stesso tempo la possibilità di osservare più da vicino, e di conseguenza più nel dettaglio, la superficie di un pianeta rispetto a un satellite orbitale. Lo sviluppo di droni capaci di volare al di fuori dell'atmosfera terrestre rappresenterebbe perciò una possibilità promettente per migliorare l'esplorazione planetaria e permetterebbe di ridurre le sfide correlate alla presenza di ostacoli del terreno. L'elicottero Ingenuity è stato progettato dal Jet Propulsion Laboratory della NASA per testare il volo aereo nella sottile atmosfera di Marte. Il primo scopo di questa tesi è quello di replicare la dinamica dell'elicottero marziano, costruendo un modello matematico semplificato adatto al design di controllo basato sulla letteratura disponibile su Ingenuity e sugli approcci esistenti per la modellazione di piccoli elicotteri terrestri a rotori coassiali. Il secondo obiettivo di questo progetto è sviluppare una legge di controllo non lineare per migliorare il range operativo di questo tipo di UAV rispetto a design di controllo già esistenti, i quali per la maggior parte sono basati su approcci di controllo lineare. La tesi inizia con una breve introduzione sulle sfide incontrate nello sviluppo di un elicottero marziano e con una descrizione generale del design di Ingenuity con l'obiettivo di identificarne i componenti principali e di evidenziarne i principi di funzionamento. Nel secondo capitolo, è discussa la procedura sviluppata per ottenere un modello non lineare sufficientemente accurato dell' elicottero marziano, basandosi su una modellazione di primo principio e su esperimenti identificativi. Nel terzo capitolo, il sistema di controllo viene sviluppato a partire dall' architettura di controllo implementata da Ingenuity e a seguire dallo sviluppo del controllore non lineare proposto. I risultati delle simulazioni numeriche effettuate sono mostrate nell'ultimo capitolo sottolineando i benefici che derivano dall'implementazione di un sistema di controllo non lineare quando l'elicottero opera lontano dal suo punto di equilibrio.

Parole chiave: Ingenuity, Marte, elicottero, UAV, dinamica, controllo

Contents

Introduction

The idea of exploration fulfils human curiosity in order to find answers to the science mysteries present in the Universe.
The question that has been pursued over many years now is: how did life evolve in our solar system, and other than Earth where else life could have existed in the early days of our solar system formation? These questions lead us to identifying the habitable zone of our solar system and the planets that fall under this habitable zone. Earth and Mars are prime candidates for satisfying the criteria defined to be in the habitable zone of the solar system.
For many years now we have been sending unmanned robotic probes, orbiters, landers and rovers to the red planet Mars in order to understand its composition, atmosphere, geology etc. There have been over 45 missions that were targeted to Mars by collective effort from different space agencies from around the world.
The unmanned robotic missions are great at exploring the Red Planet while also surviving the harsh atmosphere environment and radiation dose. The robotic exploration has paved the way for humanity to research technology that supports human settlement on Mars. The rovers Spirit and Opportunity have led a foundation for developing technology to send robust and autonomous systems to conduct experiments on Mars.
The orbiters have mapped the surface of the planet with great detail that helps space agencies in selecting landing sites of future missions in order to define mission objectives, and also to have knowledge about the environment in which the lander or rover will be performing experiments. The orbiters like Mars Reconnaissance Orbiter (MRO) and Mars Express have mapped the interesting regions of the planet like Volcanoes, Canyons and polar ice caps. Even after using the best quality Hires Images from MRO, the surface has only been mapped with resolution of about 20 m per pixel.
For this purpose the rovers have been designed and sent to Mars in order to partially fill the data gaps from the orbiters. The rovers have been successful in doing onsite research about mineral composition of rocks and soil, atmospheric studies along with sending beautiful panoramic mosaics of the red planet.
The problem is that the rovers are still limited by their ability to move quickly from one

site to another site of interest in order to conduct science experiments.

A. Motivation

The limitation posed by ground based exploration vehicles are a constraint to going further on the Red Planet. In order to overcome this limitation, the idea of aerial exploration has been considered for many years and many methods have been proposed to go a step further by changing the mode of exploration.
Aerial exploration is great at moving from point A to point B without considerations about the terrain and ground obstacles. Aerial exploration also allows for movement at higher speeds from one site to another site of interest.
There have been many ideas and theories that propose modes of transport that consider flying or hovering vehicles.
Among many projects considered for developing multi rotor systems to fly on Mars, the project that has been an inspiration to this master thesis is the Ingenuity Mars helicopter project.
The Mars helicopter is a small, lightweight helicopter that has been designed and tested by NASA's Jet Propulsion Laboratory in a simulated environment that represent atmosphere, density, pressure and gravity in Mars-like conditions.
The technological demonstration about making the first powered flight in the Mars atmosphere from the Ingenuity helicopter builds a foundation the development autonomous control for rotorcrafts for space purposes and also lead to a significant amount of research in order to develop thin airfoil aerodynamics analysis that focuses on low Reynolds number flow.

B. Challenges of Mars helicopter flight

Like any spacecraft or spacecraft instrument, a helicopter designed for Mars faces a host of challenging requirements not typically seen on Earth: it must withstand high structural loads during launch, extreme temperature variations, high levels of radiation, and be vacuum compatible; it must satisfy contamination requirements related to planetary protection; and it must operate entirely without physical intervention after launch. It must also be compact and safely deployable after landing.
In this work, the most important set of challenges taken under consideration are those related to the flight dynamics of the vehicle when operating in the Martian environment, and how these affect the mechanical design of the vehicle and the flight control algorithms.
Two aspects of the environment are primary drivers for the flight dynamics of a helicopter

on Mars:

1. The Martian atmosphere consists primarily of carbon dioxide (CO_2) at only $1-2\%$ of Earth's atmospheric density at sea level, which is equivalent to altitudes around 100.000 ft on Earth.

2. The Martian gravity is approximately 38% of Earth's gravity.

The most obvious effect of the reduced density is a reduction in lift capability for any given rotor.
The reduced gravity, although helpful, does not nearly make up for this reduction in lift. Beyond this, the Martian environment also influences the helicopter flight dynamics in less obvious but highly consequential ways, which ultimately influence both the design of the helicopter itself and the algorithms used to control it.
Designing a helicopter for Mars also presents serious challenges in terms of testing, verification, and validation. It is not possible to fully replicate the Mars environment on Earth; this forces a greater reliance on analysis, modeling, and simulation, combined with limited testing in partially replicated environments.

C. Contributions of thesis

This master thesis focuses on the flight dynamics and control design of the Mars Helicopter; in particular, the following factors are covered specifically:

1. The derivation of a nonlinear dynamic model of the Mars Helicopter suitable for simulation purposes and the preliminary validation of nonlinear control laws by combining first-principle modeling and relying on data found in Ingenuity's scientific papers and adapting existing mathematical models of terrestrial coaxial helicopters similar in structure, actuation and control.

2. The derivation of a suitable nonlinear control-oriented model that accounts for the main nonlinear effects, in particular those associated with the rigid body kinematics and the input coupling.

3. The design of a nonlinear control system, choosing a proper control architecture, designing P/PID controllers and simulating the model in SIMULINK to follow autonomously different trajectories.

The thesis is structured as presented here:

- In the first chapter, a brief introduction to the design of Ingenuity is presented aiming to investigate its main components and to highlight its working principles.

- In the second chapter, the procedure developed to obtain a sufficiently accurate nonlinear model of the Mars helicopter, which mixes first-principle modeling and identification experiments, is discussed giving particular attention to rotor dynamics.
- In the third chapter, the control system is developed starting with the presentation of the baseline control architecture implemented in Ingenuity and following with the development of the proposed nonlinear controller.
- In the fourth chapter, the nonlinear control law adopted has been tested carrying out numerical simulations of the system underling the difference with the baseline control architecture and verifying the performances of the controller for complex trajectories.
- In the last part some conclusions are derived from the presented analysis and a proposal for further developments is explained.

1 | Vehicle overview

Before modelling the flight dynamics of the vehicle, it is necessary first to have a detail description of the components of the Mars Helicopter and a clear knowledge of how it works.
Ingenuity is a small robotic coaxial rotor helicopter operating on Mars as part of NASA's Mars 2020 mission along with the Perseverance rover.
Its rotors measure 1.21 m and its entire body is 0.49 m tall, with a dry mass of 1.8 kg [2].
The helicopter is built around a central mast - a hollow structural tube that runs from the top of the helicopter to the bottom. Within this tube are the wires from the Electronics Core Module (ECM) to the propulsion motor and servo elements, as well as to the host spacecraft.
The mast tube is designed to be stiff so as to minimize control interactions, as well as have low thermal conductivity to minimize thermal leakage into the ECM.
Attached to the mast are (ordered from top to bottom):

1. **Upper Launch Lock**: this attaches the helicopter to the host spacecraft prior to deployment onto the surface. Attached to the launch lock are deployment devices, wires to provide power and communications prior to deployment, and separation connectors to cleanly disconnect electrical lines upon deployment.

2. **Solar Panel**: the solar panel is made from Inverted Metamorphic (IMM4J) cells from SolAero Technologies. The cells are optimized for the Mars solar spectrum and occupy a rectangular area with 680 cm^2 of substrate (544 cm^2 active cell area) in a region centered and immediately above the co-axial rotors. It provides the recharge of the batteries and minimally interferes with the flow through the rotor.

3. **Upper & Lower Rotors**: the rotor hubs are attached to the mast and includes the various non-rotating elements such as the servos, the non-rotating portion of the swashplate, the rotor windings, and the rotor power electronics.

4. **Landing Gear Mounting Plate**: this consists of a plate to which are connected four light-weight legs.

5. **Fuselage - Warm Electronics Box**: the fuselage consists of a very lightweight structural frame to hold the thermal skin of the helicopter, and the 30 mm gap insulation between the skin and the ECM.
6. **ECM Assembly**: the ECM is mounted onto the mast and consists of the battery, the Battery Interface Board (BIB), and electronics circuits board for the avionics.
7. **Upper Sensor Assembly**: this consists of an inclinometer, IMU and associated vibration isolation elements mounted on the mast as close to the center-of-mass of the vehicle (to minimize the effects of angular rates and accelerations). **The Lower Sensor Assembly** (consisting of an altimeter, cameras and a secondary IMU) is mounted directly onto the ECM and not onto the mast.
8. **Lower Launch Lock**: this holds the helicopter to the host spacecraft on the other end prior to deployment.

The final design is represented in Fig. 1.1 and some of its features are now discussed in more detail.

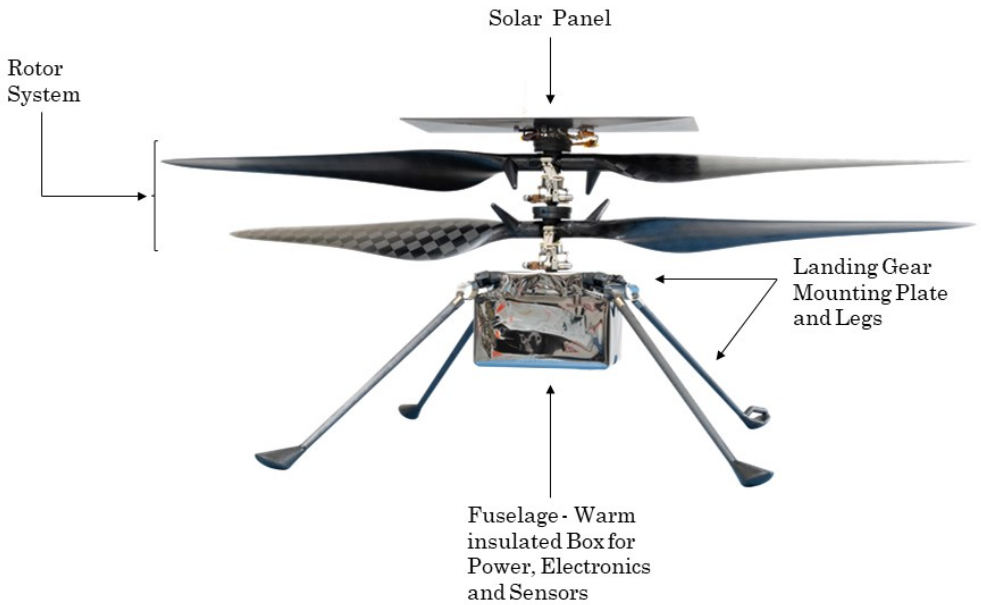

Figure 1.1: Ingenuity 3D model

1.1. Rotor system

The Mars Helicopter design features a coaxial rotor with two counter-rotating hingeless two-bladed rotors measuring 1.21 m in diameter, which are spaced apart by approximately 8% of the rotor diameter. The coaxial rotor configuration was chosen early on, with accommodation constraints on the host spacecraft as the main driver.
The rotor system provides lift for the helicopter as well as forces required for the directional control of its trajectory.
There are swashplates on both the upper and lower rotor, each with collective and cyclic control. The collective angle can range from $-4.5°$ to $17.5°$ and the cyclic angle has a range of $\pm 10°$.
The maximum rotation rate for the rotors is 2800 rpm. The speed is fixed for the duration of flight, depending primarily on the atmospheric density.
Seals around bearings and a soft boot around the swashplate assembly mitigate against dust in the Mars atmosphere.
Actuator power electronics are co-located with each actuator, and the motors self-heat before flight.
The rotors are actuated with a custom 46 pole brushless motor with solenoid wound teeth using rectangular copper wire.
Three Maxon brushed DC motors (DCX10) operating through a 4-stage gear-box control the height and tilt of each swashplate. Chinese weights provide a restoring force on the blade moments when under centrifugal loads thereby reducing the torque requirements on the swashplate actuators.
The rotor is shown in Fig. 1.2 and is fabricated from carbon fiber composites for most of the primary structure.
In Table 1.1, the numerical values of some key Ingenuity rotor parameters are reported.

Parameter	**Physical meaning**
$N_b = 2$	Number of blades per rotor
$l_{low} = 0.09\ m$	Distance of the lower rotor hub from Ingenuity CG
$R = 0.605\ m$	Rotor disk radius
$A = 1.150\ m^2$	Rotor disk area
$\Omega \approx 272\ rad/s$	Rotational Speed of Rotor (at atmospheric density, $\rho = 0.0175$ kg/m^3)
$\sigma = 0.148$	Rotor Solidity

Table 1.1: Rotor parameters [6]

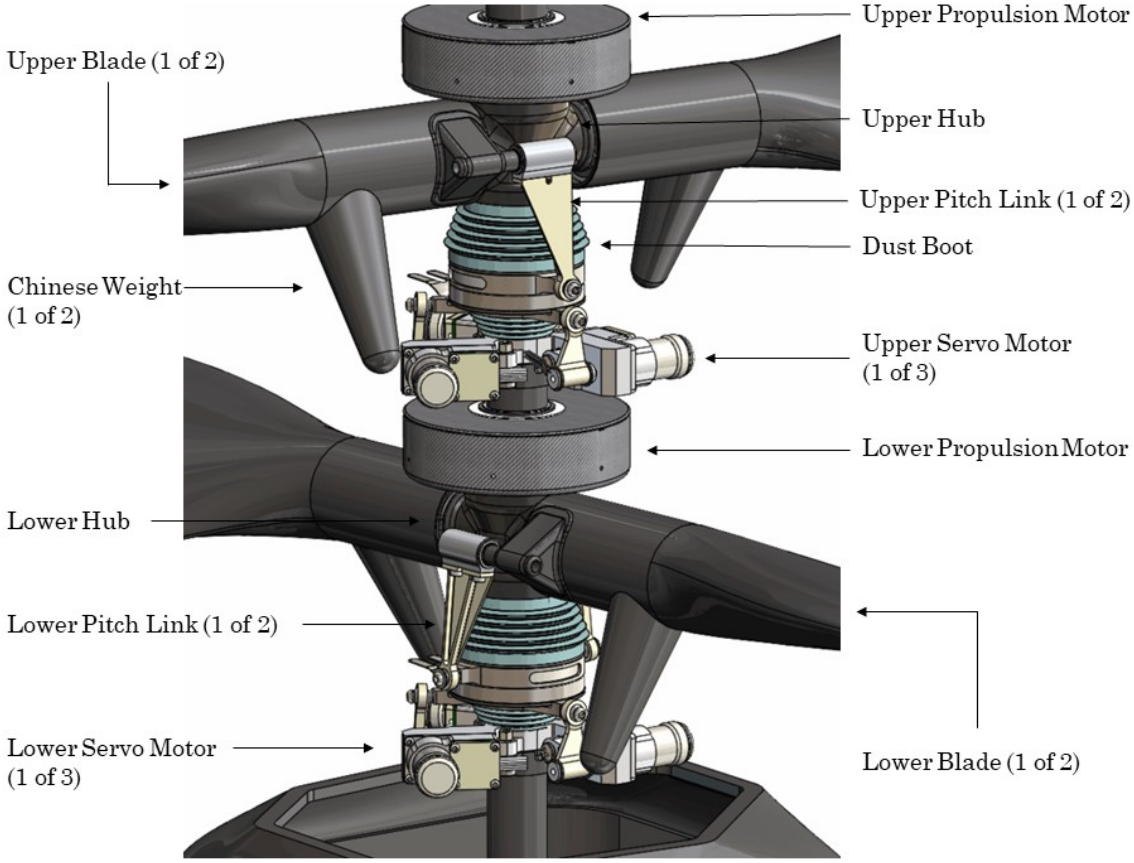

Figure 1.2: Ingenuity rotor system

1.1.1. Rotor blades

The low density Martian atmosphere and the relatively small Mars Helicopter rotors result in very low chord-based Reynolds number flows over a range of $Re_c \approx 10^3$ to 10^4. Furthermore, the low density and low Reynolds number reduce the lifting force and lifting efficiency, respectively, which are only marginally compensated by a lower gravitational acceleration.

In addition, the low temperature and largely CO_2 based atmosphere result in a low speed of sound, further constraining rotor operation in the Martian atmosphere by increasing compressibility effects.

All these issues represented a great challenge in the selection of proper airfoil sections for the rotor blades.

A series of thin laminar flow airfoils was developed for the extremely low Reynolds number operating conditions experienced by the Mars Helicopter rotor.

The CLF5605 airfoil used for the outboard portion of the blade was based on an airfoil used on other propellers designed by Aerovironment, with the camber line modified for

operation at higher lift coefficients (see Figs. 1.3 and 1.4) [10].

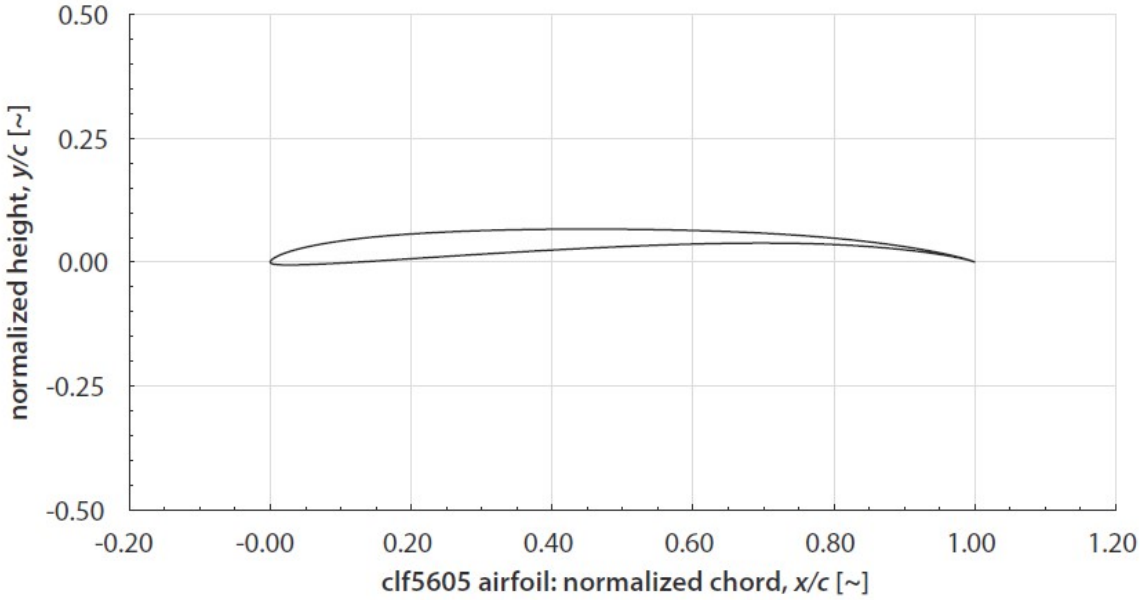

Figure 1.3: The CLF5605 airfoil cross section at 3/4-span

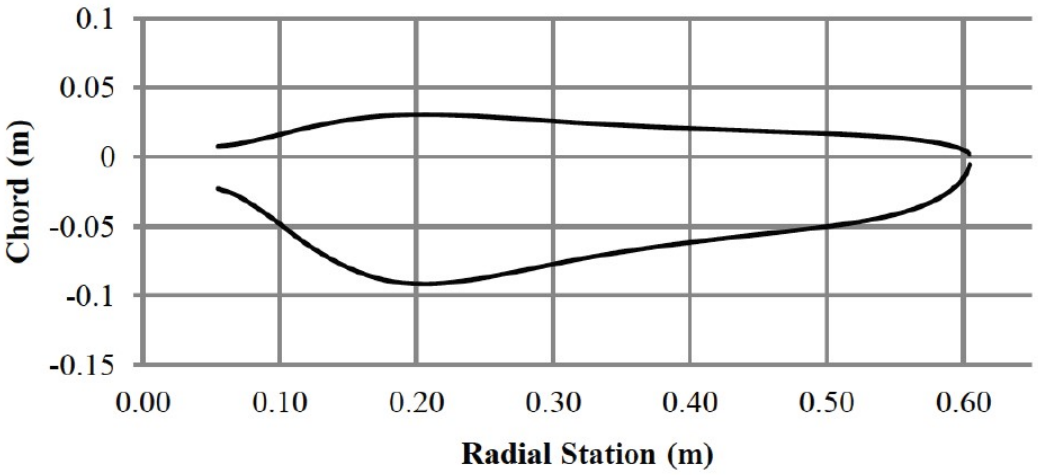

Figure 1.4: The blade planform

Section thickness was based on structural requirements: minimizing thickness reduces section profile drag which leads to corresponding performance benefits, but the unusually high first flapping frequency required for stable flight drove the design to a minimum thickness of 5% for the outboard sections and the airfoils inboard of $r/R = 0.52$ increase in thickness to the round interface tube at the root.

The high first flapping frequency is caused by the low density atmospheric condition affecting the dynamics of blade flapping: the rotating blade acts as a mass-spring-damper

system, where the predominant source of damping is aerodynamic – as the blades move up and down, the angle of attack changes in such a way as to generate forces opposing the flap motion. However, because the low atmospheric density on Mars cannot be matched by a corresponding reduction in blade inertia, the relative damping of the flap mode is approximately an order of magnitude lower for the Mars Helicopter than for a typical Earth helicopter.

The reduced damping affects the helicopter dynamics in multiple ways, one of which is to introduce poorly damped, oscillatory regressing and advancing flap modes that couple with the body of the helicopter. This is a potential issue for flight control, because a high-bandwidth attitude controller can potentially interact with and amplify the oscillatory modes, thereby destabilizing the system.

This issue is solved by making the rotor blades extremely stiff, thus driving the flap modes to high enough frequencies that interference with the control system is no longer an issue. Requirements on blade stiffness were designed with the purpose of ensuring a regressing flap mode frequency of at least 30 Hz. For the flight design, the non-rotating flap frequency can be estimated at approximately $65-70$ Hz, which ensures that the requirement is met.

In Table 1.2, the numerical values of some key parameters for Ingenuity rotor blades are listed.

Parameter	**Physical meaning**
$m_{bl} = 0.043\ kg$	Mass of each blade
$J_\beta = 0.005\ kg \cdot m^2$	Moment of inertia of each blade
$\gamma = 0.33$	Blade lock number
$e = 0.05\ m$	Effective hinge offset

Table 1.2: Blade parameters [2]

1.2. Landing gear system

The Mars helicopter landing gear system is designed to accommodate a wide range of dynamic landing conditions and surface features (see Fig. 1.5).
A large footprint with a side length of 577 mm provides a stable base for the helicopter and reduces risk of tip-over.
Rigid, lightweight, composite landing legs and feet with high resonant frequencies ensure that the landing gear modes do not interact with the control system. The four landing gear legs are attached to a molded composite interface plate, which is bonded to the main helicopter mast.
Latching deployment hinges at the top of the legs allow the landing gear system to be folded and released from the stowed state required for rover accommodation.

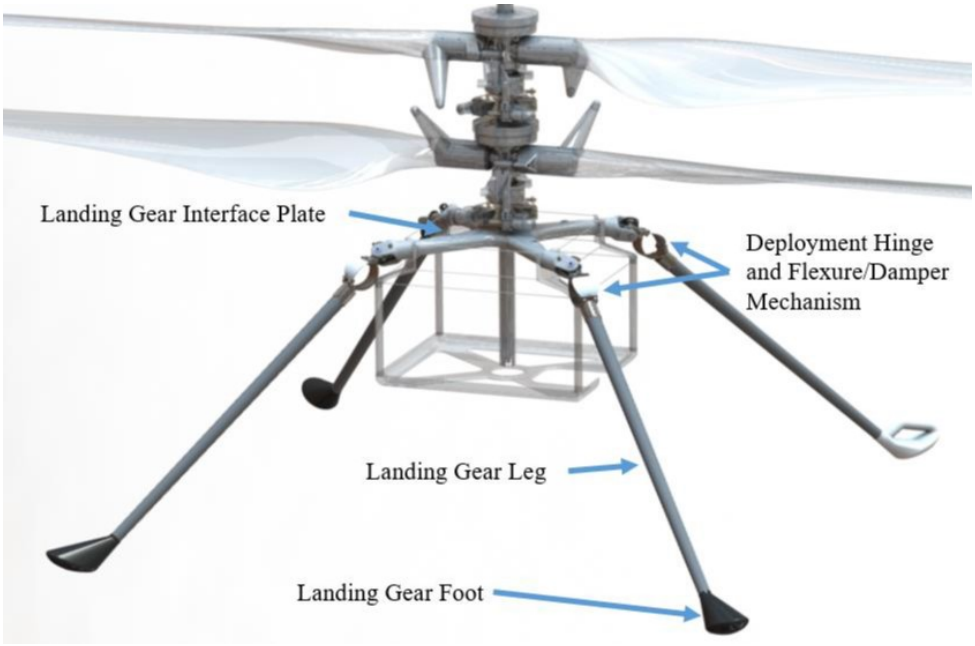

Figure 1.5: Mars Helicopter Landing gear system

Expected landing velocities up to 2 m/s are arrested by a titanium flexure at the root of each landing leg, which can deflect as much as 15° to provide an effective vertical stroke of 92 mm. An opposing flexure of 1100-series annealed aluminum deforms plastically to provide a lightweight damping solution that is largely independent of temperature or atmospheric pressure (see Fig. 1.6).

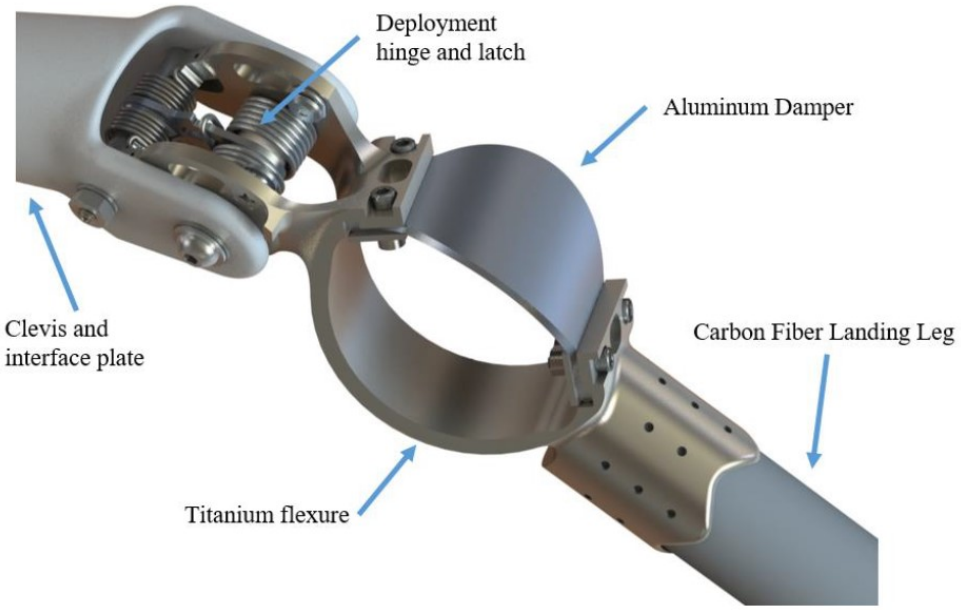

Figure 1.6: Landing gear deployment hinge and flexure/damper mechanism

1.2.1. Take-off and landing phases

Take-off and landing are the most critical phases of flight.

1. **Take-off**: during the initial takeoff, a constant thrust setting is applied, corresponding to a level approximately 20% above the vehicle weight. The purpose of this is to effect a quick separation of the legs from the ground.
   Full six-degree-of-freedom (6-DOF) control is not applied during this phase, since the legs are initially in contact with the ground; however, limited control is applied to reduce the angular rates of the vehicle.
   The initial takeoff phase lasts only a short time; once the vehicle has climbed 5 cm, or a 4 s timeout has been reached, full control is enabled. From this point on until the end of the flight, the control system tracks a reference trajectory for position, velocity, attitude, and angular rates provided by the guidance subsystem.

2. **Landing**: on landing, updates from the LRF and camera are again turned off when the vehicle is an estimated 1 m away from ground contact.
   When the vehicle is an estimated 0 : 5 m away from ground contact, touchdown detection is enabled. Touchdown detection is based on monitoring the vertical velocity control error, to determine whether the landing gear has made contact with the ground. When the control error exceeds a given threshold, indicating that the vehicle is unable to continue along its downward trajectory, all control is disabled

and the collective is set to the minimum value of $-4.5°$ on both rotors.

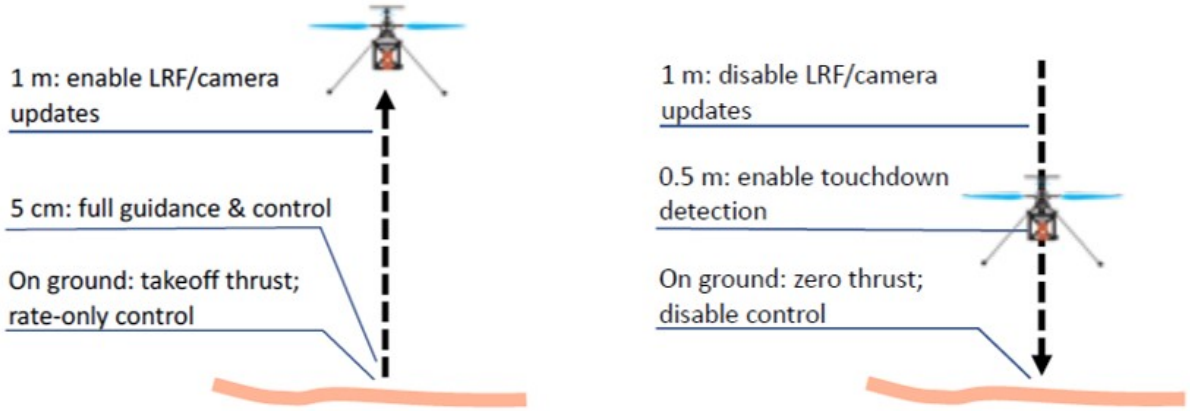

Figure 1.7: Illustration of take-off and landing sequences

1.3. Thermal system

The helicopter must survive the cold of the night on Mars where temperatures can drop to $-100°$C or lower.
The most critical component is the battery which is kept above $-15°$C through the night as it powers Kapton film heaters attached to the battery cells.
The avionics boards in the ECM surround the battery and are also kept at an elevated temperature by virtue of their proximity to the warm battery assembly.
Insulation around the avionics boards is provided by a carbon-dioxide gap of 3 cm width. Additional insulation can be provided by replacing the carbon-dioxide gas with an Aerogel formulation.
The outermost fuselage thermal coating is from Sheldahl with Solar absorptivity $\alpha = 0:8$ and infra-red (IR) emissivity $\epsilon = 0:1$.
In addition to thermal losses through the gas gap (or aerogel), additional losses occur due to conduction in the mast as well as through the copper wiring that penetrate the ECM from the mast. To minimize the latter, the wire gauges are selected to be of the thinnest gauges that can still support the current draw during operations without overheating.
Prior to flight, under the control of the FPGA, the thermal system powers on heaters in the motor control boards that have been exposed to the ambient temperatures. The internal battery temperature is brought up to $5°$C to allow hi-power energy extraction from the cells.
During operation the ECM and battery warm up as a result of avionics operations and

battery self-heating. However, the thermal inertia of the elements is such that for the short flights of the helicopter, there is no overheating.

Figure 1.8: NASA technician is shown working on Ingenuity that features a Kapton insulation blanket protecting the Helicopter Warm Electronics Box

1.4. Electronic Core Module

An illustration of the Electronics Core Module is shown in Fig. 1.9 and its components will be described in more details in the next subsections.

1.4.1. Power and energy System

The helicopter is powered by a Li-Ion battery system that is recharged daily by a solar panel.
The energy in the battery is used for operating heaters to survive the cold Martian nights as well as operate the helicopter actuators and avionics during short flights.
Depending on the latitude of operations and the Martian season, recharging of this battery through the solar panel could occur over one to multiple sols (Martian days).
The helicopter battery shown in Fig. 1.10 consists of 6 Sony SE US1865o VTC4 Li-ion cells with a nameplate capacity of 2 Ah. The maximum discharge rate is greater than 25

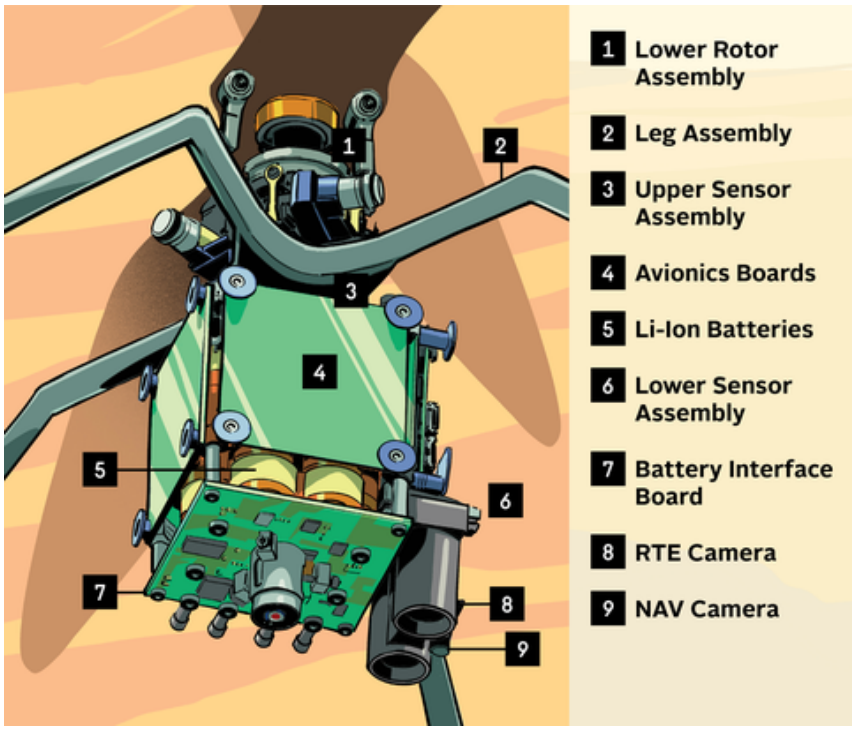

Figure 1.9: Electronics Core Module (ECM) showing configuration of battery surrounded by avionics boards and attached sensor assemblies

A and the maximum cell voltage specified by the manufacturer is 4.25 V. The continuous tested power load capability of this battery is 480 W with a peak power capability of 510 W. Battery voltage is in the range of $15 - 25.2$ V and the total mass of the 6 cells is 273 g. A cell balancing charge management system controlled by the FPGA ensures that the all the individual cells are at a uniform voltage.

A de-rated end-of-life battery capacity of 35.75 Wh is available for use. Of this capacity, 10.73 Wh (30%) is kept as reserve, night-time survival energy usage is estimated at 21 Wh for typical operation in the northern latitudes in the spring season, and approximately 10 Wh is available for flight.

Assuming that 20% of the power is at the peak load of 510 W and 80% is at a continuous load of 360 W, approximately 90 s of flight is possible.

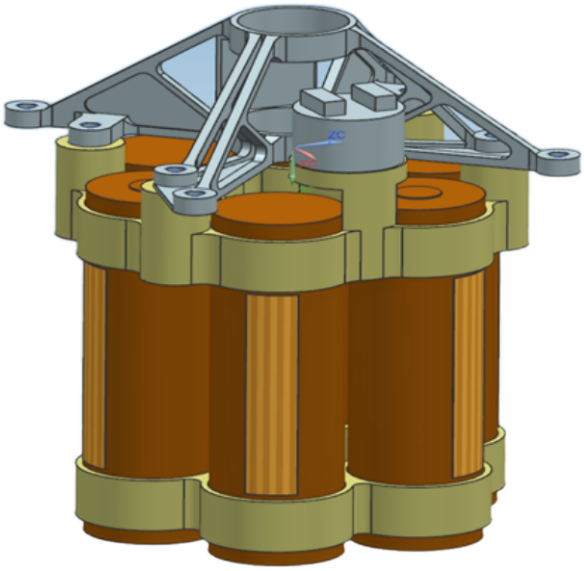

Figure 1.10: 3D-CAD of Battery assembly with Li-Ion cells and bonded thermostat and heaters

1.4.2. Avionics

The avionics design is required to have low mass, low power and adequate radiation tolerance. A set of candidate parts to meet these requirements have been incorporated into the design which is now described.

1. **Processor**: the Snapdragon processor from Intrinsyc with a Linux operating system performs high-level functions on the helicopter.
   The Snapdragon processor has a 2.26 GHz Quad-core Snapdragon 801 processor with 2 GB Random Access Memory (RAM), 32 GB Flash memory, a Universal Asynchronous Receiver Transmitter (UART), a Serial Peripheral Interface (SPI), General Purpose Input/Output (GPIO), a 4000 pixel color camera, and a Video Graphics Array (VGA) black-and-white camera. This processor implements visual navigation via a velocity estimate derived from features tracked in the VGA camera, filter propagation for use in flight control, data management, command processing, telemetry generation, and radio communication.
   The Snapdragon processor is connected to two flight-control (FC) Microcontroller Units (MCU) via a Universal Asynchronous Receiver/Transmitter (UART). These MCU processor units operate redundantly, receiving and processing identical sensor data to perform the flight-control functions necessary to keep the vehicle flying in the air. At any given time, one of the MCU is active with the other waiting to be hot-swapped in case of a fault.

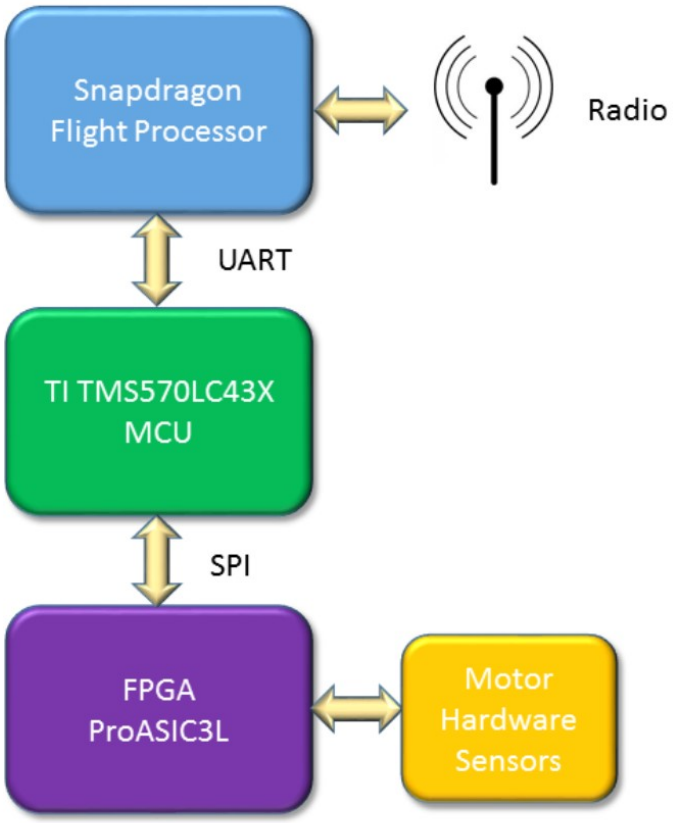

Figure 1.11: Block diagram of Avionics Elements

2. **Avionics Boards**: The avionics consists of 5 printed circuit boards which form the 5 facets of the Electronic Core Module cube. The boards are shown in Fig. 1.12.

   - *Battery Interface Board (BIB)*: placed in the bottom of the cube, it hosts the battery monitoring circuitry, motor power switches and current monitors.
   - *FPGA/Flight Controller Board (FFB)*: the two redundant TI Hercules safety processors serve as the low-level flight controller; the two processors run in sync and are provided with the same clock and data by the FPGA, which handles all the sensors and actuators interface. If a fault is detected, it signals the error to the FPGA; the FPGA switches to the other processor and power cycles the faulty one, so the flight control software continues to run without disruption.
   - *NAV/Servo Controller Board (NSB)*: the NSB carries the Snapdragon CPU and provides power and I/O interfaces. NSB also hosts the drive circuitry for the 6 DC servo motors and delivers over 20 W power.
   - *Telecom Board (TCB)*: the telecom module is mounted on the TCB. Some

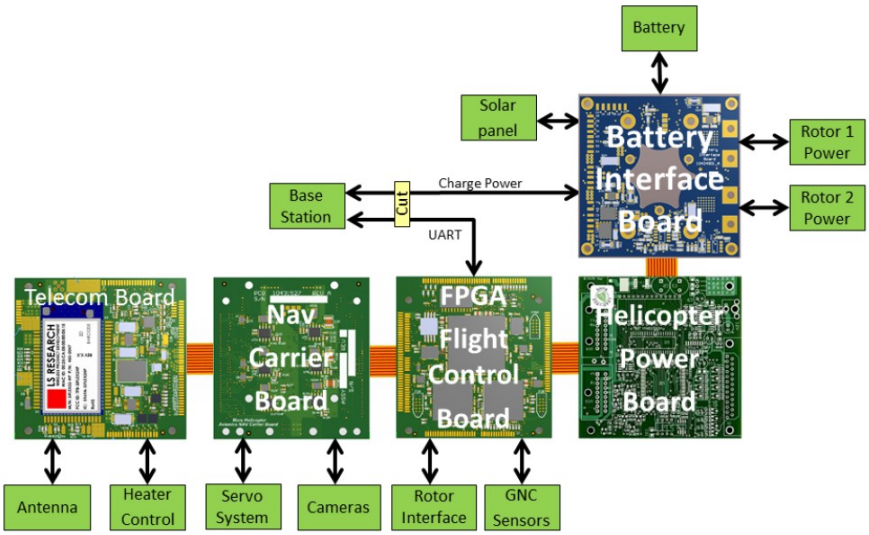

Figure 1.12: Avionics Boards shown in unfolded configuration together with key interfaces

additional analog circuitry, a 16-bit 8-channel ADC, the temperature sensor interface and heater switches take up the remaining space. This ADC is used for monitoring charging current and temperature without having to turn on the FCs, thereby saving power.

- *Helicopter Power Board (HPB)*: the HPB has two DC/DC converters that regulate the battery voltage to the 3.3 V and the 5 V. The 5 V regulator can be switched off.

1.5. Concept of operation

Flights will be conducted based on a flight plan uploaded from the ground, consisting of a series of waypoints.
Due to the many minutes of communication delay between Earth and Mars, each flight must be conducted with full autonomy. For this purpose, onboard navigation is performed using a combination of upper and lower sensors:

1. The IMU, which measures accelerations and angular rates, is used for propagation of the vehicle state from one time step to the next.
2. The camera is used together with the laser rangefinder to determine height above ground and translational velocity (this information is fused with the IMU solution).
3. The inclinometer is used to determine initial attitude before takeoff.

The onboard computation platform consists of a radiation-tolerant fieldprogrammable gate array (FPGA); a dual-redundant automotiveclass microcontroller hosting the most critical flight control functions; and a cell-phone class processor hosting the vision-based navigation functions.
The helicopter will only fly in favorable weather, with wind velocities limited to 10 m/s horizontally and 2 m/s vertically, with a maximum gust component of 3.5 m/s.
Based on the forecasted weather, ground speed and climb/descent speeds will be limited such that maximum airspeed does not exceed 10 m/s horizontally and 3.5 m/s vertically.
The batteries provide energy for flights lasting up to approximately 90 s.

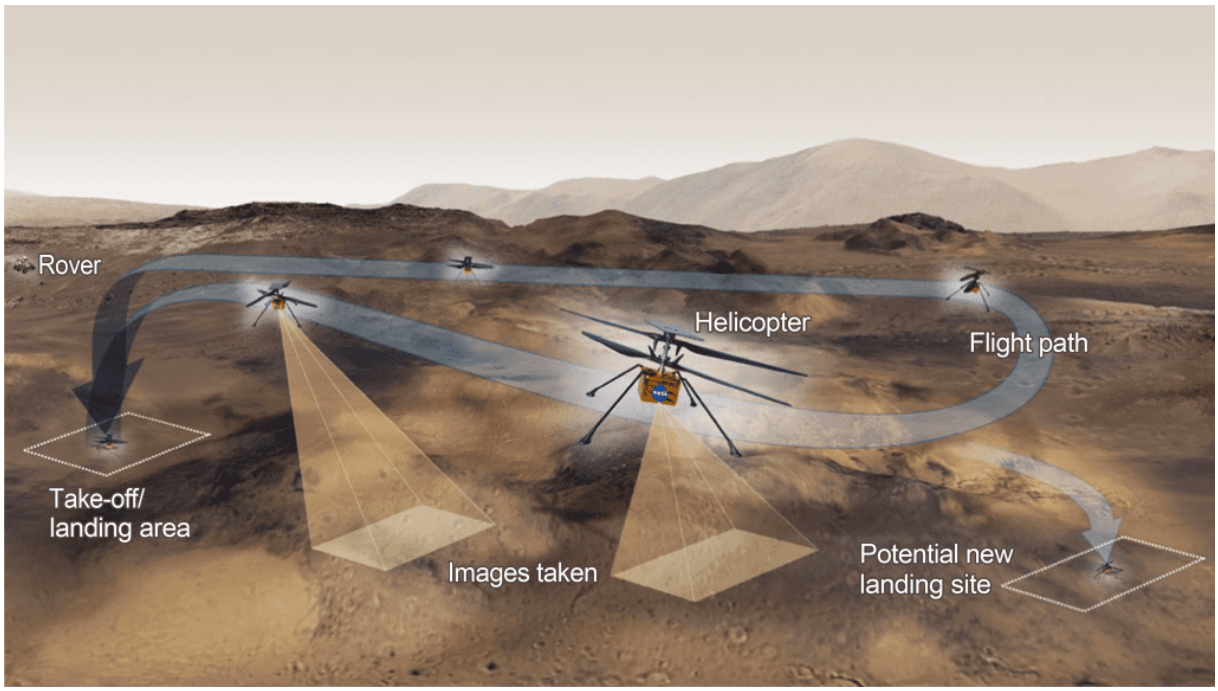

Figure 1.13: Typical Ingenuity's operation

Parameter	Range
Atmospheric density	$0.014 - 0.02\ kg/m^3$
Horizontal wind	$\leq 10\ m/s$
Vertical wind	$\leq 2\ m/s$
Gust component	$\leq 3.5\ m/s$
Landing area slope	$\leq 10°$
Endurance	$\leq 90\ s$
Flight range	$\leq 300\ m$
Flight altitude	$\leq 5\ m$

Table 1.3: Summary of key operational conditions and limitations [6]

Property	Value
Dry Mass	$1.8\ kg$
Rotor diameter	$1.21\ m$
Rotor spacing	$0.1\ m$
Ground clearance	$0.3\ m$
Landing gear footprint	$0.6 \times 0.6\ m$
Thrust-to-weight ratio	135 to 155%
Rotor speed	$\leq 2800\ rpm$
Collective control (both rotors)	$-4.5°$ to $17.5°$
Cyclic control (both rotors)	$\pm 10°$

Table 1.4: Summary of key physical parameters [6]

1.6. Demonstration vehicle

The vehicle used to demonstrate controlled flight is shown in Fig. 1.14.
It features a full-scale rotor similar to the final vehicle built for Mars flight, but with a slightly larger rotor spacing corresponding to 9% of the rotor diameter. However, because this vehicle was required to lift its own weight in Earth gravity, anything nonessential to the demonstration of controlled flight was left off the vehicle to reduce weight to a total of 765 g.
Unlike the Mars vehicle, the demonstration vehicle was equipped with cyclic control only

on the lower rotor (and collective on both rotors). This provides sufficient degrees of freedom for control but results in reduced control authority and greater cross-axis coupling.

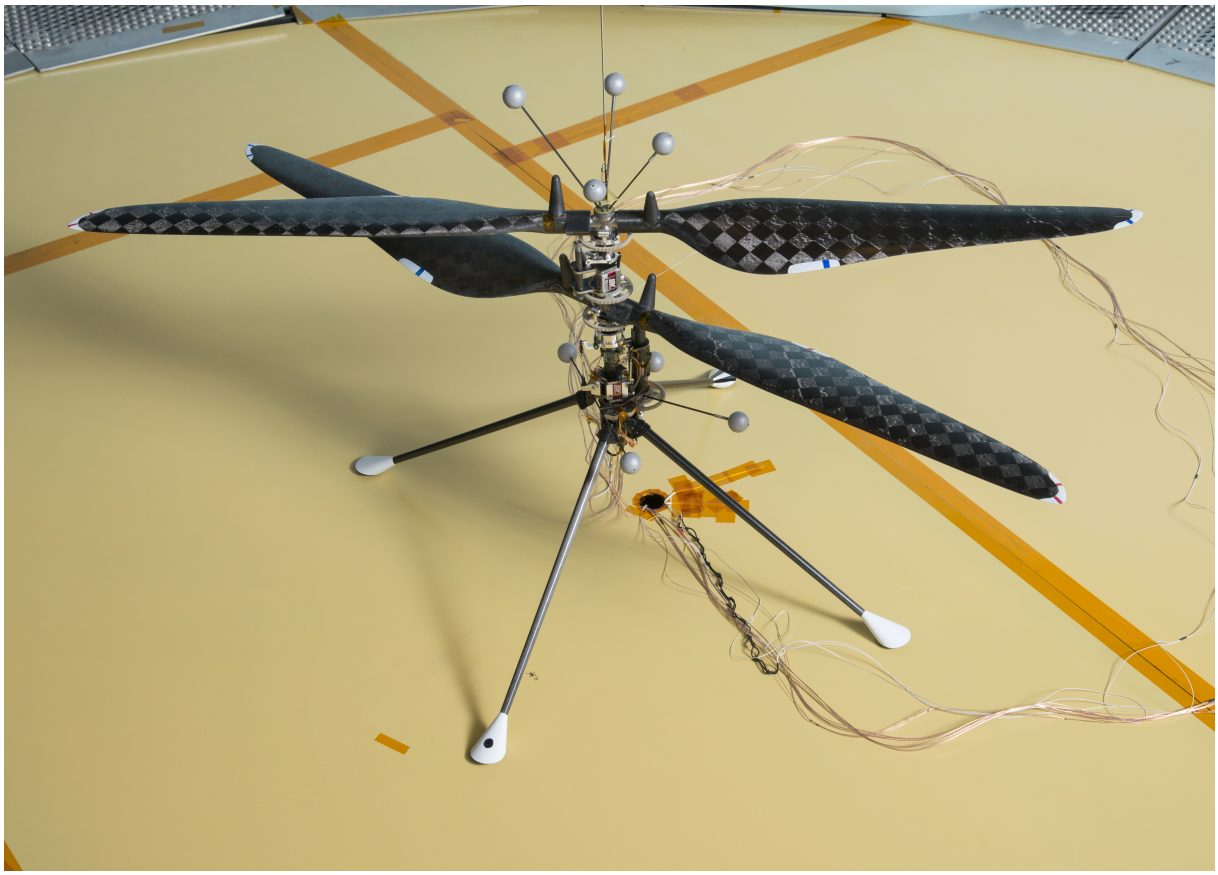

Figure 1.14: Demonstration vehicle used for controlled-flight demonstration in Martian atmospheric conditions.

Property	**Value**
m	0.765 kg
I_{xx}	0.0285 $kg\ m^2$
I_{yy}	0.0289 $kg\ m^2$
I_{zz}	0.0121 $kg\ m^2$

Table 1.5: Summary of key physical parameters of demonstration vehicle [6]

2 | Vehicle dynamics

As for all helicopter UAVs, obtaining an accurate mathematical model is a challenging task. The aim of this work is to derive a simplified mathematical model that is reliable in near hovering conditions and at the same time that allows capturing the most relevant nonlinear effects. Specifically, its dynamics have been modeled basing on the study of flight dynamics of a terrestrial miniature rotorcraft [3] and properly readjusting it for a coaxial case taking inspiration from the work of Fei Wang [4].

2.1. Working principles

Before deriving the flight dynamic model, the basic working principles of a coaxial helicopter are briefly described.
First of all, a coaxial helicopter has a pair of contrarotating rotors (upper and lower) to provide the fundamental lift force for the overall platform.
The dynamic motion of the helicopter is achieved by actively changing the pitch angles of both upper and lower rotors via the upper swashplate and the lower swashplate, respectively.
For Ingenuity, the pitch angles of both rotors are constituted by collective pitch and cyclic pitch, which are mixed controlled by three servos linked to each swashplate.
Dynamic movement of the helicopter in *Roll-Pitch* direction is realized by changing the cyclic pitch angles of both rotors; on the other hand, *Heave* and *Yaw* direction controls are obtained by changing collective pitch angles of both rotors in the same direction for the first and in opposite direction for the second.

2.2. Reference systems

2.2.1. Inertial reference system

The inertial reference system is a Cartesian coordinate system of three fixed axes that works as a fixed base for the representation of the position of a considered body or moving

reference system.
The origin of the system could be set everywhere (for example the intersection of the equator with the prime meridian and the mean sea level): it is completely arbitrary but once chosen it cannot vary.
The displacement along one or more set of orthogonal axes attached to the origin describes the position of anything in this reference system.
It is convenient to align the axes of the reference frame with the compass: one is aligned with the axis labelled North, one with the axis labelled East and the last with the normal to the surface generated by the previous two, pointing to the centre of the Earth and labelled Down. These three axes are mutually perpendicular by construction and when referring to them in the order NED form a right-handed coordinate system.

2.2.2. Body Axes

For the representation of the attitude of the UAV it is convenient to set the origin of the body frame coinciding with the centre of gravity (CG) of the coaxial helicopter.
The chosen set of axes is a right-handed system; the X axis lies in the plane of symmetry and generally points forward, the Y axis points to the right normally to the plane of symmetry and the Z axis points down.

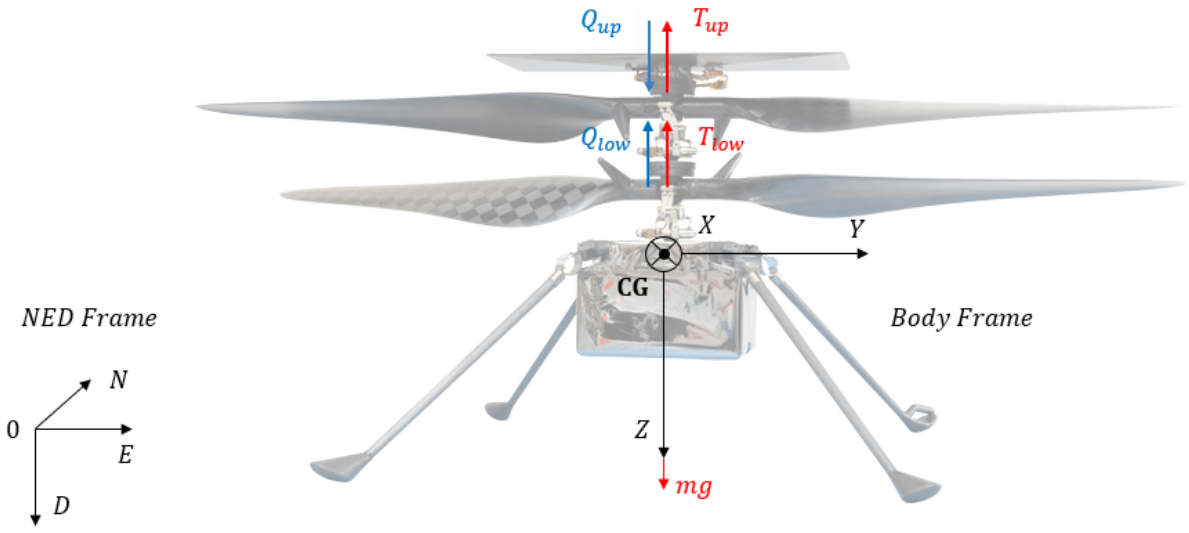

Figure 2.1: Coordinate frames and main forces and torques

2.3. Kinematics

One of the main problem in modelling and controlling a 3D system has always been the correct representation of the attitude of an object with respect to an inertial frame and a body fixed frame. This is actually a key issue in this work since the errors and so the control variables are computed based on it and the singularities of the different representations strongly influence the stability and robustness properties of the controlled system.

2.3.1. Attitude and position representation

Vectors can be rotated about any axes in any order for any number of times until the final orientation is achieved. These subsequent rotations can be represented by means of a rotation matrix from the initial orientation to the final one.
Adopting the to-from notation, a rotation matrix from system E to system D would be named R_{D-E}. Thus any vector P_E in the E reference system can be resolved to system D, in the corresponding vector PD through the matrix operation:

$$P_D = R_{D-E} P_E \tag{2.1}$$

Rotation matrices are written for $\mathbb{R}^3$ vectors and may represent the rotation around one, two or three axes.
For sake of a better comprehension it is useful to analyse the rotation around a single axis and then composing different rotations in order to achieve the final rotation matrix.
A rotation about the X axis does not change the component of the vector directed along the X axis itself, but changes the Y and Z components. All these considerations can be noticed analysing the matrix associated to this rotation of an angle Φ:

$$R_X(\Phi) = \begin{pmatrix} 1 & 0 & 0 \\ 0 & cos(\Phi) & sin(\Phi) \\ 0 & -sin(\Phi) & cos(\Phi) \end{pmatrix} \tag{2.2}$$

same considerations can be done for the rotation matrices representing respectively rotations of an angle Θ around Y and Ψ around Z axes.

These matrices have the form:

$$R_Y(\Theta) = \begin{pmatrix} cos(\Theta) & 0 & -sin(\Theta) \\ 0 & 1 & 0 \\ sin(\Theta) & 0 & cos(\Theta) \end{pmatrix} \tag{2.3}$$

$$R_z(\Psi) = \begin{pmatrix} cos(\Psi) & sin(\Psi) & 0 \\ -sin(\Psi) & cos(\Psi) & 0 \\ 0 & 0 & 1 \end{pmatrix} \tag{2.4}$$

The positive direction of the angular displacement is the one your fingers curl when aligning your thumb with the positive direction of the axis. The 0 degrees position can be assigned arbitrarily but once fixed, it must not vary.
The three presented matrices are orthonormal since each of their columns represent a vector of unit magnitude and the scalar product of column i with column j with $i \neq j$ equals zero, that is the definition of orthogonal. Orthonormality carries also the useful property that the inverse of an orthonormal matrix is its transpose, thus in order to compute the inverse rotation matrix only a transposition is needed.
It is possible to build the overall matrix representing subsequent rotations around different axes multiplying in the same sequence the rotation matrices of each rotation around each axis. Moreover, every cascade of rotations can be reduced to a rotation about three axes only. One possible way in representing these three subsequent rotations is the Euler angle conventions, whose naming convention follows NASA standard notation and consists in a first rotation of an angle Ψ around the Z axis called yaw, then a rotation of an angle Θ around the new intermediate Y axis, the so called pitch, and finally a rotation of an angle Φ around the newer X axis and also known as roll. The three angles are shown in Fig. 2.2 .

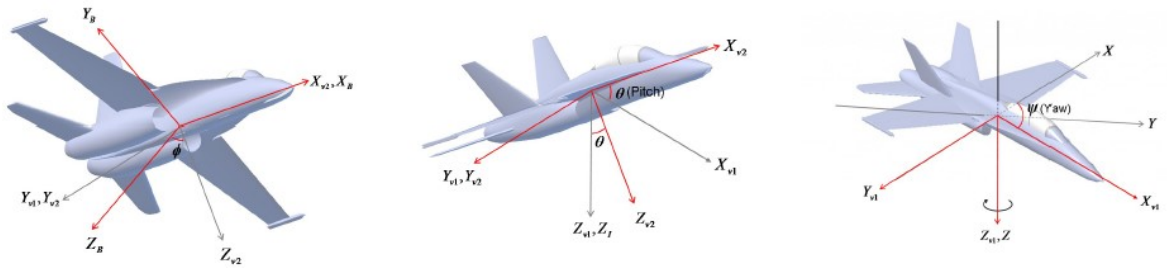

(a) Roll angle (b) Pitch angle (c) Yaw angle

Figure 2.2: Euler angles

This particular set of rotations is performed by the so called Euler rotation matrix defined

as:

$$T_{BE}(\Phi, \Theta, \Psi) = R_X(\Phi) R_Y(\Theta) R_Z(\Psi) \tag{2.5}$$

where subscript B stands for "body" and E stands for " Earth", respectively.
Matrix T_{BE} resolves an Earth-based vector to body reference system. The overall formulation of the T_{BE} matrix is then:

$$T_{BE}(\Phi, \Theta, \Psi) = \begin{pmatrix} C_\Theta C_\Psi & C_\Theta C_\Psi & -S_\Theta \\ S_\Phi S_\Theta C_\Psi - C_\Phi S_\Psi & S_\Phi S_\Theta S_\Psi + C_\Phi C_\Psi & S_\Phi C_\Theta \\ C_\Phi S_\Theta C_\Psi + S_\Phi S_\Psi & C_\Phi S_\Theta S_\Psi - S_\Phi C_\Psi & C_\Phi C_\Theta \end{pmatrix} \tag{2.6}$$

where the shorthand notation $C_\Phi = cos\Phi$, $S_\Phi = sin\Phi$, $T_\Phi = tan\Phi$ has been adopted.
To conclude the description of the configuration of the body attached frame, the position vector is given by

$$P_e = \begin{bmatrix} N \\ E \\ D \end{bmatrix} \tag{2.7}$$

where P_e is the position of the UAV centre of gravity in the inertial (Earth) frame (NED).
Starting from these considerations the vector of angular position of the UAV body axes with respect to the Earth reference system can be defined as:

$$\alpha_e = \begin{bmatrix} \Phi \\ \Theta \\ \Psi \end{bmatrix} \tag{2.8}$$

named respectively roll angle, pitch angle and yaw angle.

2.3.2. Kinematics

Of course, the three angles just defined vary with time during a maneuver and so the Euler rates are function of both the Euler angles and the body-axis angular rates.
Firstly the Euler rates are defined as:

$$\omega_e = \begin{bmatrix} \dot{\Phi} \\ \dot{\Theta} \\ \dot{\Psi} \end{bmatrix} = \dot{\alpha}_e \tag{2.9}$$

and the body-axis rates as:

$$\omega_b = \begin{bmatrix} p \\ q \\ r \end{bmatrix} \tag{2.10}$$

To get the relation from Earth-axis rates to body-axis ones each Euler rate has to be considered individually, resolved to intermediate axes and only at the end resolved to body axes. Define the Euler rate elemental vectors as:

$$\omega_{\dot{\Phi}} = \begin{bmatrix} \dot{\Phi} \\ 0 \\ 0 \end{bmatrix}, \ \omega_{\dot{\Theta}} = \begin{bmatrix} 0 \\ \dot{\Theta} \\ 0 \end{bmatrix}, \ \omega_{\dot{\Psi}} = \begin{bmatrix} 0 \\ 0 \\ \dot{\Psi} \end{bmatrix} \tag{2.11}$$

Rotate $\omega_{\dot{\Psi}}$ through the angle Θ about the Y axis, and add the result to the $\omega_{\dot{\Theta}}$ vector. Rotate that sum about the X axis through the angle Ψ and add the result to the $\omega_{\dot{\Phi}}$ vector. This last resulting vector is the body-axis angular rates vector.

$$\omega_b = \omega_{\dot{\Phi}} + R_X(\Phi)(\omega_{\dot{\Theta}} + R_Y(\Theta)\omega_{\dot{\Psi}}) \tag{2.12}$$

Rearranging the terms we get to

$$\omega_b = E(\Phi, \Theta)\omega_e = \begin{pmatrix} 1 & 0 & -S_\Theta \\ 0 & C_\Phi & S_\Phi C_\Theta \\ 0 & -S_\Phi & C_\Phi C_\Theta \end{pmatrix} \omega_e \tag{2.13}$$

On the contrary, to get the Earth-axis rate in terms of body-axis rates the inversion of the transformation matrix E is needed.
Unlike the T_{BE} matrix, matrix E is not orthonormal and in addition its inverse present two singularities in case of a pitch angle of $\pm 90°$.

$$E(\Phi, \Theta)^{-1} = \begin{pmatrix} 1 & S_\Phi T_\Theta & C_\Phi T_\Theta \\ 0 & C_\Phi & -S_\Phi \\ 0 & S_\Phi / C_\Theta & C_\Phi / C_\Theta \end{pmatrix} \tag{2.14}$$

This singularity is called gimbal lock and is one of the main difficulties when handling aggressive flight maneuvers with Euler angles parametrization. Indeed, in this work we will make use of the quaternion parametrization for simulation purposes and of the rotation matrix for control law design.

The kinematics of position is given by

$$V_e = \begin{bmatrix} \dot{N} \\ \dot{E} \\ \dot{D} \end{bmatrix} = \dot{P}_e \tag{2.15}$$

$$V_b = T_{BE}(\Phi, \Theta, \Psi)V_e = \begin{bmatrix} u \\ v \\ w \end{bmatrix} \tag{2.16}$$

where V_e is the velocity of the UAV centre of gravity in the NED frame and V_b is the same velocity resolved to body axes.

2.4. Flight dynamics

The model is developed under the assumption of the rigid body, that is all the points belonging to the body move keeping the distances and the angles fixed.

2.4.1. Velocities and accelerations

When considering the kinematic of a moving frame system following a generic path, it has to be considered that both the modulus and the direction of the velocity vector can change. A straightforward consequence of this fact is that, defining S the position vector of a point expressed in a reference system rotating with angular rate ω_b

$$S = \begin{bmatrix} x \\ y \\ z \end{bmatrix}, \ \omega_b = \begin{bmatrix} p \\ q \\ r \end{bmatrix} \tag{2.17}$$

and

$$\frac{\partial S}{\partial t} = \begin{bmatrix} \dot{x} \\ \dot{y} \\ \dot{z} \end{bmatrix} = \begin{bmatrix} u \\ v \\ w \end{bmatrix} \tag{2.18}$$

the total velocity and acceleration seen in the Earth frame are

$$\frac{dS}{dt} = \frac{\partial S}{\partial t} + \omega_b \times S \tag{2.19}$$

$$\frac{d^2S}{dt^2} = \frac{\partial}{\partial t}(\frac{dS}{dt}) + \omega_b \times \left(\frac{dS}{dt}\right) = \frac{\partial^2 S}{\partial t^2} + 2\omega_b \times \frac{\partial S}{\partial t} + \frac{\partial \omega_b}{\partial t} \times S + \omega_b \times (\omega_b \times S) \tag{2.20}$$

2.4.2. Linear motion

The description of the linear motion of a body can be obtained starting from the second Newton's Law. Linear momentum is the product of the mass times the velocity of an object. A force acting on the object makes the related momentum change:

$$F = \frac{d(mV_b)}{dt} \tag{2.21}$$

Applying to this expression (2.19) and (2.20) and adopting dot notation for the sake of readability:

$$F = \frac{dm}{dt}V_b + m\left(\frac{\partial V_b}{\partial t} + \omega_b \times V_b\right) = \dot{m}V_b + m\dot{V_b} + \omega_b \times (mV_b) \tag{2.22}$$

The obtained expression in Eq. 2.22 represents the rate of change of the linear momentum as a function of the applied forces. In the system under analysis those forces are forces coming from various mechanical parts, gravity, aerodynamics and others that can be lumped into a category called externally applied loads. In the following the vector F_{ext} represents the external forces:

$$F_{ext} = \begin{bmatrix} F_X \\ F_Y \\ F_Z \end{bmatrix} \tag{2.23}$$

Assuming a constant mass of the UAV the resulting equation of linear motion takes the form:

$$m\dot{V_b} + \omega_b \times (mV_b) = F_{ext} \tag{2.24}$$

2.4.3. Angular motion

Expanding and rearranging Eq. 2.20, the acceleration of a point can be expressed as:

$$\begin{cases} \ddot{x} = \dot{u} + \dot{q}z - \dot{r}y + q(w + py - qx) - r(v + rx - pz) \\ \ddot{y} = \dot{v} + \dot{r}x - \dot{p}z + r(u + qz - ry) - p(w + py - qx) \\ \ddot{z} = \dot{w} + \dot{p}y - \dot{q}x + p(v + rx - pz) - q(u + qz - ry) \end{cases} \tag{2.25}$$

Considering the body mass divided into infinitesimal masses, the inertial force acting on the J-th differential mass element is:

$$\begin{cases} (dF_X)_j = dm_j \ddot{x} \\ (dF_Y)_j = dm_j \ddot{y} \\ (dF_Z)_j = dm_j \ddot{z} \end{cases} \tag{2.26}$$

If the position of the differential mass element is S_j , the mass resists an angular force (a moment) about all three axes. The differential inertial moments are:

$$dM_j = S_j \times dF_j \tag{2.27}$$

$$\begin{cases} (dM_X)_j = (dF_Z)_j y_j - (dF_Y)_j z_j \\ (dM_Y)_j = (dF_X)_j z_j - (dF_Z)_j x_j \\ (dM_Z)_j = (dF_{Y\,j}) x_j - (dF_X)_j y_j \end{cases} \tag{2.28}$$

By definition, the origin of the coordinate system is the centre of gravity; therefore

$$\begin{cases} \sum(x) dm = 0 \\ \sum(y) dm = 0 \\ \sum(z) dm = 0 \end{cases} \tag{2.29}$$

Combining Eqs. 2.26, 2.28 and 2.29 the linear motion equation are obtained:

$$\begin{cases} m\ddot{x} = m(\dot{u} + qw - rv) \\ m\ddot{y} = m(\dot{v} + ru - pw) \\ m\ddot{z} = m(\dot{w} + pv - qu) \end{cases} \tag{2.30}$$

Introducing the definition of inertia tensor in the form:

$$I_n = \begin{pmatrix} I_{xx} & -I_{xy} & -I_{xx} \\ I_{yx} & I_{yy} & -I_{yz} \\ -I_{zx} & -I_{zy} & I_{zz} \end{pmatrix} \tag{2.31}$$

where the various terms can be defined as

$$\int (xy)dm = I_{xy}, \int (xz)dm = I_{xz}, \int (yz)dm = I_{yz},$$
$$\int (y^2 + z^2)dm = I_{xx}, \ (x^2 + z^2)dm = I_{yy}, \int (x^2 + y^2)dm = I_{zz}$$

Considering a body frame coincident with the symmetry axes of the aircraft body, I_n becomes a diagonal matrix.
From all the previous considerations the expression of the angular motion can be derived in the form:

$$\begin{aligned} L &= I_{xx}\dot{p} + (I_{zz} - I_{yy})qr \\ M &= I_{yy}\dot{q} + (I_{xx} - I_{zz})pr \\ N &= I_{zz}\dot{r} + (I_{yy} - I_{xx})pq \end{aligned} \tag{2.32}$$

where L, M, N are the moments applied on the body-axes X, Y, Z respectively. Collecting all the applied moments in a vector M_{ext}

$$M_{ext} = \begin{bmatrix} L \\ M \\ N \end{bmatrix} \tag{2.33}$$

and recalling the definition of body-axis angular velocity vector the equation of angular motion can be reorganized in the form

$$I_n\dot{\omega}_b + \omega_b \times (I_n\omega_b) = M_{ext} \tag{2.34}$$

The similarity of this formulation with Eq. 2.24 are evident and the two together constitute the generalized equations of motion of a body.

2.5. Rotor dynamics

Since detailed rotor equations of motion can be extremely complex and not all effects related to rotors are relevant for the type of analysis we carry out in this work, we need simplified expressions for the rotor equations of motion. With these simplified dynamics, we will then be able to express the rotor forces and moments as a function of the rotor states and couple the two dynamic systems.
A fundamental aspect of rotor dynamics is the flapping motion of the blades and in the following, we will summarize the development of a so-called tip-path-plane rotor model used in low-complexity simulation systems and which represents the foundation of the

highly simplified model used for the identification.
The flapping motion is a 2π-periodic function. Thus the general solution to the flapping equation can be expressed as a the Fourier series [3]

$$\beta(\Psi) = \beta_0 - \beta_{1c}C_\Psi - \beta_{1s}S_\Psi - \beta_{2c}C_{2\Psi} - \beta_{2s}S_{2\Psi} - ... \tag{2.35}$$

In full-scale helicopters, the magnitude of the second harmonic are less than 10% of the magnitude of the first harmonic [3]. Hence, the second and higher harmonics in the Fourier series can be ignored, i.e.

$$\beta(\Psi) \approx \beta_0 - \beta_{1c}C_\Psi - \beta_{1s}S_\Psi \tag{2.36}$$

This first-harmonic representation of the blade flapping motion defines the rotor tip-path-plane (TPP) equation. This type of motion results in a cone-shaped rotor like the one illustrated Fig. 2.3. The top of the cone is the TPP. The non-periodic term β_0 describes the coning angle and the coefficients of the first harmonic β_{1c} and β_{1s} describe the tilting of the rotor tip-path-plane in the longitudinal and lateral directions, respectively. In the following, we will use the notation: a instead of β_{1c}, b instead of β_{1s}, and a_o instead of β_0.

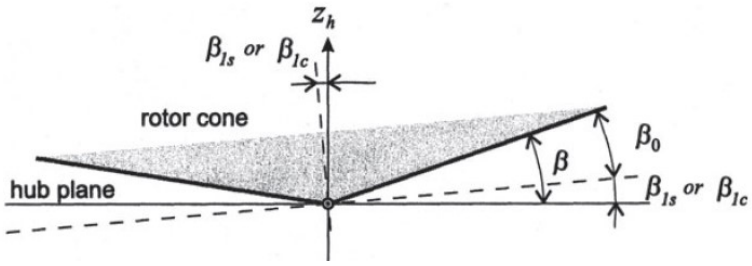

Figure 2.3: Tip-path-plane rotor representation

As a simplifying assumption for a TPP model, the blade is represented as a rigid beam and its attachement to the shaft is modeled through a flapping hinge located at the center of the hub (no hinge offset) with a linear torsional spring with spring constant K_β.
Thus, the equations for the blade flapping motion are derived from the balance of moments about the flapping hinge (Fig. 2.4).
Once derived the elemental forces acting on a blade element located at the radial station y, the flapping equation of motion results in [3]:

$$\beta'' + \left(1 + \frac{K_\beta}{I_\beta \Omega^2}\right)\beta = \frac{1}{I_\beta \Omega^2}\int_0^R y dF_z dy \tag{2.37}$$

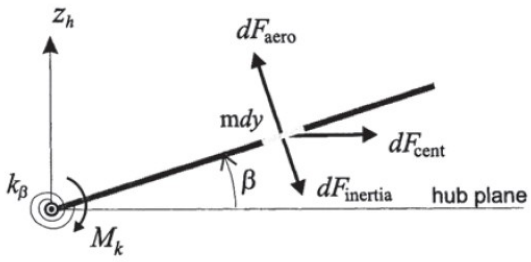

Figure 2.4: Blade represented as a rigid beam, with flapping angle β. Also shown are forces acting on a blade element, as well as the moment from the flapping spring acting at root of the blade.

where I_β is the inertia of the blade, Ω is the rotational speed of rotor and β'' describes the differentiation respect to Ψ.
Substituting the tip-path-plane expression Eq. 2.36 into the flapping differential equation Eq. 2.37, matching all the non-periodic terms with a_o, the sine terms with b, and the cosine terms with a and defining the tip-path-plane state vector $a = [a, b]^T$, we obtain a second-order matrix differential equation:

$$\ddot{a} + D\dot{a} + Ka = F \tag{2.38}$$

where D is the damping matrix, K is the stiffness matrix, and F is the forcing term.
Discarding the effects of translational speed, setting zero pitch-flap coupling coefficient and discarding the coning dynamics, the previous matrices reduce to [3]

$$D = \Omega \begin{pmatrix} \frac{\gamma}{8} & 2 \\ -2 & \frac{\gamma}{8} \end{pmatrix}; \quad K = \Omega^2 \begin{pmatrix} \frac{K_\beta}{I_\beta \Omega^2} & \frac{\gamma}{8} \\ -\frac{\gamma}{8} & \frac{K_\beta}{I_\beta \Omega^2} \end{pmatrix} \tag{2.39}$$

and

$$F = \Omega^2 \begin{pmatrix} \frac{\gamma}{8} & 0 \\ 0 & \frac{\gamma}{8} \end{pmatrix} \begin{bmatrix} A_1 \\ B_1 \end{bmatrix} + \Omega \begin{pmatrix} -2 & -\frac{\gamma}{8} \\ -\frac{\gamma}{8} & 2 \end{pmatrix} \begin{bmatrix} p \\ q \end{bmatrix} + \Omega \begin{pmatrix} 0 & -\frac{1}{\Omega} \\ -\frac{1}{\Omega} & 0 \end{pmatrix} \begin{bmatrix} \dot{p} \\ \dot{q} \end{bmatrix} \tag{2.40}$$

where γ is the blade lock number which represents the ratio between the aerodynamic and inertial forces acting on the blade

$$\gamma = \frac{\rho c C_{l\alpha} R^4}{I_\beta} \tag{2.41}$$

where R is the rotor radius, ρ is the air density, c is the blade chord length and $C_{l\alpha}$ is the lift curve slope.
A_1 and B_1 are, respectively, the lateral and longitudinal cyclic blade pitch angle defined

as functions of the longitudinal and lateral cyclic controls, δ_{lon} and δ_{lat}, respectively

$$A_1 = B_{lat}\delta_{lat} \quad B_1 = A_{lon}\delta_{lon}. \tag{2.42}$$

Next, the order of the rotor equations will reduce to discard the high-frequency dynamics. This is achieved by dropping the higher-order terms in the TPP equations of motion Eq. 2.38, i.e. the blade flapping accelerations $\ddot{a}$ and $\ddot{b}$ and the vehicle angular accelerations $\dot{p}$ and $\dot{q}$.
Using equation Eq. 2.38 with the above matrices and simplifications produces the following coupled first-order tip-path-plane equations of motion:

$$\begin{cases} \tau_f \dot{b} = -b - \tau_f p - B_a a + B_s B_1 + B_c A_1 & \text{(2.43a)} \\ \tau_f \dot{a} = -a - \tau_f q + A_b b - A_s B_1 + A_c A_1 & \text{(2.43b)} \end{cases}$$

The key terms are:

$$A_b = B_a = \frac{128K_\beta - I_\beta \gamma^2 \Omega^2}{8\gamma(2I_\beta \Omega^2 + K_\beta)} \tag{2.44}$$

which represent the coupling effect between longitudinal and lateral flapping motions.

$$\tau_f = \frac{I_\beta \Omega(\gamma^2 + 256)}{8\gamma(2I_\beta \Omega^2 + K_\beta)} \tag{2.45}$$

is the rotor time constant.
Eq. 2.43 represents the low-frequency rotor dynamic approximations which capture the key tip-path-plane responses due to control inputs and vehicle motion.

2.6. External forces and moments

Once the dynamics equations of the model have been identified, the most important contributions to forces and moments acting on the helicopter are now presented in this section.
The overall contributions can be summarized as

$$F_{ext} = F_T + F_g + F_a \tag{2.46a}$$
$$M_{ext} = M_Q + M_\beta + M_a \tag{2.46b}$$

where $F_T \in \mathbb{R}^3$ and $M_Q \in \mathbb{R}^3$ are the rotors thrust and torque, respectively; $F_g \in \mathbb{R}^3$ is the gravitational force vector in body frame; $M_\beta \in \mathbb{R}^3$ is the hub torsional moment vector and $F_a \in \mathbb{R}^3$, $M_a \in \mathbb{R}^3$ are the aerodynamic forces and moments vectors.

Each contribution in Eq. 2.46 will be investigated in more details in the following subsections.

2.6.1. Rotors thrust and torque

When spinning, each rotor produces a force and a torque that can be used to control the motion of the helicopter. In the following, we will describe a simplified model for the generation of force and torque by coaxial propellers based on BEMT (blade element momentum theory).
A first simplifying assumption is that the thrust vector is always perpendicular to the tip-path-plane (TPP), which is true in hover and vertical flight and still very accurate in forward flight [9].
In its default orientation, TPP is coincident with hub plane and rotors generate only a vertical thrust that can be expressed in body coordinates as:

$$F_T = \sum \begin{bmatrix} 0 \\ 0 \\ T_i \end{bmatrix}, \quad \text{i} \in (\text{up, low}) \tag{2.47}$$

where T_i is the magnitude of each rotor thrust.
Since during flight, the upper and lower TPPs deviate from their default orientation, the rotors generate not only a vertical thrust but also two lateral forces dependent on a longitudinal flapping angle a and a lateral flapping angle b of the blades (Fig. 2.5).
The single thrust can be rewritten as:

$$F_{T_i} = R(a_i, b_i) \begin{bmatrix} 0 \\ 0 \\ T \end{bmatrix} \tag{2.48}$$

where

$$R(a_i, b_i) = \begin{pmatrix} C_{a_i} & -S_{a_i}S_{b_i} & -S_{a_i}C_{b_i} \\ 0 & -C_{b_i} & S_{b_i} \\ -S_{a_i} & -C_{a_i}S_{b_i} & -C_{b_i}C_{a_i} \end{pmatrix} \tag{2.49}$$

is a transformation matrix between the body and rotor coordinate system.
By computing Eq. 2.48, it results:

$$F_{T_i} = T \begin{bmatrix} -S_{a_i}C_{b_i} \\ S_{b_i} \\ -C_{a_i}C_{b_i} \end{bmatrix} \tag{2.50}$$

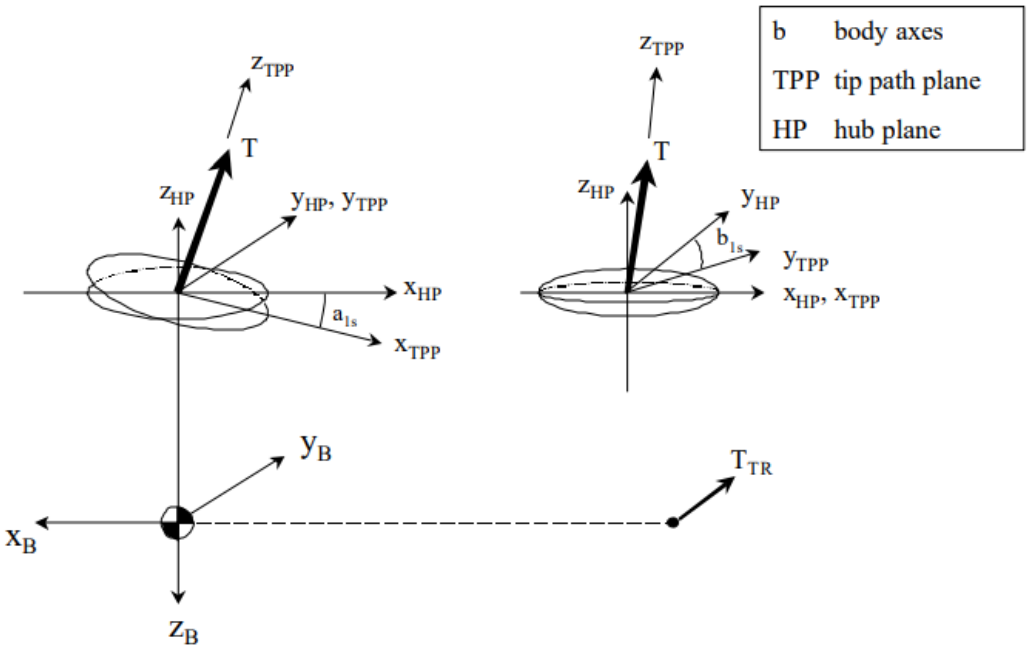

Figure 2.5: Hub plane, tip-path plane and body axes

and the overall thrust vector:

$$F_T = T_{up} \begin{bmatrix} -S_{a_{up}} C_{b_{up}} \\ S_{b_{up}} \\ -C_{a_{up}} C_{b_{up}} \end{bmatrix} + T_{low} \begin{bmatrix} -S_{a_{low}} C_{b_{low}} \\ S_{b_{low}} \\ -C_{a_{low}} C_{b_{low}} \end{bmatrix} \tag{2.51}$$

According to the aerodynamic actuator disk theory [1], the magnitude of rotor thrust can be formulated as:

$$T = \rho C_T A \Omega^2 R^2 \tag{2.52}$$

where ρ is the air density, A is the rotor disk area, Ω is the rotor rotational speed, R is the rotor radius and C_T is the rotor thrust coefficient. All these parameters are constant except for the last one.

In order to evaluate the total thrust coefficient, it is necessary first to find the expression of its incremental.

The incremental thrust dC_T can be obtained using the BEMT theory with small angle assumptions ($\cos\phi \approx 1$, ϕ is the inflow angle equal to λ/r) [11]:

$$dC_T = 4F\lambda(\lambda - \lambda_\infty) r dr \tag{2.53}$$

where r is the nondimensional radial distance along the blade, F is the factor to account for the Prandtl tip losses, λ is the nondimensional inflow velocity and λ_∞ is the nondi-

mensional axial velocity (equal to zero in hovering conditions).
Now, using the conventional blade-element theory (BET), the incremental thrust can be rewritten as [11]:

$$dC_T = \frac{1}{2}\sigma C_{l_\alpha}(\theta_i r^2 - \lambda r)dr \tag{2.54}$$

where C_{l_α} is the bidimensional lift-curve slope of the airfoil section and although it will get a different value at each blade station because it is a function of local incident Mach number and Reynolds number, an average value for the rotor can be assumed without serious loss of accuracy [11].
The rotor solidity σ is defined as the ratio of the blade area against the rotor disk area:

$$\sigma = \frac{N_b c}{\pi R} \tag{2.55}$$

where N_b are the number of blades per rotor and c is the chord of the blade.
θ_i is the blade pitch distribution on the i-th rotor and it is related to the collective commanded controls (δ_{i0}).
The most critical part of the design is the evaluation of λ, the nondimensional inflow velocity.
The generic expression of λ is function of r and it can be obtained equating the incremental thrust coefficients from the momentum and blade-element theories (i.e., using Eqs. 2.53 and 2.54) [11]:

$$\lambda(r) = \sqrt{\left(\frac{\sigma C_{l_\alpha}}{16F} - \frac{\lambda_\infty}{2}\right)^2 + \frac{\sigma C_{l_\alpha}}{8F}\theta_i r} - \left(\frac{\sigma C_{l_\alpha}}{16F} - \frac{\lambda_\infty}{2}\right) \tag{2.56}$$

Eq. 2.56 can be solved numerically at a series of discretized elements that are distributed radially over the rotor disk; for simplification, F can be considered equal to 1 (corresponding to $N_b \to \infty$).
The expression of λ in Eq. 2.56 is valid for both the upper and lower rotors. However, as the inner part of the lower rotor operates in the *vena contracta* of the upper rotor (see Fig. 2.6), the evaluation of λ_{low} is more complicated.
For beam sections of the lower rotor lying inside the upper contraction area, the inflow distribution is given as:

$$\lambda(r) = \sqrt{\left(\frac{\sigma C_{l_\alpha}}{16F} - \frac{\lambda_\infty + (A/A_c)\lambda_u}{2}\right)^2 + \frac{\sigma C_{l_\alpha}}{8F}\theta_l r} - \left(\frac{\sigma C_{l_\alpha}}{16F} - \frac{\lambda_\infty + (A/A_c)\lambda_u}{2}\right) \tag{2.57}$$

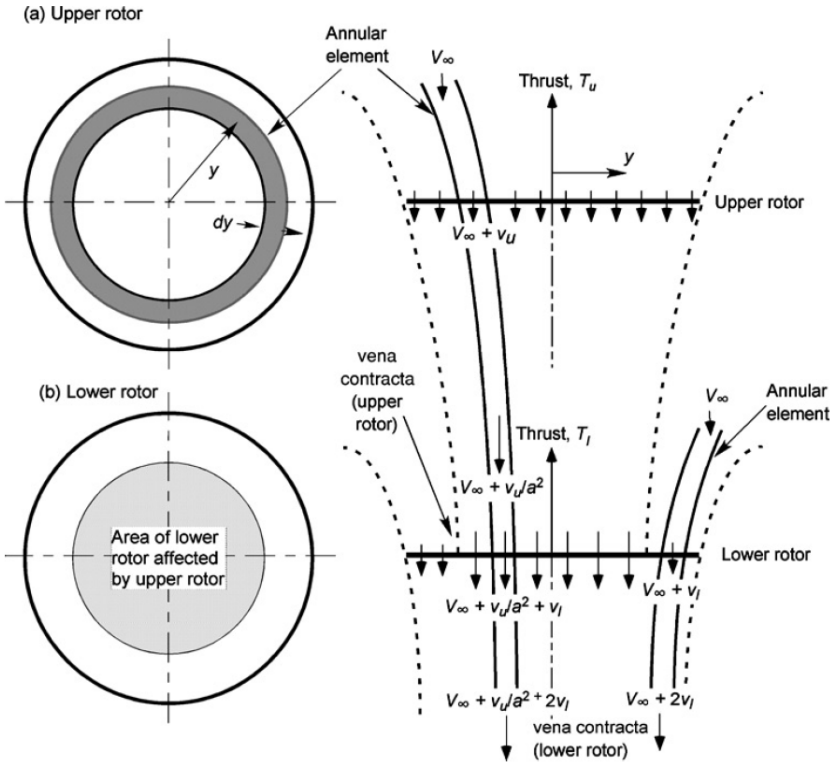

Figure 2.6: Flow model used for the BEMT analysis of a coaxial rotor system with the lower rotor operating in the slipstream of the upper rotor.

where θ_l is the blade pitch distribution on the lower rotor (related to the lower collective commanded control, δ_{l0}) and λ_u is the inflow velocity of upper rotor.
A_c is the contracted area defined as:

$$A_c = \pi r_c^2 R^2 \tag{2.58}$$

where r_c is the contraction ratio found closer to 0.8 for practical cases.
For points outside the upper contraction area, the inflow distribution is expressed as Eq. 2.56, with $i = l$.
When the spanwise inflow distributions are obtained, the rotor thrust and power coefficients for each rotor may then be found by numerical integration across each respective rotor disk.
The thrust coefficient becomes:

$$C_T = \int_{r=0}^{r=1} dC_T = \frac{1}{2}\sigma C_{l_\alpha} \int_{r=0}^{r=1} (\theta_i r^2 - \lambda r) dr \tag{2.59}$$

An alternative simplified formulation that neglects the radial distribution of the inflow but that can be employed also in forward flight conditions is derived next.
These formulas have been obtained considering the previous reasoning about inflow and interaction between the rotors but taking a θ_i and λ_i uniformly distributed along the blade (so not depending on r).
For upper rotor:

$$\begin{cases} \lambda_{up} = \dfrac{C_{T_{up}}}{2\sqrt{\mu^2 + (\lambda_{up} - \mu_z)^2}} & \text{(2.60a)} \\ C_{T_{up}} = \dfrac{C_{l_{\alpha,up}}\sigma}{2}\left(\theta_{up}\left(\dfrac{1}{3} + \dfrac{\mu^2}{2}\right) + \dfrac{\mu_z - \lambda_{up}}{2}\right) & \text{(2.60b)} \end{cases}$$

For lower rotor:

$$\begin{cases} \lambda_{low} = \dfrac{C_{T_{low}}}{2\sqrt{\mu^2 + (\lambda_{low} - k\lambda_{up} - \mu_z)^2}} & \text{(2.61a)} \\ C_{T_{low}} = \dfrac{C_{l_{\alpha,low}}\sigma}{2}\left(\theta_{low}\left(\dfrac{1}{3} + \dfrac{\mu^2}{2}\right) + \dfrac{\mu_z + k\lambda_{up} - \lambda_{low}}{2}\right) & \text{(2.61b)} \end{cases}$$

where

$$\begin{aligned} \mu &= \frac{\sqrt{(u - u_{wind})^2 + (v - v_{wind})^2}}{\Omega R} \\ \mu_z &= \frac{w - w_{wind}}{\Omega R} \end{aligned} \tag{2.62}$$

u_{wind}, v_{wind}, w_{wind} stand for velocity of wind along body-axis X, Y, Z.
The key term k in Eq. 2.61 is a coefficient taking in account the interaction between the rotors and it has been evaluated from hovering conditions as shown in the later Section 2.8.1.
Eqs. 2.60 and 2.61 are evaluated at each instant time using the MATLAB function *fsolve* and taking as initial conditions the values of λ and C_T at previous instant time.

The rotation of each rotor generates also a drag torque Q along the body-axis Z.
Similarly to thrust, this torque can be formulated according to the aerodynamic actuator disk theory [1] as:

$$Q = \rho C_Q A \Omega^2 R^3 \tag{2.63}$$

The main difference from Eq. 2.52 is represented by the coefficient C_Q.
It is necessary also in this case to find first the expression of its incremental.

The incremental rotor torque coefficient is provided by BEMT:

$$dC_Q = \frac{\sigma}{2}(\phi C_l + C_d)r^3 dr \tag{2.64}$$

where C_d is the sectional profile drag coefficient. By knowing that $\lambda = \phi r$ and $dC_T = (\sigma/2)C_l r^2 dr$, the incremental torque coefficient can be rewritten as:

$$dC_Q = \frac{\sigma}{2}C_l \lambda r^2 dr + \frac{\sigma}{2}C_d r^3 dr = \lambda dC_T + \frac{\sigma}{2}C_d r^3 dr \tag{2.65}$$

Integrating Eq. 2.65:

$$C_Q = \int_{r=0}^{r=1} dC_Q = \int_{r=0}^{r=1} \lambda \, dC_T + \frac{\sigma}{2}\int_{r=0}^{r=1} C_d r^3 dr \tag{2.66}$$

Also in this case, for simplicity, the torque coefficient is evaluated considering θ and λ uniformly distributed along the blade resulting in a final expression:

$$C_Q = \lambda C_T + \frac{\sigma}{8}C_d \tag{2.67}$$

In the first instance, the drag coefficient C_d can be assumed equal to a constant value $C_{d,0}$, whose numerical value is extracted from Fig. 2.7 basing on the fact that MH airfoil operates in a subcritical flow state and has a constant $t/c = 0.05$ [10].

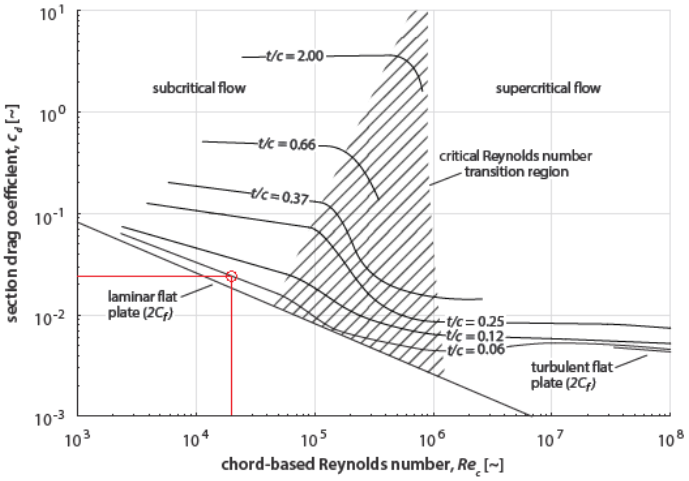

Figure 2.7: Reynolds number criticality based on thickness

Eventually, the overall rotor torque vector along the body-axis Z will be described by:

$$M_Q = \begin{bmatrix} 0 \\ 0 \\ Q_{up} - Q_{low} \end{bmatrix} \tag{2.68}$$

Moreover, when the thrust vector no longer pass through the CG of the helicopter due to the deviation of the upper and lower TPPs from their default orientation, a rotational torque is generated.
This torque can be expressed as a vectorial product given by:

$$\sum l_i \times T_i = \sum |l_i| \begin{bmatrix} 0 \\ 0 \\ -1 \end{bmatrix} \times T_i \begin{bmatrix} -S_{a_i} C_{b_i} \\ S_{b_i} \\ -C_{a_i} C_{b_i} \end{bmatrix}, \quad \text{i} \in (\text{up, low}) \tag{2.69}$$

where l_i is the displacement from the helicopter CG to the i-th rotor hub.

2.6.2. Gravitational force

Another force to be considered acting on the centre of gravity is the gravitational force. This force acts always pointing to the centre of the Earth, that is Down in the inertial frame, and so it must be rotated into body frame to get a consistent representation of its effect on the system:

$$F_g = T_{BE}(\Phi, \Theta, \Psi) \begin{bmatrix} 0 \\ 0 \\ mg \end{bmatrix} = \begin{bmatrix} -S_\Theta \\ S_\Psi C_\Theta \\ C_\Psi C_\Theta \end{bmatrix} mg \tag{2.70}$$

2.6.3. Aerodynamics forces and moments

In order to determine the aerodynamic forces acting on the body, it is necessary to know both the direction and velocity of the total airflow inside which the UAV operates.
In all, three main wind sources composing the total wind vector $V_{tot} \in \mathbb{R}^3$ can be identified: the first component is $V_b \in \mathbb{R}^3$ due to the airflow generated by the translational and rotational body displacements; the second component corresponds to the airflow speed $V_{prop} \in \mathbb{R}^3$ generated by the coaxial rotors; the third component $V_{wind} \in \mathbb{R}^3$ is due to the externally induced wind, in general unpredictable.
Since the resultant of aerodynamic forces are applied in correspondence of the CoP and, in a realistic case CoP $\neq$ CoG, a fourth component $\omega_b \times d_{cp}$ must be considered inside

the expression of the total wind vector: this represents the cross product between body angular rates $\omega_b \in \mathbb{R}^3$ and $d_{cp} = [X_{cp}, Y_{cp}, Z_{cp}]^T$, the coordinates of CoP in the body frame.
The wind vector in the body coordinate system is then written as [9] [13]:

$$V_{tot} = V_b - V_{prop} - V_{wind} + \omega_b \times d_{cp} \tag{2.71}$$

V_{prop} can be expressed as the induced velocity of the lower rotor on the fuselage and it can be written as:

$$V_{prop} = \sqrt{\frac{|T_{low}|}{2\rho\pi R^2}} \tag{2.72}$$

Considering Eq. 2.71 and a V_{prop} acting only in body-azis Z direction, the expressions of the three components of the total wind are written as follows:

$$V_{ux} = u - |V_{wind}|_{X_b} + (qZ_{cp} - rY_{cp}) \tag{2.73a}$$
$$V_{vy} = v - |V_{wind}|_{Y_b} - (pZ_{cp} - rX_{cp}) \tag{2.73b}$$
$$V_{wz} = w - V_{prop} - |V_{wind}|_{Z_b} + (pY_{cp} - qX_{cp}) \tag{2.73c}$$

where u, v, w are the three translational body-velocity components and $|V_{wind}|_{X_b}, |V_{wind}|_{Y_b}, |V_{wind}|_{Z_b}$ are the three components of the externally induced wind vector V_{wind}.
Once the expression of V_{tot} is known, the aerodynamic forces in the three body directions can be evaluated knowing the air density ρ and the effective drag areas S_x, S_y, S_z.
They can be formulated in a quadratic form as:

$$|F_{aero}|_X = -\frac{\rho}{2} S_x V_{ux} \|V_{tot}\| \tag{2.74a}$$
$$|F_{aero}|_Y = -\frac{\rho}{2} S_y V_{vy} \|V_{tot}\| \tag{2.74b}$$
$$|F_{aero}|_Z = -\frac{\rho}{2} S_z V_{wz} \|V_{tot}\| \tag{2.74c}$$
$$\tag{2.74d}$$

where

$$\|V_{tot}\| = \sqrt{V_{ux}^2 + V_{vy}^2 + V_{wz}^2} \tag{2.75}$$

The effective drag areas along the body-axis X, Y, Z are evaluated as:

$$S_i = A_i \cdot C_i, \quad \text{i} \in (\text{X, Y, Z}) \tag{2.76}$$

where C_i are the body shape aerodynamic coefficients and A_i are the surface areas of the fuselage.
The non-dimensional coefficients C_i depends on the flight conditions and on a number of quantities in a nonlinear manner, typically the Mach number, altitude, attitude and body rates. However, considering a near-hover or slow cruise flight, a fair assumption is to consider it as constant. Given the low density, this simplification has little impact on the flight dynamics.
Once defined the drag caused by linear translations, the aerodynamic moments around each axis can be defined:

$$M_{aero} = -\frac{\rho}{2}\begin{bmatrix} A_x C_{lp} V_{ux} p \\ A_y C_{mq} V_{vy} q \\ A_z C_{nr} V_{wz} w \end{bmatrix} + d_{cp} \times F_{aero} \tag{2.77}$$

where the constants C_{lp}, C_{mq} and C_{nr} are the aerodynamic damping moment coefficients.

2.7. Nonlinear model

The conventions and the Mars helicopter model have been presented in detail in this chapter, highlighting all the modelling assumptions and the implication they have in the final result.
The final model to be controlled is then

$$\begin{cases} m\dot{V}_b + \omega_b \times (mV_b) = F_{ext} & \text{(2.78a)} \\ I_n\dot{\omega}_b + \omega_b \times (I_n\omega_b) = M_{ext} & \text{(2.78b)} \end{cases}$$

where the total forces and moments, F_{ext} and M_{ext} respectively, can be summarized as:

$$\begin{bmatrix} F_X \\ F_Y \\ F_Z \end{bmatrix} = \sum T_i \begin{bmatrix} -S_{a_i} C_{b_i} \\ S_{b_i} \\ -C_{a_i} C_{b_i} \end{bmatrix} + mg \begin{bmatrix} -S_\Theta \\ S_\Psi C_\Theta \\ C_\Psi C_\Theta \end{bmatrix} + \begin{bmatrix} -0.5\rho S_x V_{ux} ||V_{tot}|| \\ -0.5\rho S_y V_{vy} ||V_{tot}|| \\ -0.5\rho S_z V_{wz} ||V_{tot}|| \end{bmatrix},$$

$$\begin{bmatrix} L \\ M \\ N \end{bmatrix} = \sum l_i T_i \begin{bmatrix} S_{b_i} \\ S_{a_i} C_{b_i} \\ 0 \end{bmatrix} + \sum K_\beta \begin{bmatrix} b_i \\ a_i \\ 0 \end{bmatrix} + \begin{bmatrix} 0 \\ 0 \\ Q_{up} - Q_{low} \end{bmatrix} +$$

$$+ 0.5\rho \begin{bmatrix} A_x C_{lp} V_{ux} p \\ A_y C_{mq} V_{vy} q \\ A_z C_{nr} V_{wz} w \end{bmatrix} + \begin{bmatrix} Y_{cp}|F_{aero}|_Z - Z_{cp}|F_{aero}|_Y \\ Z_{cp}|F_{aero}|_X - X_{cp}|F_{aero}|_Z \\ X_{cp}|F_{aero}|_Y - Y_{cp}|F_{aero}|_X \end{bmatrix}.$$

and the flapping motion of blades is described by

$$\begin{cases} \tau_f \dot{b} = -b - \tau_f p + B_a a_i + B_s B_1 + B_c A_1 & \text{(2.79a)} \\ \tau_f \dot{a} = -a - \tau_f q + A_b b_i - A_s B_1 + A_c A_1 & \text{(2.79b)} \end{cases}$$

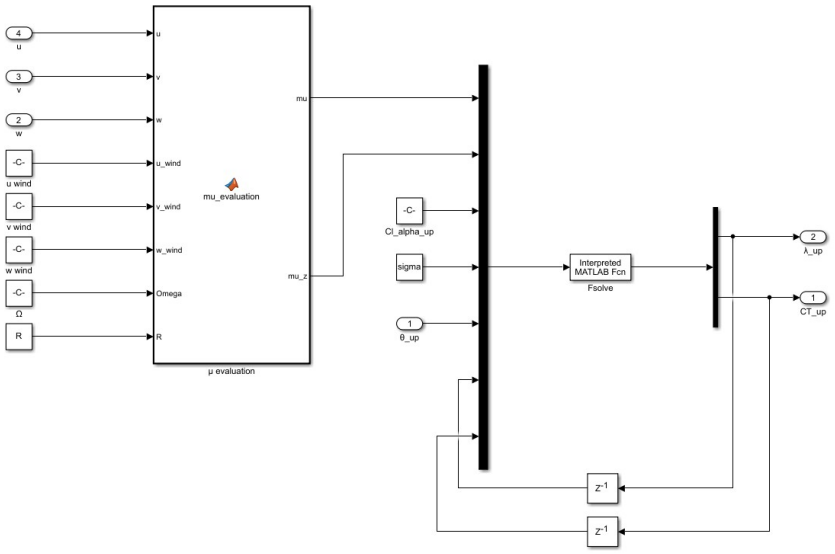

Figure 2.8: Simulink block for evaluation of thrust coefficient

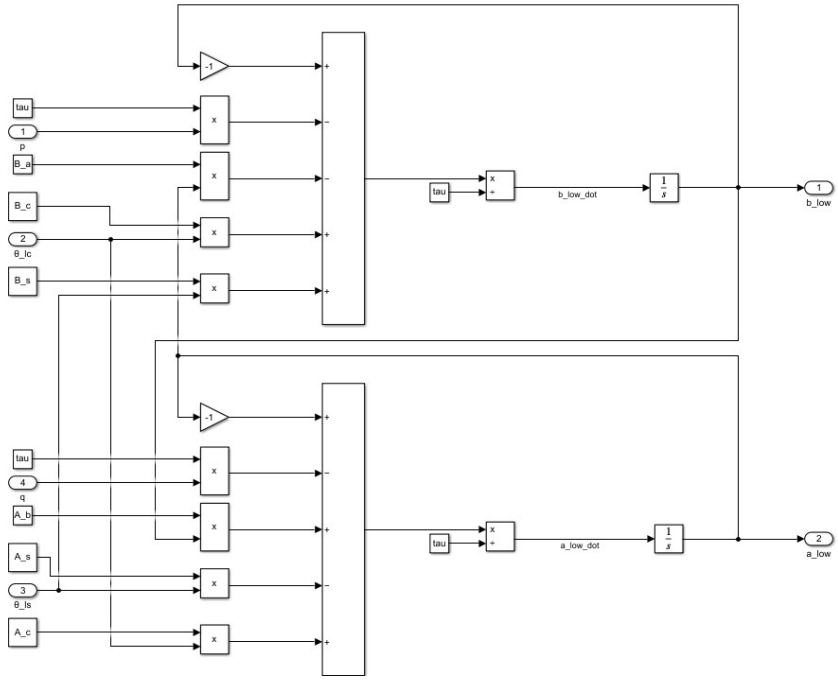

Figure 2.9: Simulink block for evaluation of flapping angles

2.8. Model tuning

In this section, the linearization of the system dynamics around hovering condition is presented. This has a double goal:

1. Use the linearized dynamics at low frequency in order to evaluate the unknown parameters of the nonlinear model, exploiting the numerical values of Ingenuity's stability and control derivatives available [6].
2. Have an adequate model to study the main dynamic characteristics of the system and on which to perform the synthesis of linear control solutions.

The flight dynamics of the system, summarized in Subsection 2.7, can be concisely write as a non-linear function:

$$\dot{x} = f(x, u) \tag{2.80}$$

with $x \in \mathbb{R}^{16}$ and $u \in \mathbb{R}^{6}$.
Eq 2.80 can be linearized around an equilibrium condition, obtaining a state-space model in standard form described by the general equation:

$$\dot{x} = Ax + Bu \tag{2.81}$$

where $A \in \mathbb{R}^{16\times16}$ is the state matrix and $B \in \mathbb{R}^{16\times6}$ is the control matrix.
The state vector is expressed as $x = [x; y; z; \phi; \theta; \psi; u; v; w; p; q; r; a_{up}; b_{up}; a_{low}; b_{low}]$ including NED-frame positions, the attitude Euler angles, body-frame linear velocities, body-frame angular rates and flapping angles of the blades; and the control input vector $u = [\theta_{u0}; \theta_{l0}; \theta_{us}; \theta_{uc}; \theta_{ls}; \theta_{lc}]$ includes the upper and lower collective, followed by the upper and lower cosine cyclic and sine cyclic.
Since we want to replicate the behaviour of the low-order model of Ingenuity proposed in [6], the linearized flight dynamics can be accurately described with only vehicle velocities, attitude, and angular rates as states in the frequency range relevant for control. This approximation is acceptable because of the stiff rotor design leading to a rotor dynamics always far from the desired bandwidth of control system.

This results in a final linearized model expressed as

$$\begin{bmatrix} \dot{u} \\ \dot{v} \\ \dot{w} \\ \dot{\Phi} \\ \dot{\Theta} \\ \dot{\Psi} \\ \dot{p} \\ \dot{q} \\ \dot{r} \end{bmatrix} = A \begin{bmatrix} u \\ v \\ w \\ \Phi \\ \Theta \\ \Psi \\ p \\ q \\ r \end{bmatrix} + B \begin{bmatrix} \theta_{l0} \\ \theta_{lc} \\ \theta_{ls} \\ \theta_{u0} \\ \theta_{uc} \\ \theta_{us} \end{bmatrix} \tag{2.82}$$

where $A \in \mathbb{R}^{9\times9}$ and $B \in \mathbb{R}^{9\times6}$ will be identified in next subsections.

2.8.1. Trimming

In order to estimate the stability and control derivatives of the system, it is necessary first to identify the trimming values of the states.
The hovering condition is chosen as equilibrium point.
In hovering condition the position of the helicopter is constant and all velocites are set to zero resulting in a state vector:

$$x_0 = \begin{bmatrix} u \\ v \\ w \\ \Phi \\ \Theta \\ \Psi \\ p \\ q \\ r \end{bmatrix}_0 = \begin{bmatrix} 0 \\ 0 \\ 0 \\ 0 \\ 0 \\ 0 \\ 0 \\ 0 \\ 0 \end{bmatrix} \tag{2.83}$$

In hovering, the overall thrust produced by the rotor system acts straight up and must equal the weight of the vehicle.
For the coaxial case:

$$T_{up} + T_{low} = mg \tag{2.84}$$

Moreover, the rotors operate at balanced torque

$$Q_{up} - Q_{low} = 0 \tag{2.85}$$

with the lower rotor operating in the vena contracta of the upper rotor.
In this situation, the thrust generated by the lower rotor will be smaller respect than the one produced by the upper rotor.
The thrust ratio can be evaluated analytically once chosen properly one of the primary case shown in [7].
For our model, the rotors operate at balanced torque with the lower rotor operating in the vena contracta of the upper rotor.
Assuming:

1. Close finite spacing between rotors
2. Lower rotor not affecting performance of upper rotor
3. The vena contracta produced by the upper rotor has an area of $A/2$ with slipstream velocity $2v_u$

it results

$$\frac{T_{up}}{T_{low}} = 1.4375 \tag{2.86}$$

The complete study and derivation is shown in [7] and its accuracy has been validated for our model.
Once defined the ratio between the thrusts, it is necessary to evaluate the inflow velocities of both rotors.
In hovering flight, some assumptions can be considered reasonable:

1. The blade is considered to be rigid;
2. The truncation effect at the blade root, tip loss, and flapping hinge extension is neglected and the unsteady effect is neglected;
3. The inflow velocity is considered to be uniformly distributed in the plane of the blade disk.

For upper rotor, basing on the previous assumptions, the inflow equation in hovering condition becomes:

$$\lambda_{up} = \sqrt{\frac{C_{T_{up}}}{2}} \tag{2.87}$$

Since the performance of lower rotor is affected by upper rotor, the expression of λ_{low} cannot be written as Eq. 2.87; thus, it can be determined solving the following system of equations coming from Eqs. 2.84 and 2.86:

$$\begin{cases} C_{T_{up}} + C_{T_{low}} = \dfrac{mg}{\rho\Omega^2 R^2 A} = C_{T_{up}} + 2\lambda_{low}\sqrt{(\lambda_{low} - k\lambda_{up})^2}, & \text{(2.88a)} \\ C_{T_{up}} - C_{T_{low}} = \dfrac{\lambda_{low}}{2} - \dfrac{1+k}{2}\lambda_{up} & \text{(2.88b)} \end{cases}$$

where λ_{low} and k are the only two unknowns.
Onced found the numerical values of thrusts and inflow velocities in hovering condition, the trimming values of collective control inputs can be evaluated from Eqs. 2.60b and 2.61b.
Around equilibrium conditions, the flapping motion of blades is null; setting all velocities and flapping angles equal to zero, from Eq. 2.79, it results clearly that the cyclic control inputs are equal to zero in hovering condition.

$$\theta_{us} = \theta_{ls} = 0 \tag{2.89a}$$

$$\theta_{uc} = \theta_{lc} = 0 \tag{2.89b}$$

All identified trimming values satisfy the nonlinear equilibrium equation:

$$\dot{x} = f(x, u) = 0 \tag{2.90}$$

with $x \in \mathbb{R}^{16}$ and $u \in \mathbb{R}^6$.

2.9. Derivatives evaluation

Since the difficulties to replicate Martian conditions on Earth, the demonstration vehicle has been used for flight dynamics simulations.
As described in Section 1.6, the demonstration vehicle features a full-scale rotor equipped with cyclic control only on the lower rotor (and collective on both rotors); it has a reduced weight in order to simulate gravity on Mars and different values of inertia along the X-, Y-, Z-axis (see Table 1.5). Nevertheless, its flight dynamics is described by the same dynamics model reported in Subsection 2.7.
The resulting linearized system model is defined by a slightly modified form of Eq. 2.82

$$M\dot{\bar{x}} = F\bar{x} + G\bar{u} \tag{2.91}$$

where the state vector is arranged as $\bar{x} = [u; v; w; \Phi; \Theta; \Psi; p; q; r]$ and the input vector is defined as $\bar{u} = [\theta_{s0}; \theta_{lc}; \theta_{ls}; \theta_{a0}]$, where θ_{s0} and θ_{a0} are the symmetric and antisymmetric collective components:

$$\theta_{s0} = \frac{\theta_{u0} + \theta_{l0}}{2}, \quad \theta_{a0} = \frac{\theta_{l0} - \theta_{u0}}{2} \tag{2.92}$$

The matrix

$$M = \begin{pmatrix} m & 0 & 0 & 0 & 0 & 0 & 0 & 0 & 0 \\ 0 & m & 0 & 0 & 0 & 0 & 0 & 0 & 0 \\ 0 & 0 & m & 0 & 0 & 0 & 0 & 0 & 0 \\ 0 & 0 & 0 & 1 & 0 & 0 & 0 & 0 & 0 \\ 0 & 0 & 0 & 0 & 1 & 0 & 0 & 0 & 0 \\ 0 & 0 & 0 & 0 & 0 & 1 & 0 & 0 & 0 \\ 0 & 0 & 0 & 0 & 0 & 0 & I_{xx} & 0 & 0 \\ 0 & 0 & 0 & 0 & 0 & 0 & 0 & I_{yy} & 0 \\ 0 & 0 & 0 & 0 & 0 & 0 & 0 & 0 & I_{zz} \end{pmatrix} \tag{2.93}$$

is the inertial matrix of the helicopter.

The matrices

$$F = \begin{pmatrix} X_u & X_v & X_w & 0 & -mgC_{\bar{\Theta}} & 0 & X_p & X_q - \bar{w} & X_r + \bar{v} \\ Y_u & Y_v & Y_w & mgC_{\bar{\Phi}}C_{\bar{\Theta}} & -mgS_{\bar{\Phi}}S_{\bar{\Theta}} & 0 & Y_p + \bar{w} & Y_q & Y_r - \bar{u} \\ Z_u & Z_v & Z_w & -mgS_{\bar{\Phi}}C_{\bar{\Theta}} & -mgC_{\bar{\Phi}}S_{\bar{\Theta}} & 0 & Z_p - \bar{v} & Z_q + \bar{u} & Z_r \\ 0 & 0 & 0 & 0 & 0 & 0 & 1 & S_{\bar{\Phi}}T_{\bar{\Theta}} & C_{\bar{\Phi}}T_{\bar{\Theta}} \\ 0 & 0 & 0 & 0 & 0 & 0 & 0 & C_{\bar{\Phi}} & -S_{\bar{\Phi}} \\ 0 & 0 & 0 & 0 & 0 & 0 & 0 & S_{\bar{\Phi}}/C_{\bar{\Theta}} & C_{\bar{\Phi}}/C_{\bar{\Theta}} \\ L_u & L_v & L_w & 0 & 0 & 0 & L_p & L_q & L_r \\ M_u & M_v & M_w & 0 & 0 & 0 & M_p & M_q & M_r \\ N_u & N_v & N_w & 0 & 0 & 0 & N_p & N_q & N_r \end{pmatrix},$$

$$G = \begin{pmatrix} X_{S0} & X_{LC} & X_{LS} & X_{A0} \\ Y_{S0} & Y_{LC} & Y_{LS} & Y_{A0} \\ Z_{S0} & Z_{LC} & Z_{LS} & Z_{A0} \\ 0 & 0 & 0 & 0 \\ 0 & 0 & 0 & 0 \\ 0 & 0 & 0 & 0 \\ L_{S0} & L_{LC} & L_{LS} & L_{A0} \\ M_{S0} & M_{LC} & M_{LS} & M_{A0} \\ N_{S0} & N_{LC} & N_{LS} & N_{A0} \end{pmatrix} \tag{2.94}$$

are respectively the matrices containing the stability derivatives and the control derivatives of the system.
$[\bar{u};\bar{v};\bar{w}]$ are the the body-frame trim velocities and $\bar{\Phi}$ and $\bar{\Theta}$ are the trim roll and pitch attitudes. All these trim values are equal to zero as seen before.

2.9.1. Stability derivatives

The stability derivatives of the system can be modeled taking the partial derivative of dynamics equation respect to each state and substituting the trim parameters:

$$F = \left[\frac{\partial f}{\partial x}\right]_{x_0,u_0} = \begin{pmatrix} \frac{\partial f_1}{\partial x_1} & \cdots & \frac{\partial f_1}{\partial x_n} \\ \vdots & \vdots & \vdots \\ \frac{\partial f_n}{\partial x_1} & \cdots & \frac{\partial f_n}{\partial x_n} \end{pmatrix}_{x_0,u_0} \in \mathbb{R}^{9\times 9} \tag{2.95}$$

Defining:

$$\begin{bmatrix} f_1 \\ f_2 \\ f_3 \\ f_7 \\ f_8 \\ f_9 \end{bmatrix} = \begin{bmatrix} -T_{low}S_aC_b - mgS_\Theta - |F_{aero}|_X \\ T_{low}S_b + mgS_\Phi C_\Theta - |F_{aero}|_Y \\ -T_{up} - T_{low}C_aC_b + mgC_\Phi C_\Theta - |F_{aero}|_Z \\ l_{low}T_{low}S_b + K_\beta b + |M_{aero}|_X \\ l_{low}T_{low}S_aC_b + K_\beta a + |M_{aero}|_Y \\ Q_{up} - Q_{low} + |M_{aero}|_Z \end{bmatrix} \tag{2.96}$$

the parameters dependent stability derivatives of our model are expressed as:

$$X_u = \left[\frac{\partial f_1}{\partial u}\right]_{x_0,u_0} = -\frac{\rho S_x\sqrt{V_{prop}}}{2} \tag{2.97}$$

$$X_q = \left[\frac{\partial f_1}{\partial q}\right]_{x_0,u_0} = -\frac{\rho S_x Z_{cp}\sqrt{V_{prop}^2}}{2} \tag{2.98}$$

$$Y_v = \left[\frac{\partial f_2}{\partial v}\right]_{x_0,u_0} = -\frac{\rho S_y\sqrt{V_{prop}}}{2} \tag{2.99}$$

$$Y_p = \left[\frac{\partial f_2}{\partial p}\right]_{x_0,u_0} = \frac{\rho S_y Z_{cp}\sqrt{V_{prop}^2}}{2} \tag{2.100}$$

$$Z_w = \left[\frac{\partial f_3}{\partial w}\right]_{x_0,u_0} = -\frac{\rho S_z\sqrt{V_{prop}^2}}{2} - \frac{\rho S_z V_{prop}^2}{2\sqrt{V_{prop}}} \tag{2.101}$$

$$L_v = \left[\frac{\partial f_7}{\partial v}\right]_{x_0,u_0} = \frac{\rho S_y Z_{cp}\sqrt{V_{prop}^2}}{2} \tag{2.102}$$

$$L_p = \left[\frac{\partial f_7}{\partial p}\right]_{x_0,u_0} = -\frac{\rho S_y Z_{cp}^2\sqrt{V_{prop}^2}}{2} \tag{2.103}$$

$$M_u = \left[\frac{\partial f_8}{\partial u}\right]_{x_0,u_0} = -\frac{\rho S_x Z_{cp}\sqrt{V_{prop}^2}}{2} \tag{2.104}$$

$$M_q = \left[\frac{\partial f_8}{\partial q}\right]_{x_0,u_0} = -\frac{\rho S_x Z_{cp}^2\sqrt{V_{prop}^2}}{2} \tag{2.105}$$

$$N_r = \left[\frac{\partial f_9}{\partial r}\right]_{x_0,u_0} = \frac{\rho C_{nr} A_z V_{prop}}{2} \tag{2.106}$$

where

$$V_{prop} = \sqrt{\frac{|T_{low}|}{2\rho\pi R^2}} \tag{2.107}$$

Note that we have reported only non-null derivatives.

Since not all physical parameters of Ingenuity were known from the available literature, the goal was to evaluate them obtaining stability derivatives as close as possible to the ones reported in [6] and ensuring then their validity. Looking at the expressions of the stability derivatives, the assumed parameters known were ρ and V_{prop} (its numerical value can be extrapolated from Eq. 2.107 in hovering condition); instead, the system parameters to identify are the drag areas S_i, the body coordinates of center of pressure (X_{cp}, Y_{cp}, Z_{cp}) and the aerodynamic damping moment coefficient C_{nr} .

For example, from Eq. 2.97, the effective drag area S_x has been extrapolated knowing the desired value X_u and substituting the other known parameters of the system

$$S_x = -\frac{2X_u}{\rho\sqrt{V_{prop}}} \tag{2.108}$$

The same procedure has been followed for evaluate S_z, Z_{cp} and C_{nr}.

Note that for the symmetry of the vehicle $S_x = S_y$ and $X_{cp} = Y_{cp} = 0$.

Substituting all the physical parameters of the system in the expression of stability derivatives, the matrix F becomes

$$F = \begin{pmatrix} -0.03 & 0 & 0 & 0 & -7.54 & 0 & 0 & 0.005 & 0 \\ 0 & -0.03 & 0 & 7.54 & 0 & 0 & -0.005 & 0 & 0 \\ 0 & 0 & -0.13 & 0 & 0 & 0 & 0 & 0 & 0 \\ 0 & 0 & 0 & 0 & 0 & 0 & 1 & 0 & 0 \\ 0 & 0 & 0 & 0 & 0 & 0 & 0 & 1 & 0 \\ 0 & 0 & 0 & 0 & 0 & 0 & 0 & 0 & 1 \\ 0 & -0.005 & 0 & 0 & 0 & 0 & -8.34\text{e}{-4} & 0 & 0 \\ 0.005 & 0 & 0 & 0 & 0 & 0 & 0 & -8.34\text{e}{-4} & 0 \\ 0 & 0 & 0 & 0 & 0 & 0 & 0 & 0 & -0.006 \end{pmatrix}$$

2.9.2. Control derivatives

The evaluation of control derivatives is very important for the development of the control system.
Their computation is similar to that of stability derivatives, but in this case each dynamics equation is partially derived respect to each control input variable

$$G = \left[\frac{\partial f}{\partial u}\right]_{x_0,u_0} = \begin{pmatrix} \frac{\partial f_1}{\partial u_{s0}} & \frac{\partial f_1}{\partial u_{lc}} & \frac{\partial f_1}{\partial u_{ls}} & \frac{\partial f_1}{\partial u_{a0}} \\ \vdots & \vdots & \vdots & \vdots \\ \frac{\partial f_n}{\partial u_{s0}} & \frac{\partial f_n}{\partial u_{lc}} & \frac{\partial f_n}{\partial u_{ls}} & \frac{\partial f_n}{\partial u_{a0}} \end{pmatrix}_{x_0,u_0} \in \mathbb{R}^{9\times 4} \tag{2.109}$$

Since the dynamics' equations do not depend directly on cyclic control inputs but on flapping angles, it is necessary first to rearrange Eq. 2.79.
At equilibrium one has

$$\begin{cases} a = A_b b - A_s B_1 + A_c A_1 & \text{(2.110a)} \\ b = -B_a a + B_s B_1 + B_c A_1 & \text{(2.110b)} \end{cases}$$

Substituting Eq. 2.110b in Eq. 2.110a leads to

$$a = \frac{1}{1 + A_b B_a}\left((A_b B_s - A_s)B_1 + (A_b B_c + A_c)A_1\right) \tag{2.111}$$

and then

$$b = \frac{1}{1 + A_b B_a}\left((B_a A_s + B_s)B_1 + (B_c - B_a A_c)A_1\right). \tag{2.112}$$

Substituting Eqs. 2.111 and 2.112 in Eq. 2.96, the partial derivatives respect to cyclic controls can be written as:

$$X_{lc} = \left[\frac{\partial f_1}{\partial \theta_{lc}}\right]_{x_0,u_0} = -\frac{1}{1 + A_b B_a} T_{low}(A_b B_c + A_c) \tag{2.113}$$

$$X_{ls} = \left[\frac{\partial f_1}{\partial \theta_{ls}}\right]_{x_0,u_0} = -\frac{1}{1 + A_b B_a} T_{low}(A_b B_s - A_s) \tag{2.114}$$

$$Y_{lc} = \left[\frac{\partial f_2}{\partial \theta_{lc}}\right]_{x_0,u_0} = \frac{1}{1 + A_b B_a} T_{low}(B_c - B_a A_c) \tag{2.115}$$

$$Y_{ls} = \left[\frac{\partial f_2}{\partial \theta_{ls}}\right]_{x_0,u_0} = \frac{1}{1 + A_b B_a} T_{low}(B_a A_s + B_s) \tag{2.116}$$

$$L_{lc} = \left[\frac{\partial f_7}{\partial \theta_{lc}}\right]_{x_0,u_0} = \frac{1}{1 + A_b B_a}(B_c - B_a A_c)K \tag{2.117}$$

$$L_{ls} = \left[\frac{\partial f_7}{\partial \theta_{ls}}\right]_{x_0,u_0} = \frac{1}{1 + A_b B_a}(B_a A_s + B_s)K \tag{2.118}$$

$$M_{lc} = \left[\frac{\partial f_8}{\partial \theta_{lc}}\right]_{x_0,u_0} = \frac{1}{1+A_bB_a}(A_bB_c + A_c)K \tag{2.119}$$

$$M_{ls} = \left[\frac{\partial f_8}{\partial \theta_{ls}}\right]_{x_0,u_0} = \frac{1}{1+A_bB_a}(A_bB_s - A_s)K \tag{2.120}$$

where K is a parameter including the effective spring constant K_β , T_{low} and l_{low} .
On the other hand, the non-null derivatives respect to collective angles are:

$$Z_{s0} = \left[\frac{\partial f_3}{\partial \theta_{s0}}\right]_{x_0,u_0} = -\frac{A\Omega^2R^2\rho\sigma}{6}(C_{l_{\alpha,up}} + C_{l_{\alpha,low}}) \tag{2.121}$$

$$Z_{a0} = \left[\frac{\partial f_3}{\partial \theta_{a0}}\right]_{x_0,u_0} = \frac{A\Omega^2R^2\rho\sigma}{6}(C_{l_{\alpha,up}} - C_{l_{\alpha,low}}) \tag{2.122}$$

$$N_{s0} = \left[\frac{\partial f_9}{\partial \theta_{s0}}\right]_{x_0,u_0} = \frac{A\Omega^2R^3}{6}(\rho\sigma\lambda_{up}C_{l_{\alpha,up}} - \lambda_{low}C_{l_{\alpha,low}}) \tag{2.123}$$

$$N_{a0} = \left[\frac{\partial f_9}{\partial \theta_{a0}}\right]_{x_0,u_0} = -\frac{A\Omega^2R^3}{6}(\rho\sigma\lambda_{up}C_{l_{\alpha,up}} + \lambda_{low}C_{l_{\alpha,low}}) \tag{2.124}$$

In the previous expressions of control derivatives, not all system parameters are known; in particular, ρ, A, Ω, R, σ and l_{low} are known from literature (see Table 1.1). T_{low}, λ_{up} and λ_{low} were previously evaluated for hovering condition (see Subsection 2.8.1). The only unknowns are the parameters related to the flapping motion of the blades (A_b, B_a, A_c, B_c, A_s, B_s), the parameter K and the bidimensional lift-curve slope for both rotors ($C_{l_{\alpha,up}}$ and $C_{l_{\alpha,low}}$).
In order to evaluate the unknown parameters, a system of eight equations in seven unknowns is built imposing the expression of partial derivatives respect to cyclic controls equal to the desired control derivatives (adjusting the signs according to the conventions adopted for reference system).

$$\begin{cases} -3.079n(A_bB_c + A_c) = [X_{lc}]_d \\ -3.079n(A_bB_s - A_s) = [X_{ls}]_d \\ 3.079n(B_c - B_aA_c) = [Y_{lc}]_d \\ 3.079n(B_aA_s + B_s) = [Y_{ls}]_d \\ nK(B_c - B_aA_c) = [L_{lc}]_d \\ nK(B_aA_s + B_s) = [L_{ls}]_d \\ nK(A_bB_c + A_c) = [M_{lc}]_d \\ nK(A_bB_s - A_s) = [M_{ls}]_d \end{cases} \tag{2.125}$$

where

$$n = \frac{1}{1 + A_b B_a} \tag{2.126}$$

System 2.125 is solved using nonlinear least-squares methods implemented in MATLAB function *fsolve* using as starting points the values expected from flapping dynamics derivation exposed in Section 2.5 (see results in Table 2.1).
Using the same procedure, the average value of $C_{l_{\alpha,up}}$ and $C_{l_{\alpha,low}}$ is evaluated from Eqs. 2.121 and 2.122 (Table 2.2).
Substituting all rotor parameters in the expression of control derivatives, the matrix G becomes

$$G = \begin{pmatrix} 0 & -3.87 & 0.48 & 0 \\ 0 & -0.76 & -3.87 & 0 \\ -42.39 & 0 & 0 & -7.73 \\ 0 & 0 & 0 & 0 \\ 0 & 0 & 0 & 0 \\ 0 & 0 & 0 & 0 \\ 0 & -1.19 & -6.09 & 0 \\ 0 & 6.08 & -0.75 & 0 \\ 0.044 & 0 & 0 & -1.29 \end{pmatrix} \tag{2.127}$$

In a linearized model, forces and moments are instantaneous and proportional to the control inputs with a gain equal to the corresponding control derivative.
Matrix 2.127 shows clearly how rotor forces and moments along Z body-axis are proportional only to collective inputs and, vice versa, forces and moments along X and Y body-axis are proportional only to cyclic inputs.

Parameter	**Physical meaning**
$A_b = 0.6428$	Coupling term
$B_a = -0.1755$	Coupling term
$A_c = 1.4135$	Coefficient multiplied for longitudinal cyclic control (Eq. 2.79b)
$B_c = -0.4660$	Coefficient multiplied for longitudinal cyclic control (Eq. 2.79a)
$A_s = -0.6524$	Coefficient multiplied for lateral cyclic control (Eq. 2.79b)
$B_s = -1.2290$	Coefficient multiplied for lateral cyclic control (Eq. 2.79a)
$K_\beta = 4.5680\ Nm/rad$	Effective spring constant

Table 2.1: Flapping parameters derived from control derivatives

Parameter	Physical meaning
$C_{l_{\alpha,up}} = 1.2867$	Bidimensional lift-curve slope for upper rotor
$C_{l_{\alpha,low}} = 1.8606$	Bidimensional lift-curve slope for lower rotor

Table 2.2: Rotor parameters derived from control derivatives

2.9.3. Comparison with Ingenuity

Since we want to have a dynamic behavior of our model comparable to that of Ingenuity in the vicinity of the hovering point at low frequency and not all derivatives of model match perfectly the numerical values reported in [6], the strategy adopted is to compare the two systems using the MATLAB function *gapmetric*.
The function

$$[\text{gap}, \text{nugap}] = gapmetric(P_1, P_2) \tag{2.128}$$

computes the gap and Vinnicombe (ν-gap) metrics for the distance between two dynamic systems P_1 and P_2. The gap metric values satisfy $0 \leq \text{nugap} \leq \text{gap} \leq 1$. Values close to zero imply that any controller that stabilizes P_1 also stabilizes P_2 with similar closed-loop gains.
The result of this analysis is a gap between Ingenuity dynamic system and our model dynamic system of 0.57.
Since the great influence on control system is given by the control derivatives of system, in order to investigate the great gap obtained, it is necessary to look at the two G matrices of the systems

$$G_{Ingenuity} = \begin{pmatrix} 0 & -3.84 & 0.37 & 0 \\ 0 & -0.74 & -3.91 & 0 \\ -42.39 & 0 & 0 & -7.73 \\ 0 & 0 & 0 & 0 \\ 0 & 0 & 0 & 0 \\ 0 & 0 & 0 & 0 \\ 0 & -1.20 & -6.06 & 0 \\ 0 & 6.10 & -0.82 & 0 \\ 0 & 0 & 0 & -4.81 \end{pmatrix}, \tag{2.129}$$

$$G_{model} = \begin{pmatrix} 0 & -3.87 & 0.48 & 0 \\ 0 & -0.76 & -3.87 & 0 \\ -42.39 & 0 & 0 & -7.73 \\ 0 & 0 & 0 & 0 \\ 0 & 0 & 0 & 0 \\ 0 & 0 & 0 & 0 \\ 0 & -1.19 & -6.09 & 0 \\ 0 & 6.08 & -0.75 & 0 \\ 0.044 & 0 & 0 & -1.29 \end{pmatrix} \tag{2.130}$$

As shown in Eq. 2.130, the great difference between the two matrices is given by the numerical value of control derivative N_{a0} (the term contoured in red); this is about four times smaller respect the value reported in Ingenuity's scientific paper.
This can be explained looking at the expression of N_{a0}

$$N_{a0} = -\frac{A\Omega^2 R^3}{6}(\rho\sigma\lambda_{up}C_{l_{\alpha,up}} + \lambda_{low}C_{l_{\alpha,low}}) \tag{2.131}$$

it appears clearly that a great contribution is given by the value of λ_{low} at equilibrium; this strictly depends on the considerations carried out in hovering condition, in particular in term of thrust ratio and assumptions adopted (see Subsection 2.8.1).
Since we are mostly interested in control the position of the UAV, we can neglect the difference between N_{a0} values and the gap between the two dynamics systems is reduced to 0.02.
The only parameter left to be identified is the rotor time constant τ_f; this coefficient has been chosen so that the first frequency of our model is the same of the one reported in literature for Ingenuity demonstration vehicle, in which the first frequency is about 12 Hz [5]. As shown in Fig. 2.10, the open-loop poles of the complete hover dynamics of the demonstration vehicle (including rotor dynamics) have been plotted once identified τ_f; as expected from the high stiffness of the rotors, the poles related to flapping dynamics (the two complex poles on the left of the graphic at a frequency above 10 Hz) are located far from the poles of the low-frequency dynamics.
The responses in open loop of our model's rotor system to collective and cyclic step inputs are shown in the following figures. In particular, Fig. 2.11 illustrates the response of vertical force to symmetric and antisymmetric collective step inputs: three-second steps of 2 deg in the asymmetric collective (negative, then positive) are followed by three-second steps of 2 deg in the symmetric collective (positive, then negative).
Fig. 2.12 shows the responses of roll and pitch torques to steps in the cyclic channels: three-second steps of 5 deg in θ_{1c} (positive, then negative) are followed by similar steps

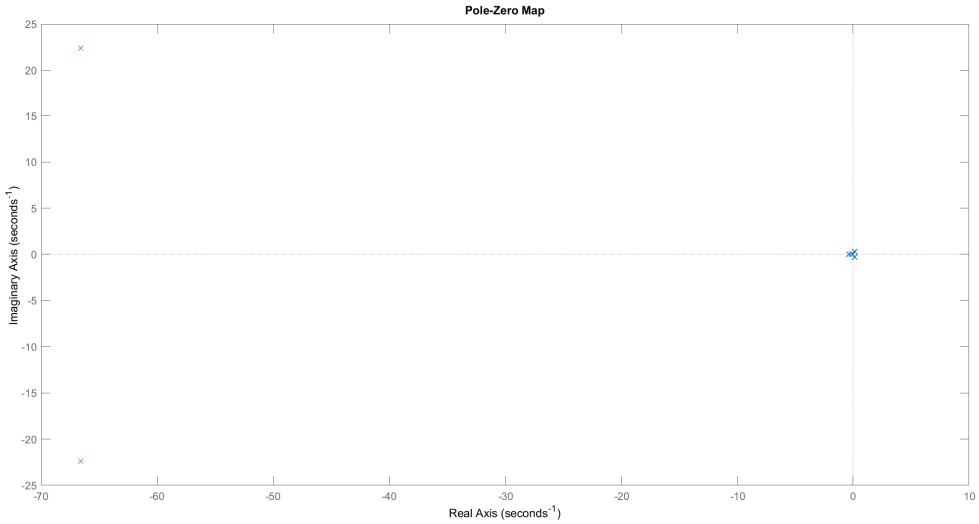

Figure 2.10: Poles of the complete dynamics of the demonstration vehicle

in θ_{1s}. The responses obtained are close to those of the real system as reported in [6].

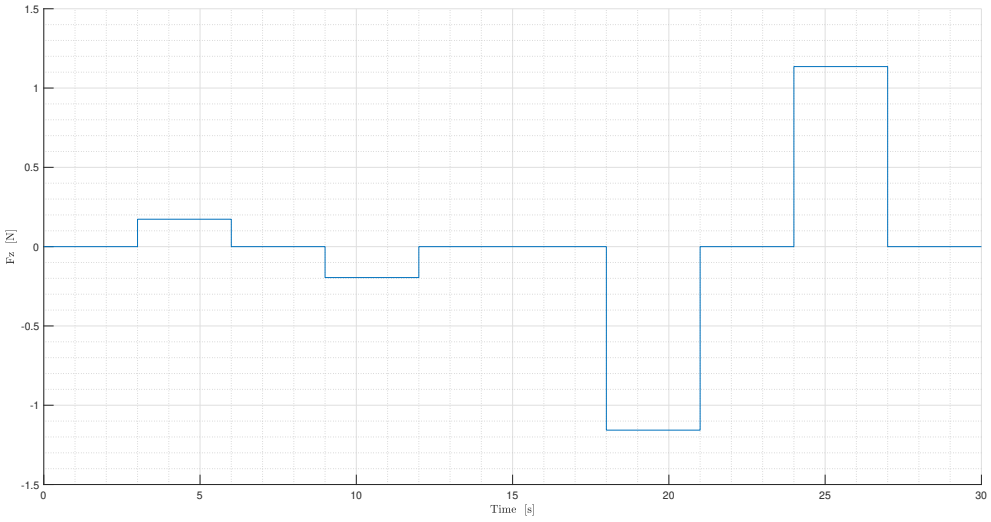

Figure 2.11: Open loop response of vertical force to steps in the collective channels

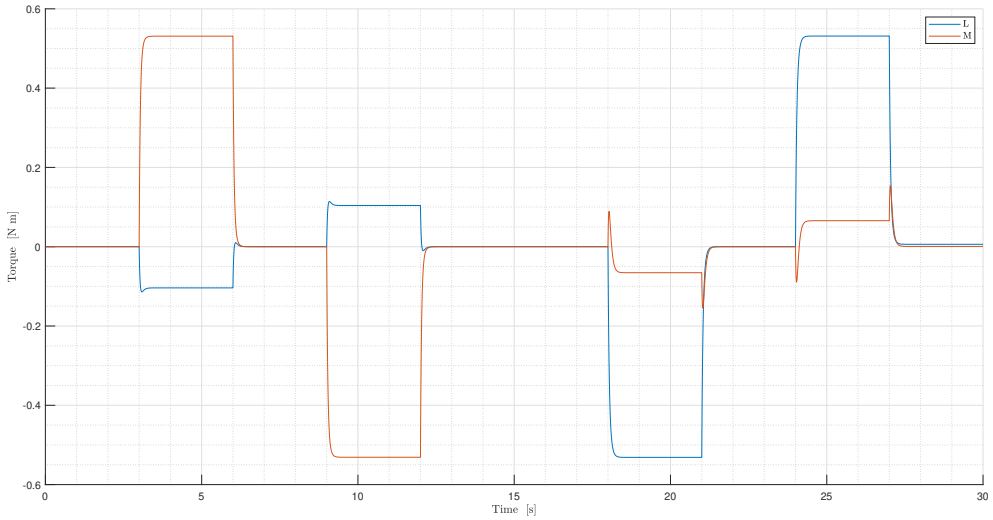

Figure 2.12: Open loop response of roll and pitch torques to steps in the cyclic channels

3 | Vehicle control system

The linearized model presented in the previous chapter is now used to develop control laws for the position and attitude control of the Mars helicopter.
The development of the control system starts with the implementation of the linear control system taken from baseline by replicating the architecture proposed in the literature [5] for Ingenuity; this is useful to see the responses of our model to simple commands and its behavior near hovering conditions. Limitations of the linear architecture are highlighted when considering large maneuvers and large magnitude disturbances.
After deriving a suitable nonlinear-control oriented model for the Mars Helicopter, the design of a nonlinear control architecture leads to an improvement of results far from hovering point and to the possibility of making the UAV follow more complex trajectories. Beyond the complex and uncertain nonlinear dynamics, one of the main challenges in deriving control laws for the system under consideration is the underactuation, which is clearly visible by inspecting the input matrix G, which has rank 4.

3.1. Baseline controller

The overall baseline control architecture, as presented in [5], is illustrated in Fig. 3.1, which mirrors typical cascade control architectures used also on Earth form small scale helicopters.
The main blocks are:

1. **Heave** controller based on a PID-type controller
2. **Yaw** angle controller based on a PID-type controller
3. **Horizontal position** controller is composed by a nested architecture. An inner loop is formed by independently controlling roll and pitch with PD-type controllers. Input to the inner loop is set by an outer loop, which is formed by controlling the horizontal position using PID-type controllers. The horizontal position is represented in a local ground frame, whereas the roll and pitch angles are the angles of the body frame relative to gravity; therefore, the output of the outer loop is rotated

by the yaw angle before being used as a reference by the inner loop.

4. **Mixer** to decouple control inputs
5. **Plant** which contains all dynamics equations taking as inputs the cyclic and collective controls and giving in output the states of the system

As mentioned above, the baseline controller proposed in the literature [5] is based on a simplified model that accounts only for large rotations about the z-axis. Specifically, based on the nonlinear translational model (including only the propulsive force)

$$m\dot{v}_x = (cos(\phi)sin(\theta)cos(\psi) + sin(\phi)sin(\psi))T_c \tag{3.1a}$$

$$m\dot{v}_y = (cos(\phi)sin(\theta)sin(\psi) - sin(\phi)cos(\psi))T_c \tag{3.1b}$$

assuming near hovering conditions lead to

$$m\begin{bmatrix}\dot{v}_x\\ \dot{v}_y\end{bmatrix} = -mg\begin{bmatrix}cos(\psi)sin(\psi)\\ -cos(\psi)sin(\psi)\end{bmatrix}\begin{bmatrix}\theta\\ \phi\end{bmatrix} = -mgT(\psi)\begin{bmatrix}\theta\\ \phi\end{bmatrix} \tag{3.2}$$

To control the (underactued) translational motion, one can use the roll and pitch angles as virtual inputs, given that the attitude dynamics is fully actuated. Setting $\theta = \theta_v$, $\phi = \phi_v$, since matrix $T(\psi)$ is invertible, it is possible to decouple the two equations by using

$$\begin{bmatrix}\theta_v\\ \phi_v\end{bmatrix} = T(\psi)^{-1}\begin{bmatrix}\tilde{\theta}_v\\ \tilde{\phi}_v\end{bmatrix} \tag{3.3}$$

so that

$$m\dot{v}_x = -mg\tilde{\theta}_v \tag{3.4a}$$

$$m\dot{v}_y = -mg\tilde{\phi}_v \tag{3.4b}$$

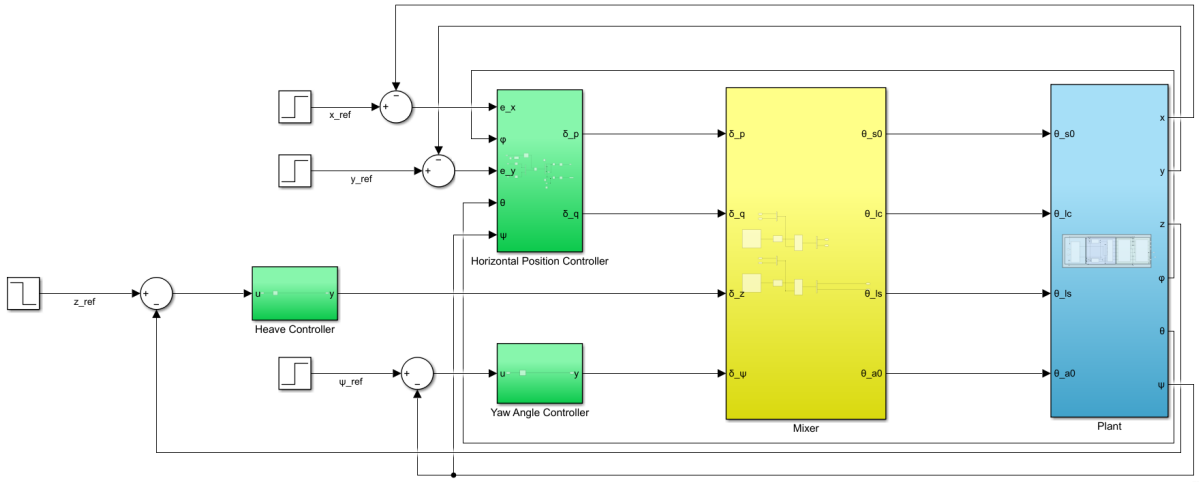

Figure 3.1: Baseline control architecture (SIMULINK representation)

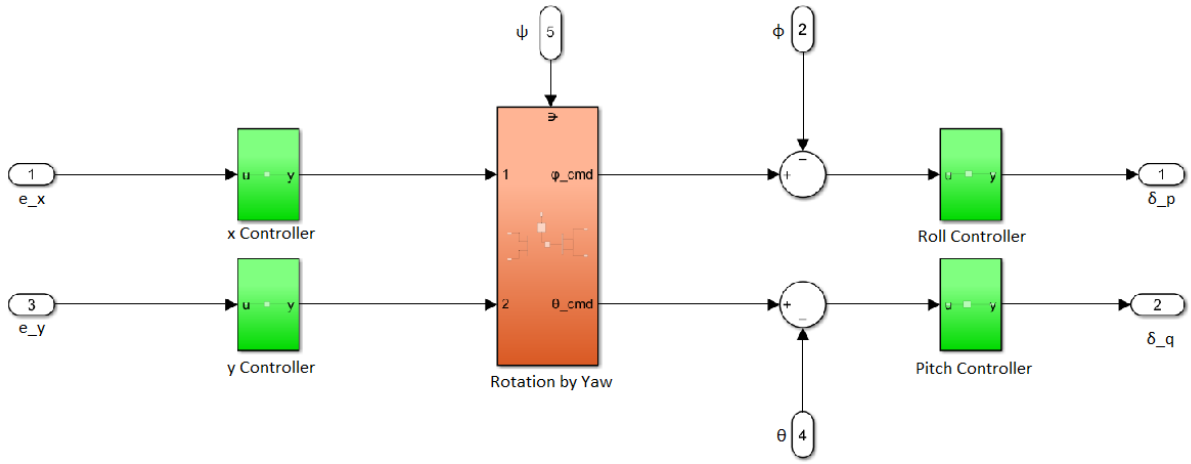

Figure 3.2: Nested architecture for horizontal position controller

3.1.1. Input mixing

The first step for the design of control system is the selection of collective and cyclic mixing matrices to decouple control inputs.

For control of heave and yaw, the mixing matrix M_{col} is selected such that

$$\begin{bmatrix} \theta_{s0} \\ \theta_{a0} \end{bmatrix} = M_{col}^{-1} \begin{bmatrix} \delta_z \\ \delta_\psi \end{bmatrix} \tag{3.5}$$

where δ_z and δ_ψ are respectively the heave-aligned input and yaw-aligned input.
Eq. 3.5 is verified for a mixing matrix defined as:

$$M_{col} = \begin{pmatrix} Z_{s0} & Z_{a0} \\ N_{s0} & N_{a0} \end{pmatrix} \tag{3.6}$$

where Z_{s0}, Z_{a0}, N_{s0} and N_{a0} are the control derivatives evaluated during linearization as partial derivatives of dynamics equations respect to collective angles (third row and ninth row of matrix 2.127).
The mixing matrix M_{cyc} for roll and pitch control has been selected in a similar way:

$$\begin{bmatrix} \theta_{lc} \\ \theta_{ls} \end{bmatrix} = M_{cyc}^{-1} \begin{bmatrix} \delta_p \\ \delta_q \end{bmatrix} \tag{3.7}$$

where δ_p and δ_q are respectively the roll-aligned input and pitch-aligned input.
The mixing matrix M_{cyc} is

$$M_{cyc} = \begin{pmatrix} L_{lc} & L_{ls} \\ M_{lc} & M_{ls} \end{pmatrix} \tag{3.8}$$

where L_{lc}, L_{ls}, M_{lc} and M_{ls} are the control derivatives evaluated during linearization as partial derivatives of dynamics equations respect to cyclic angles (seventh row and eighth row of matrix 2.127).

3.1.2. Control requirements and tuning

Once the system has been decoupled into several subsystem thanks to the mixing, the next step is the design of each single PID- and PD-type controllers according to the architecture described above.
The first tuning is performed taking the same control architecture illustrated in Fig. 3.1 and considering as plant the linearized system model expressed in Eq. 2.91; this procedure allows to have a simple design of controllers and to obtain good results for nonlinear case near equilibrium point.
Since the mixer allows to obtain heave and yaw dynamics that are decoupled from each other and, due to the values of other stability and control derivatives in hover, the rest of the system, for both heave and yaw, PID-type controllers can be designed with relative ease.
Basing on stability analysis carried out by [5], for the heave loop, a controller with crossover frequency of 1.2 Hz was designed, with stability margins of 15.5 dB and 60°.
For the yaw loop, a controller with crossover frequency of 1.9 Hz was designed, with sta-

bility margins of 10.2 dB and 58°.
The cyclic inputs, coming out from the mixer, will result in pure roll and pitch moments according to the model, although coupling still exists due to the stability derivatives and the translational control derivatives; this coupling leads, together with the nested architecture, to a more complex design of controllers for roll and pitch.
The inner loop is designed by eliminating the translational degrees of freedom and designing for the system restricted to roll and pitch.
The inner loop has a crossover frequency of 2.6 Hz and exhibits margins of 9.3 dB and 60° [5].
The outer loop is designed by closing the inner loop and treating the pitch angle as the control input for longitudinal translational control and the roll angle as the control input for lateral translational control.
The outer loop has a crossover frequency of 0.3 Hz, with margins of 15.6 dB and 56°.
The robustness of the resulting system has been checked performing first the Nichols charts for each loop, introducing a perturbation at each channel independently.
For heave and yaw loop, the plots are reported in Figs. 3.3 and 3.4 together with the values of minimum stability margins.

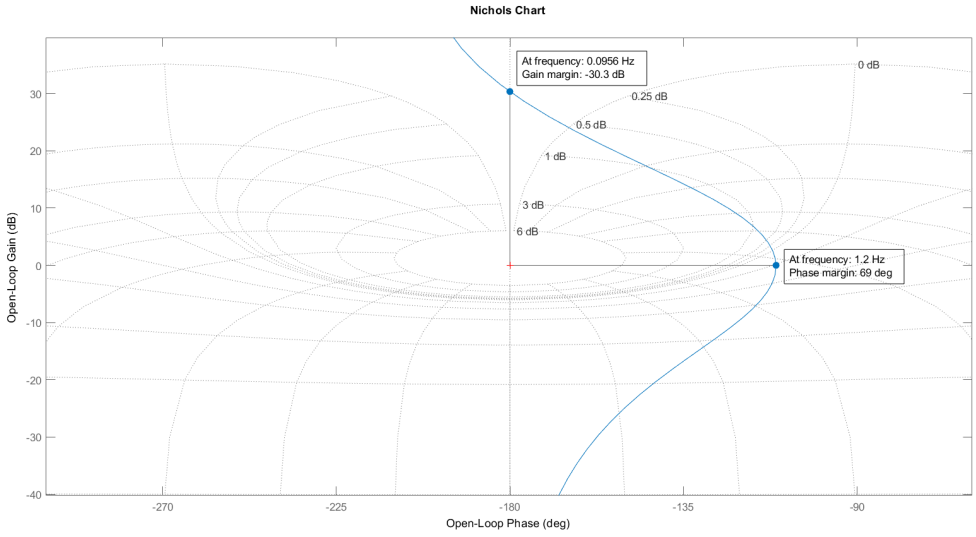

Figure 3.3: Nichols chart for heave loop

Figs. 3.3 and 3.4 show that the curve of the magnitude-vs-phase plot is always far from the critical point and from the minimum requirements for stability (defined as margins of 6 dB and 30° [5]) meaning a good robustness of the system to perturbations.
Moreover, the curve of the magnitude-vs-phase plot passes only above the critical point meaning that a reduction in gain will reduce the gain margin and eventually destabilize

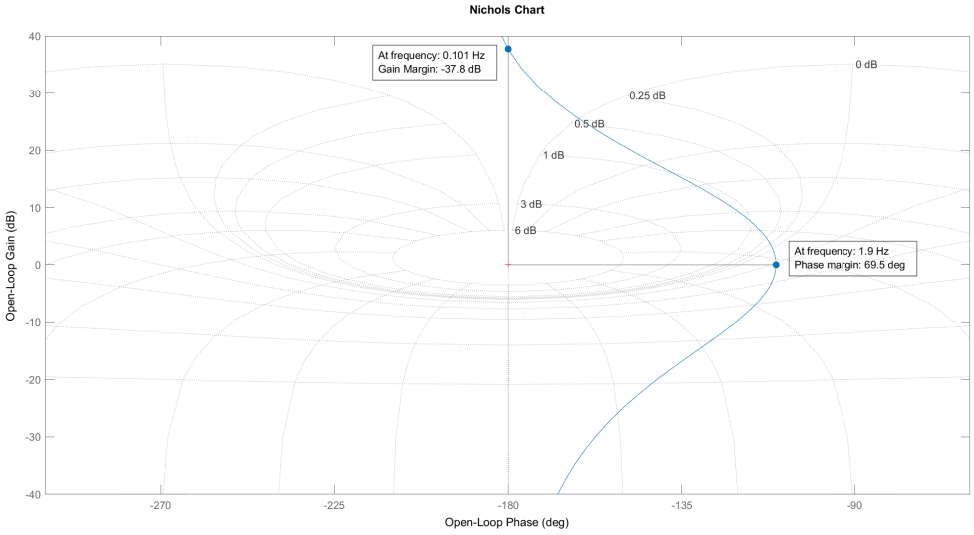

Figure 3.4: Nichols chart for yaw loop

the system.
As seen for heave and yaw loop, the Nichols charts for inner pitch loop and outer longitudinal translation loop have been investigated (Figs. 3.5 and 3.6).

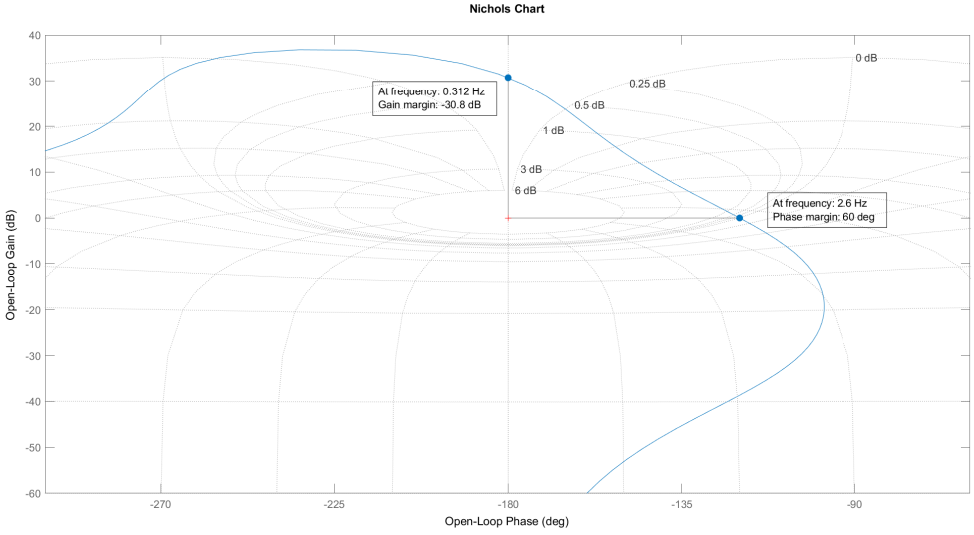

Figure 3.5: Nichols chart for inner pitch loop

Looking at Figs. 3.5 and 3.6, similar considerations done for heave and yaw loop can be made with the only difference for Nichols chart of outer longitudinal translation loop in which the curve of the magnitude-vs-phase plot passes both above and below the critical point, which means that both an increase and a reduction in gain will reduce the gain

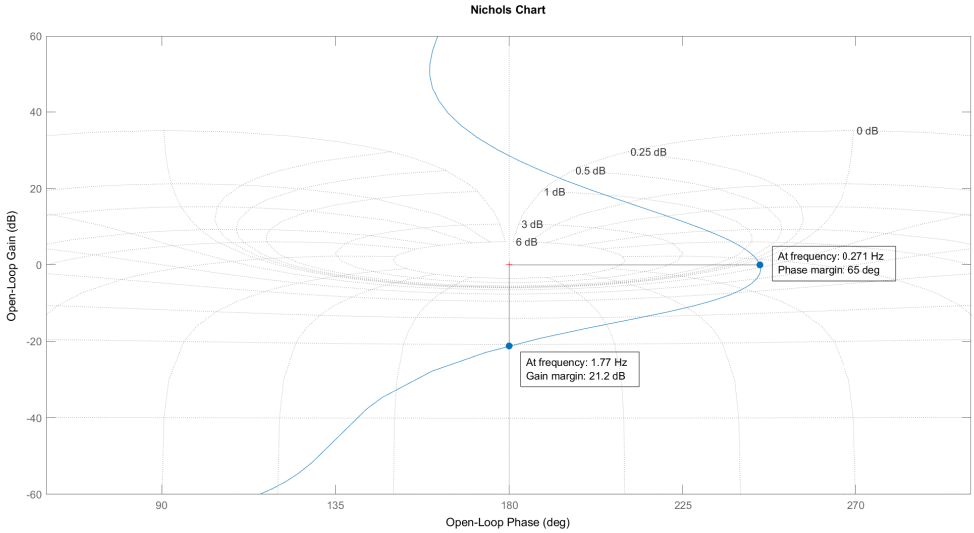

Figure 3.6: Nichols chart for outer longitudinal translation loop

margin and eventually destabilize the system.
Ideally, the sequential design process outlined above would be adequate for designing the nested controller. However, it is possible to design a controller with good stability margins both for the inner loop (with translational dynamics eliminated) and the outer loop (with the inner loop closed) that nevertheless reveals inadequate margins when the loop is opened up at the input point with both controllers in place, as illustrated in Fig. 3.7.

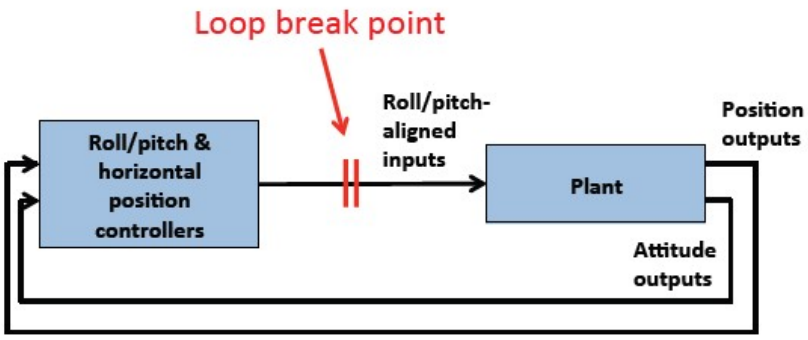

Figure 3.7: Stability is studied by opening the plant at the input point, while leaving the roll/pitch and horizontal translation controllers in place.

Fig. 3.8 shows the Nichols chart for the pitch/longitudinal translation axis when opened at this point. The curve of the magnitude-vs-phase plot remains far from the critical point ensuring the robustness of the system also in this condition.

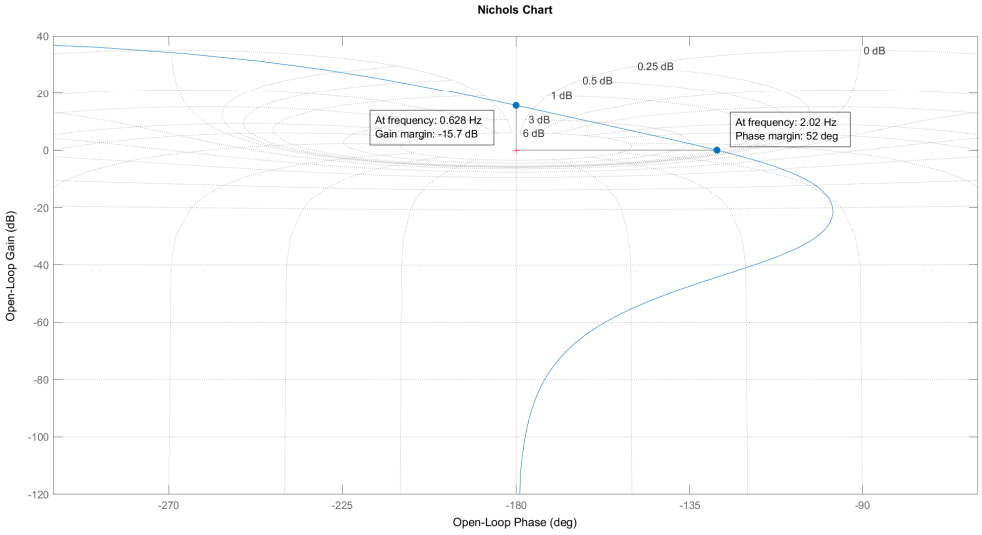

Figure 3.8: Nichols chart for the pitch and longitudinal position control loop, when opened at the input point to the plant

Due to the couplings that exist between the pitch/longitudinal translation loop and the roll/lateral translation loop, stability must also be studied in a MIMO sense.
This is done using multiloop disk margins, an analysis technique based on the structured singular value that can be used to quantify the largest complex perturbations that can be injected at the input point to the plant, simultaneously and independently in each channel. The perturbation takes the form of a disk in the complex plane (Fig. 3.9).

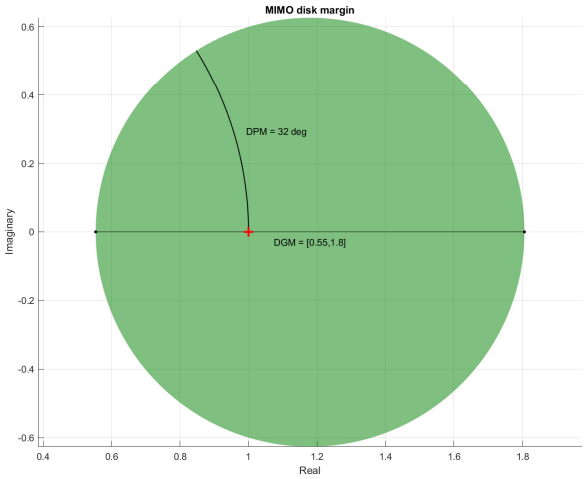

Figure 3.9: MIMO disk margins

The plot has been realized using MATLAB functions *diskmargin* and *diskmarginplot* and

it identifies gain margins of [0.55 1.8] and phase margins of [−32° 32°].
Once the linear control system has been tuned, in order to check the performance of the control law, simulations with the linear plant have been performed considering as reference states small step signals.

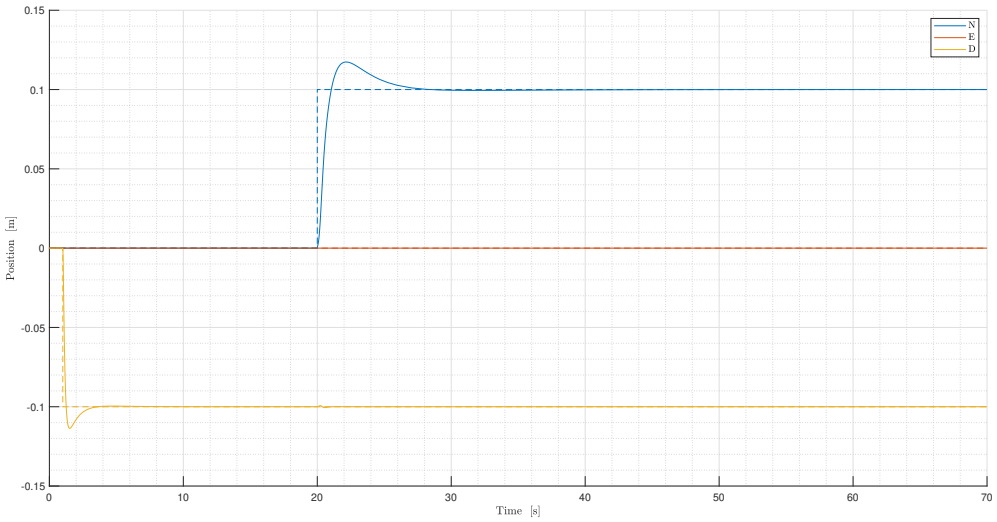

Figure 3.10: Time history of NED position (dashed lines are the desired values)

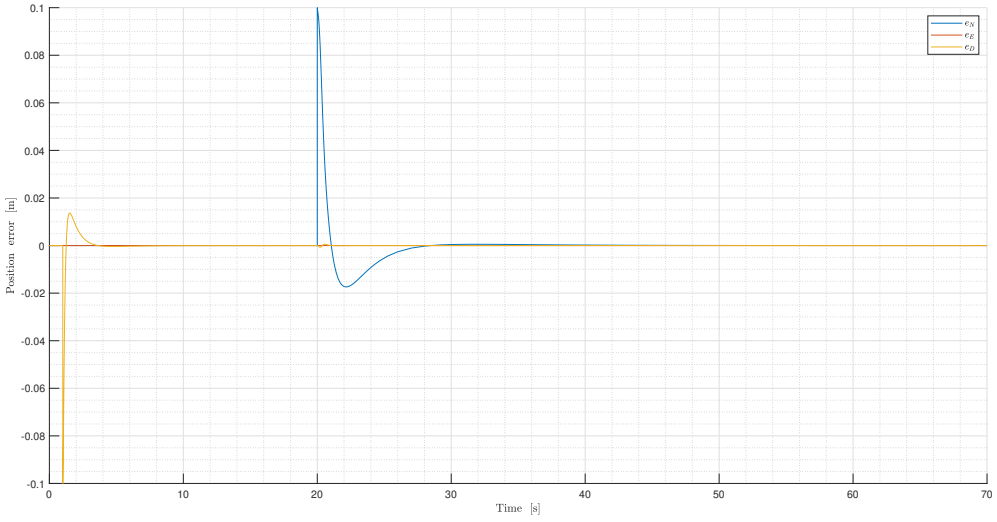

Figure 3.11: Tracking error of NED position

In Fig. 3.10, it is shown the response of the linear model on the x, y, z axes to a step of −0.1 m (with sample time of 1 s) on the desired heave and of 0.1 m (with sample time of 20 s) on the desired longitudinal position. The results are satisfactory, with small overshoots

and settling times, showing the good performances of the linear position controller when the system operates near hovering condition.
A similar simulation can be conducted in order to check the validity also of the linear attitude controller; in this case, the response of the system to a step of 0.1 rad on the desired yaw angle is studied.

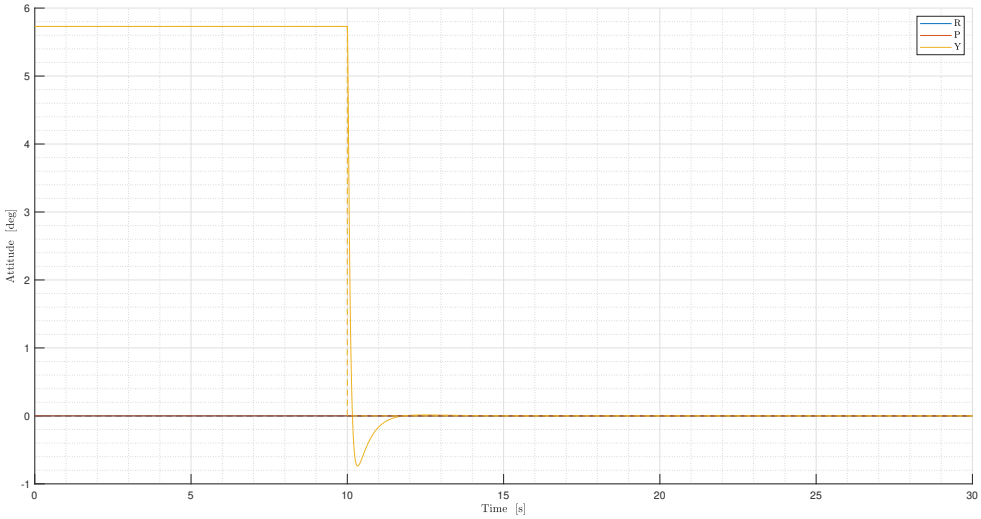

Figure 3.12: Time history of roll, pitch and yaw angles (dashed lines are the desired values)

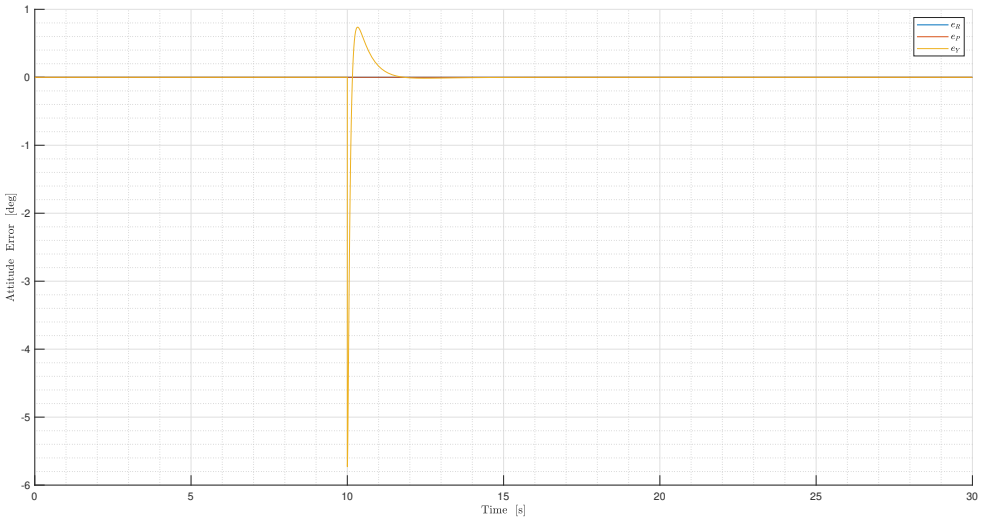

Figure 3.13: Tracking error of attitude

Looking at Fig. 3.12, we can do the same considerations carried out for the previous

simulation with a convergence of the yaw angle to zero in about 1.5 s. This result is consistent with the tuning since the required bandwidth for the system was of about 1.9 Hz.

3.1.3. Validation on the nonlinear plant

The designed control system is then paired with the nonlinear model described by Eq. 2.78.
The system is simulated under the same conditions of the previous linear case and considering the same reference states; this in order to check that the responses of the nonlinear model are the same of that linear near hovering point.

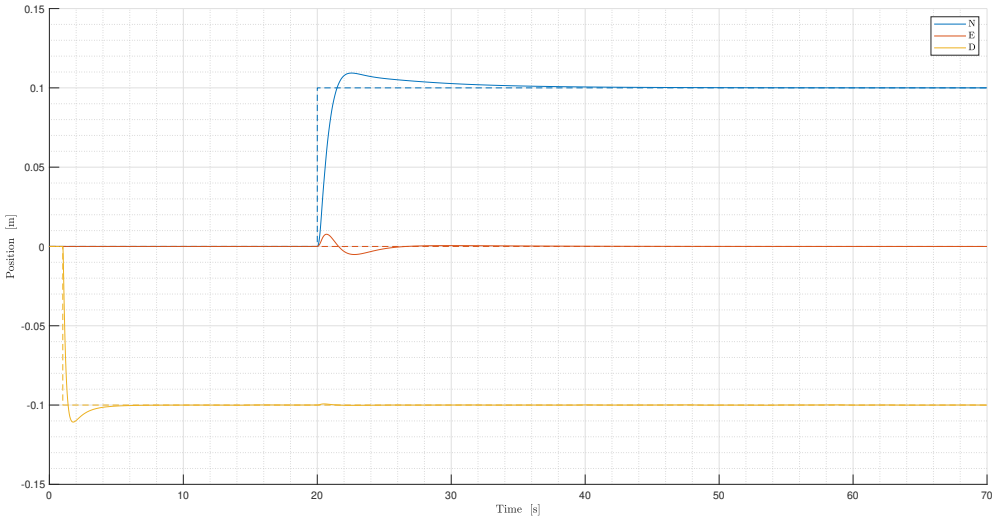

Figure 3.14: Time history of NED position (dashed lines are the desired values)

Fig. 3.14 is very similar to Fig. 3.10 with the only difference in slightly higher settling time on x axis and higher coupling between axis due to introduction of saturation; therefore, the results of this simulation confirms that the nonlinear model shows the same responses of the linear system in term of position when we operate near design condition.
The same considerations can be done in term of attitude control looking at Fig. 3.16; the response on yaw angle has the same time of convergence as in Fig. 3.12 but with a slightly higher overshoot and with some oscillations due to nonlinearites of the system and residual couplings between axis.

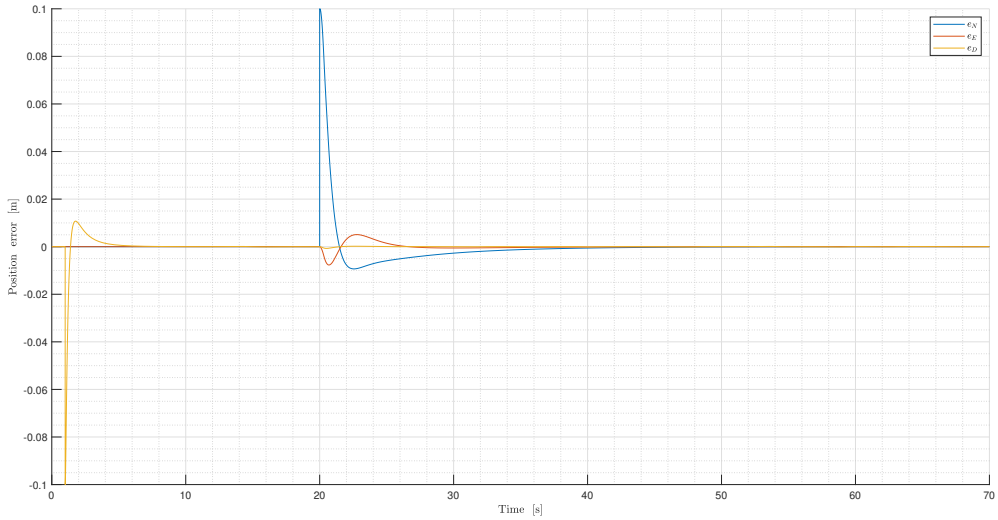

Figure 3.15: Tracking error of NED position

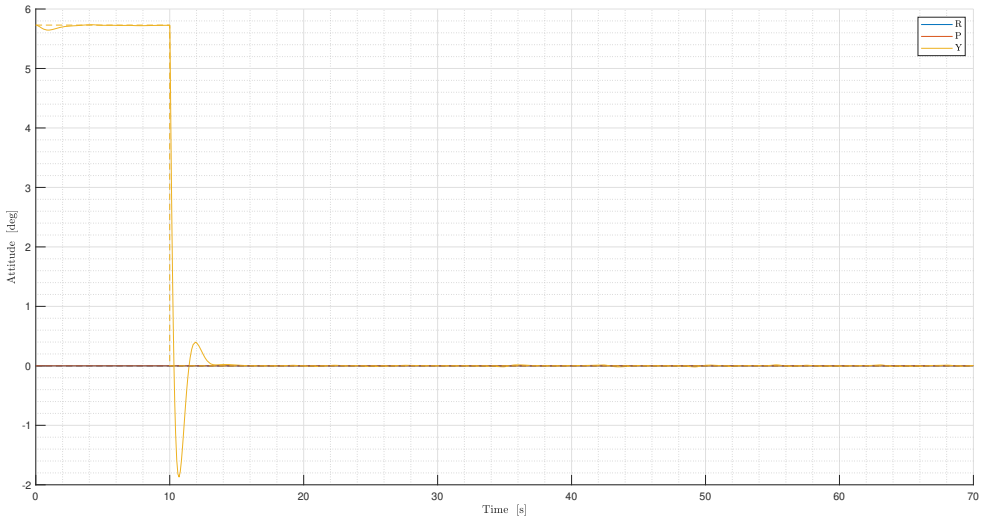

Figure 3.16: Time history of roll, pitch and yaw angles (dashed lines are the desired values)

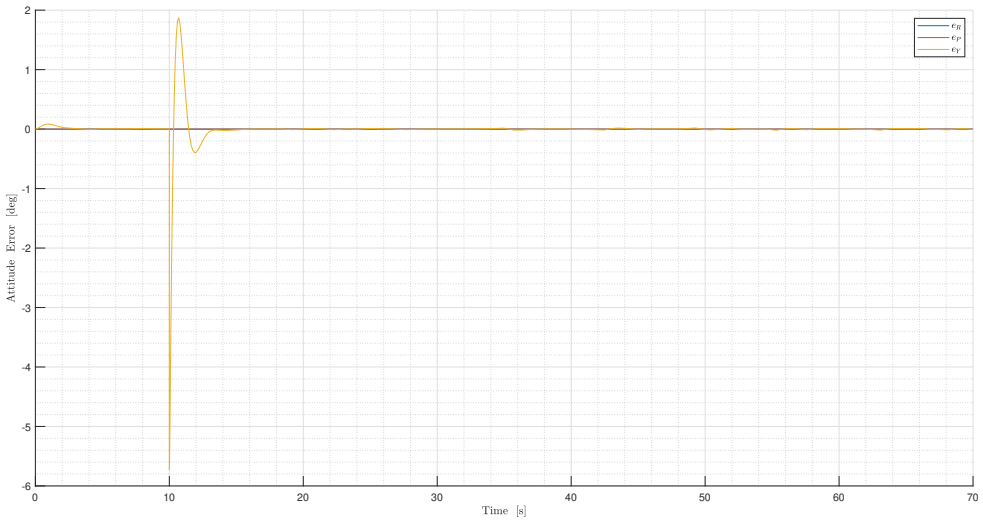

Figure 3.17: Tracking error of attitude

Then, the baseline controller has been tested far from the design condition considering great steps (2 m on x axis and −3 m on z axis). As illustrated in Fig. 3.19, the linear controller does not work well showing great overshoots and settling times. Moreover, as shown in Fig. 3.18, the control inputs are saturated at the point in which the step occurs (for Ingenuity the cyclic angles can range ±10° and the collective angles can range from −4.5° to 17.5°). These results confirm the bad behavior of the linear control law when the nonlinear system operates far from the hovering condition. To overcome this issues, it is necessary to implement a nonlinear controller.

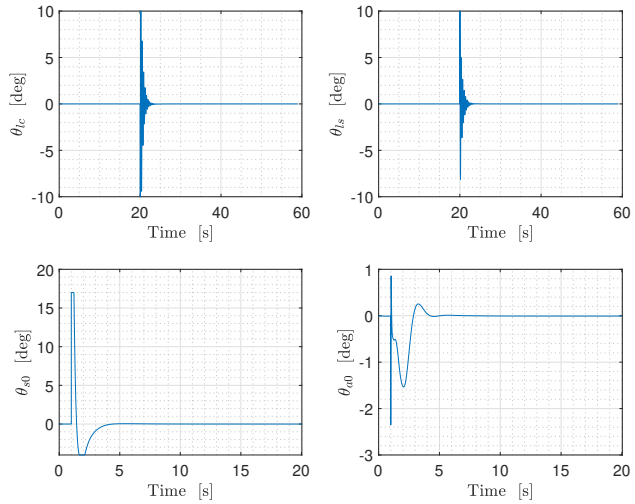

Figure 3.18: Time history of control inputs

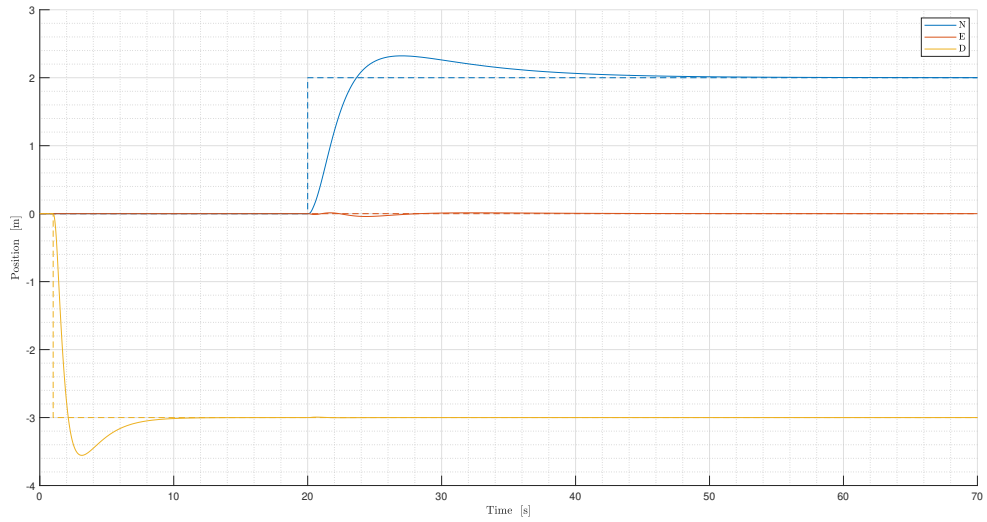

Figure 3.19: Time history of NED position (dashed lines are the desired values)

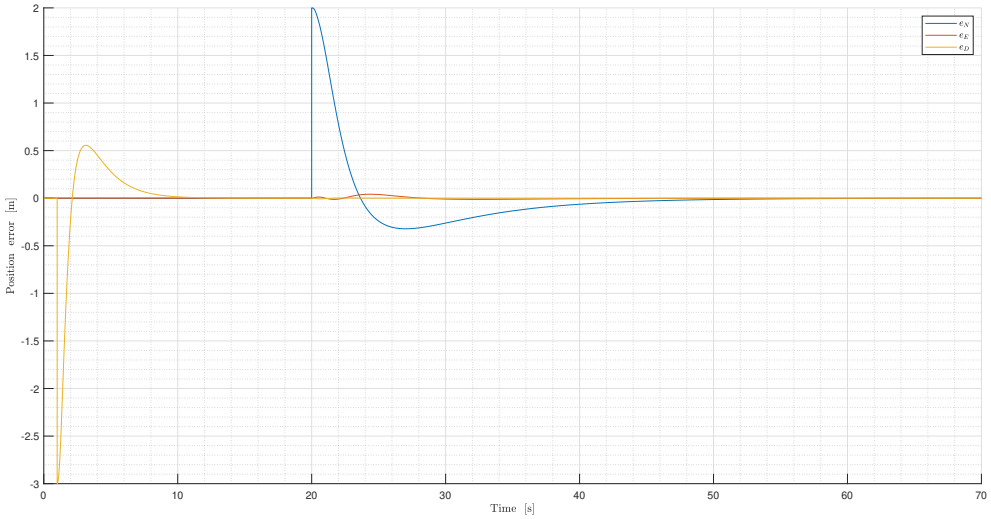

Figure 3.20: Tracking error of NED position

Another example of the bad behaviour of the linear control system far from the design point is shown in Fig. 3.21: it illustrates the longitudinal position response to a constant horizontal wind of magnitude 10 m/s (maximum horizontal wind at which the Mars Helicopter operates) applied throughout the simulation time, with a very great peak of approximately 0.78 m.

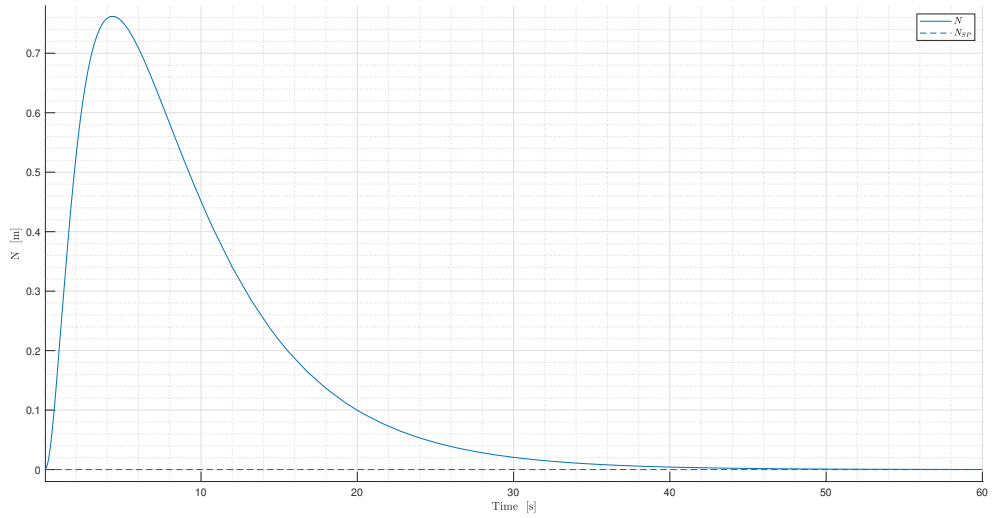

Figure 3.21: Step response of longitudinal position to a constant wind of magnitude 10 m/s along the x axis

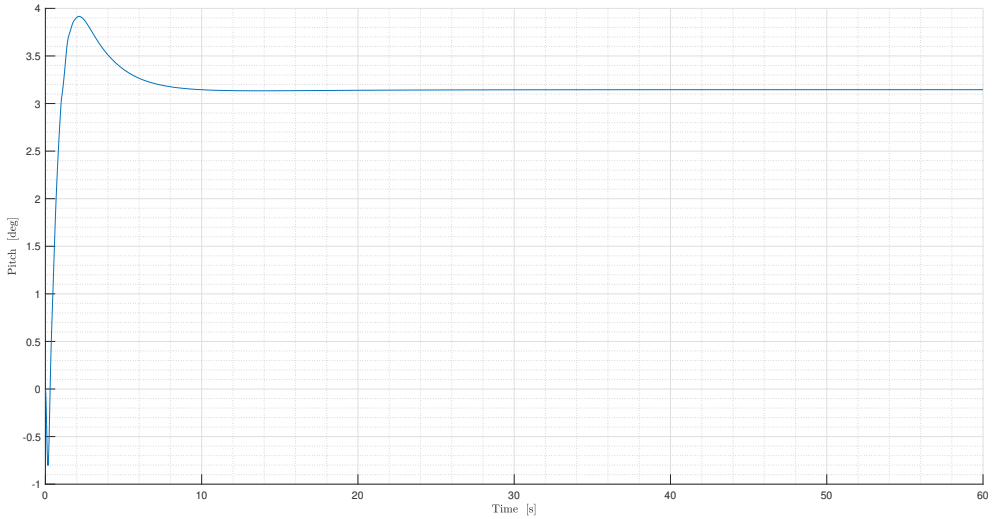

Figure 3.22: Pitch response to a constant wind of magnitude 10 m/s along the x axis

3.2. Nonlinear controller

In order to improve the results already obtained, a nonlinear control architecture is introduced.
The chosen control architecture shown in Fig. 3.23 consists of two nested parts. The outer position loop computes the total thrust to be generated by rotors and the roll and pitch angles required to get this thrust. The inner loop controls the attitude of the UAV using the moments generated by the propellers and the desired yaw and the computed roll and pitch as set-points instead.

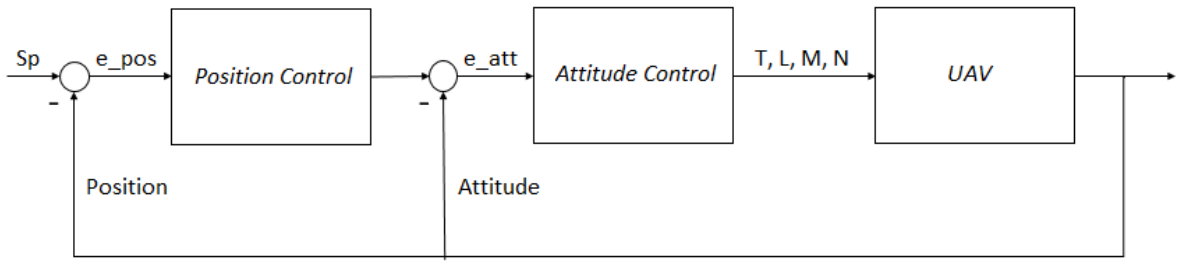

Figure 3.23: Control block diagram

3.2.1. Mathematical model

The starting point of the nonlinear control design is the building of an enlarged system that include also the dynamic of the rotation matrix $R \in SO(3)$, describing the attitude of UAV; the resulting system is represented in inertial frame with the centre of mass coincident with the origin of the body frame.
Recalling Eqs. 2.78 and 2.79, the position dynamics can be written as

$$\begin{aligned} \dot{x} &= v \\ m\dot{v} &= -mge_3 + T_{up}Rn_{up}(a_{up}, b_{up}) + T_{low}Rn_{low}(a_{low}, b_{low}) + f_e(x, v, ...) \end{aligned} \tag{3.9}$$

where

$$
\begin{aligned}
n_i &= \begin{bmatrix} -S_{a_i} C_{b_i} \\ S_{b_i} \\ -C_{a_i} C_{b_i} \end{bmatrix}, \quad \text{i} \in (\text{up, low}) \\
e_3 &= \begin{bmatrix} 0 \\ 0 \\ 1 \end{bmatrix} \\
f_e &= \text{aerodynamic drag and unmodelled exogenous terms}
\end{aligned}
\tag{3.10}
$$

and the attitude dynamics

$$
\begin{aligned}
\dot{R} &= R\hat{\omega} \\
J\dot{\omega} &= -\hat{\omega} J\omega + l_{low} e_3 \times T_{low} n_{low} + K_\beta \begin{bmatrix} b_{low} \\ a_{low} \\ 0 \end{bmatrix} + l_{up} e_3 \times T_{up} n_{up} \\
&\quad + K_\beta \begin{bmatrix} b_{up} \\ a_{up} \\ 0 \end{bmatrix} + (Q_{up} - Q_{low}) e_3 + \tau_e
\end{aligned}
\tag{3.11}
$$

where τ_e are the aerodynamics effects and unmodelled exogenous terms.
Including all terms treated as disturbances inside τ_e, the Eq. 3.11 can be rewritten as:

$$
\begin{aligned}
\dot{R} &= R\hat{\omega} \\
J\dot{\omega} &= -\hat{\omega} J\omega + l_{low} e_3 \times T_{low} n_{low} + K_\beta \begin{bmatrix} b_{low} \\ a_{low} \\ 0 \end{bmatrix} + (Q_{up} - Q_{low}) e_3 + \tau_e
\end{aligned}
\tag{3.12}
$$

If we consider a_{low} and b_{low} small enough, the expression of n_{low} can be rewritten as

$$
n_{low} \approx \begin{bmatrix} -a_{low} \\ b_{low} \\ 1 \end{bmatrix} \tag{3.13}
$$

leading to

$$
l_{low} e_3 \times T_{low} n_{low} \approx T_{low} l_{low} \begin{bmatrix} b_{low} \\ a_{low} \\ 0 \end{bmatrix} \tag{3.14}
$$

The total control torque components along roll and pitch axis are

$$\begin{aligned} L_c &= (T_{low} l_{low} + K_\beta) b_{low} \\ M_c &= (T_{low} l_{low} + K_\beta) a_{low} \end{aligned} \tag{3.15}$$

Assuming steady state conditions for the rotor dynamics and neglecting the influence of p, q (acceptable near hovering condition)

$$\begin{bmatrix} b_{low} \\ a_{low} \end{bmatrix} = M_{cyc}^{-1} \begin{bmatrix} \theta_{lc} \\ \theta_{ls} \end{bmatrix} \tag{3.16}$$

where M_{cyc} is the mixing matrix defined in Eq. 3.8.
In near hovering conditions, $T_{low} \approx T_{low,0}$ and we can write

$$\begin{bmatrix} L_c \\ M_c \end{bmatrix} = M_{cyc} \begin{bmatrix} \theta_{lc} \\ \theta_{ls} \end{bmatrix} \tag{3.17}$$

where

$$M_{cyc} = (T_{low,0} l_{low} + K_\beta) M_{cyc}^{-1} \tag{3.18}$$

M_{cyc} is invertible and L_c, M_c can be used to control roll and pitch axis motion.
The yaw torque is expressed as

$$N_c = Q_{up} - Q_{low} \tag{3.19}$$

and near hovering conditions is related to the asymmetric collective input as follow

$$N_c \approx \left| \frac{\partial}{\partial \theta_{a0}} (Q_{up} - Q_{low}) \right|_{x_0, u_0} \theta_{a0} \tag{3.20}$$

Going back to the position dynamics and substituting the previous assumptions in Eq. 3.9

$$m\dot{v} = -mge_3 + T_{up} R \left(\begin{bmatrix} -a_{up} \\ b_{up} \\ 0 \end{bmatrix} - e_3 \right) + T_{low} R \left(\begin{bmatrix} -a_{low} \\ b_{low} \\ 0 \end{bmatrix} - e_3 \right) + f_e \tag{3.21}$$

Remarking that cyclic inputs terms become disturbances for the position dynamics (input coupling effect), Eq. 3.21 becomes

$$m\dot{v} = -mge_3 + T_c R e_3 + \tilde{f}_e \tag{3.22}$$

where $\tilde{f}_e$ includes the terms related to a_{low}, b_{low}, a_{up} ... and $T_c = T_{up} + T_{low}$.
T_c can be written in approximate way as

$$T_c \approx \left| \frac{\partial}{\partial \theta_{s0}} \right|_{x_0, u_0} \theta_{s0} \tag{3.23}$$

The final model in inertial frame becomes

$$\begin{cases} \dot{x} = v \\ m\dot{v} = -mge_3 + T_c R e_3 + \tilde{f}_e \\ \dot{R} = R\hat{\omega} \\ J\dot{\omega} = -\hat{\omega} J\omega + \tau_c + \tau_e \end{cases} \tag{3.24}$$

with the allocation matrix

$$\begin{bmatrix} \theta_{s0} \\ \theta_{a0} \\ \theta_{lc} \\ \theta_{ls} \end{bmatrix} = \begin{pmatrix} M_{col}^{-1} & \\ & M_{cyc}^{-1} \end{pmatrix} \begin{bmatrix} T_c \\ L_c \\ M_c \\ N_c \end{bmatrix} \tag{3.25}$$

3.2.2. Control design

Considering Eq. 3.25, it is possible to use T_c and $\tau_c \in \mathbb{R}^3$ as variables for control design purposes, representing a desired control thrust and torque, respectively.
We can consider a nonlinear cascaded controller for position-yaw setpoint regulation; in particular, the control architecture corresponds to a double cascade P/PID nonlinear controllers for position and attitude control with a planner in the middle (see Fig. 3.24) [12]:

$$f_c^d = sat(PI_x(s)(k_{p,x}^0(x - x^d) - v)) + mge_3 \tag{3.26}$$

$$\begin{cases} T_c^d = ||f_c^d|| \\ R_p = \left[\frac{b_{p_3} \times b_{d_1}}{||b_{p_3} \times b_{d_1}||} \times b_{p_3} \quad \frac{b_{p_3} \times b_{d_1}}{||b_{p_3} \times b_{d_1}||} \quad b_{p_3} \right], \; b_{p_3} = \frac{f_c^d}{||f_c^d||} \end{cases} \tag{3.27}$$

$$\tau_c^d = PI_R(s)(\omega^d(K_{p,R}(R_p^T R) - \omega) - D_R(s)\omega \tag{3.28}$$

where

$$\begin{aligned} PI_{(.)}(s) &= K_{p,(.)}^i + k_{i,(.)}^i \frac{1}{s} \\ D_{(.)}(s) &= k_{d,(.)}^i N_{(.)}^i \frac{Ns}{s+N} \end{aligned} \tag{3.29}$$

are continuos functions defining, respectively, a proportional integral and (filtered) derivative actions, $k^{(.)}_{(.,.)} \in \mathbb{R}_{>0}$ are scalar gains while $K_{p,R} \in \mathbb{R}^{3x3}_{>0}$ is a diagonal matrix and $N^{(i)}_{(.)} \in \mathbb{R}_{>0}$ is the filter time constant; $x^d \in \mathbb{R}^3$ is the position setpoint; the rotation matrix $R_p \in SO(3)$ is the reference signal to be tracked by the attitude controller (Eq. 3.28) and corresponds to a reference frame having the third axis b_{p_3} aligned with the force required for position stabilization (f_c^d in Eq. 3.26) while the other two axes of the frame are assigned by a rotation about b_{p_3}, that accounts for a desired yaw angle ($\Psi^d \in \mathbb{R}$) through the unit vector $b_{d1} = \begin{bmatrix} cos(\Psi^d) & sin(\Psi^d) & 0 \end{bmatrix}^T$, which represents the desired (inertial) heading direction;

$$\omega^d(K_{p,R}R_p^T R) = 2K_{p,R}sgn(q_e(R_p))\mathbf{q}_e(R_p) \tag{3.30}$$

is a nonlinear proportional stabilizer assigning the reference velocity to the inner-loop attitude PID controller, with $q_e(R_p) \in \mathbb{R}$ and $\mathbf{q}_e(R_p) \in \mathbb{R}$ beeing the vectorial and the scalar part of the quaternion error $q_e \in \mathbb{S}^3$.

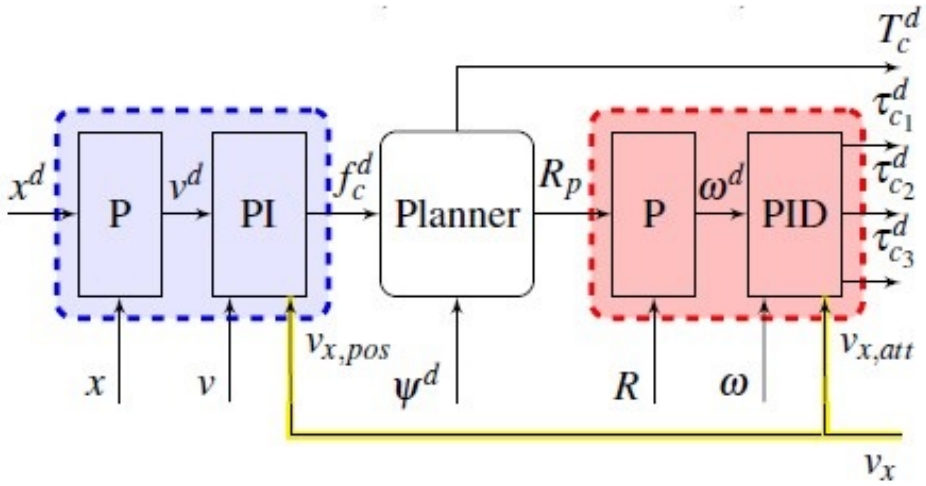

Figure 3.24: Controller implementation

For the position controller, a saturated PI has been implemented; this is necessary for two reasons: first, to simulate the limited capabilities of the rotors; second, to avoid singularity in the rotation matrix $R_p \in SO(3)$. Looking at Eqs. 3.26 and 3.27, singularity can be avoided imposing that the desired control thrust T_c^d must be always positive and lower than the gravitational force: this is achieved, in our case, limiting the output of PI_z in the range of $\pm\frac{mg}{2}$.

Nevertheless, the introduction of saturation may ruin the performance of the closed loop system, from degraded transients to instability when the system operates far from the hovering condition. This phenomena is called windup effect and it can be mitigated with

the implementation of a proper anti-windup technique. For our nonlinear controller, the *back calculation* method has been used which involves the use of extra feedback path from the error between the controller output u and the plant input $\hat{u} = sat(u)$ trough a gain $\frac{1}{\tau_t}$ (for PI controllers the back calculation constant is set as $\tau_t = \tau_i$; see Fig. 3.25) [8].

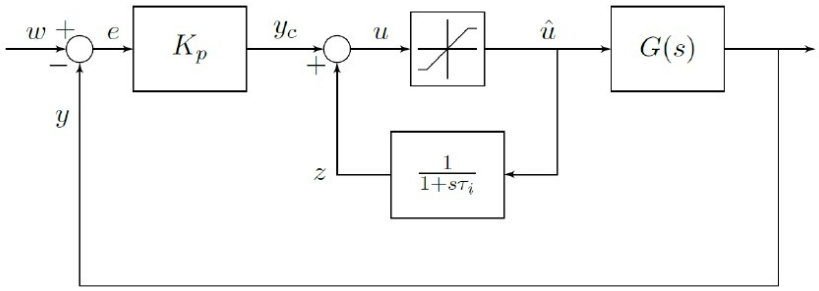

Figure 3.25: AW back calculation for a general PI controller

3.2.3. Tuning

The great advantage of the nonlinear control architecture presented in Subsection 3.2.2 is the capability to manage great displacements of the nonlinear system without limitations in the gains assigned to the controllers.

Even if there are not systematic tuning methods for nonlinear controllers, it is possible, for our case, to tune the controllers in order to follow local desired performances without losing global stability of the system. In this way, a linearized version of the control architecture was used to carry out tuning of the gains. This allows to resort to the systematic tuning method used for baseline controller (Subsection 3.1.2). Therefore, the controllers have been tuned in order to achieve the same performance requirements identified for the baseline.

As for the linear control system, if the inner loop for both position and attitude control is fast enough, it is possible to choice arbitrarily gains for the outer loop; this because the inner loop becomes like an identity capable to follow any reference within a certain bandwidth. For the proportional controllers of position, the gains have been imposed equal to the crossover frequencies of the outer horizontal position loop and heave loop of baseline control architecture (0.3 Hz and 1.2 Hz, respectively); for the proportional controllers of attitude, the gains have been imposed equal to the crossover frequencies of the inner roll/pitch loop and yaw loop of baseline control architecture (2.6 Hz and 1.9 Hz, respectively). The inner loop PID controllers have been tuned on the linearized dynamics system in order to be at least two times faster than the respectively outer loop P controllers.

4 | Vehicle simulation

In this chapter the simulated results obtained using the previously developed nonlinear control architecture is presented.
A first introduction to the SIMULINK simulator built is provided at the beginning. Then the nonlinear control law is tested first near hovering condition (carrying out the same simulations done in Subsection 3.1.2) and later, it is tested far from the design point in order to study the responses of the system to great signals.

4.1. UAV simulator

The main block of the simulator is of course the Mars helicopter model. It is based on the equations in Subsection 2.7 plus some additions that can be seen in Fig. 4.2. The position in output is expressed in inertial frame and the attitude in form of quaternions. The yellow block in Fig. 4.1 contains the implemented nonlinear control architecture described in Section 3.2 that computes the required thrust and moments in order to follow the desired trajectory generated by *set point generator* function. Before entering the *Ingenuity* block, the control signals are sent to the mixer described by Eqs. 3.5 and 3.7 giving in output the collective and cyclic controls.

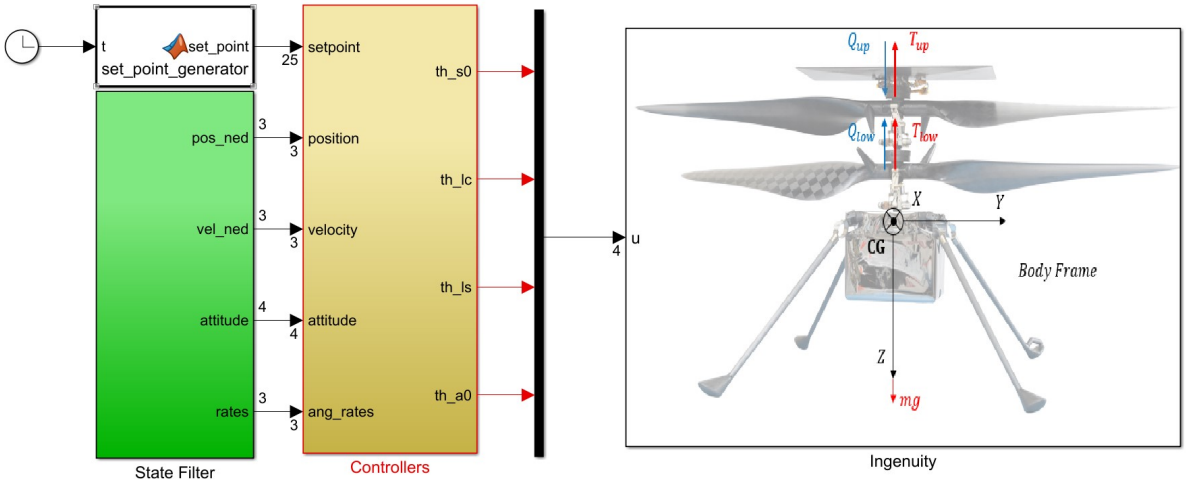

Figure 4.1: UAV simulator implemented in SIMULINK

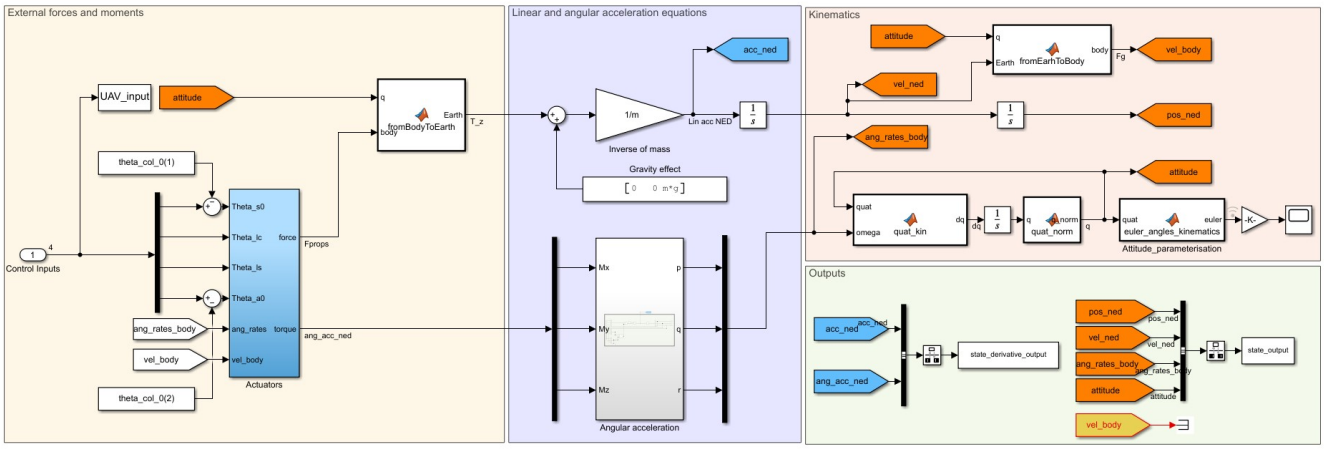

Figure 4.2: Simulator of the UAV dynamics

4.2. Simulations near hovering point

The system is simulated around hovering conditions considering as reference states the same small step signals implemented at the end of Subsection 3.1.2.
In order to test the position control law, a step of -0.1 m (with sample time of 1 s) on the desired heave and of 0.1 m (with sample time of 20 s) on the desired longitudinal position has been considered. The results are illustrated in Fig. 4.3 showing a behaviour similar to that of linear case but with smaller overshoots and settling times validating the good performances of the nonlinear control architecture implemented. Moreover, the axis appear completely decoupled.
The attitude control law has been tested in the same way considering a step of 0.1 rad on the desired yaw angle. Also in this case, the response is very clean and fast with a time of convergence to the desired value less than 1 s and a null overshoot (see Fig. 4.5).

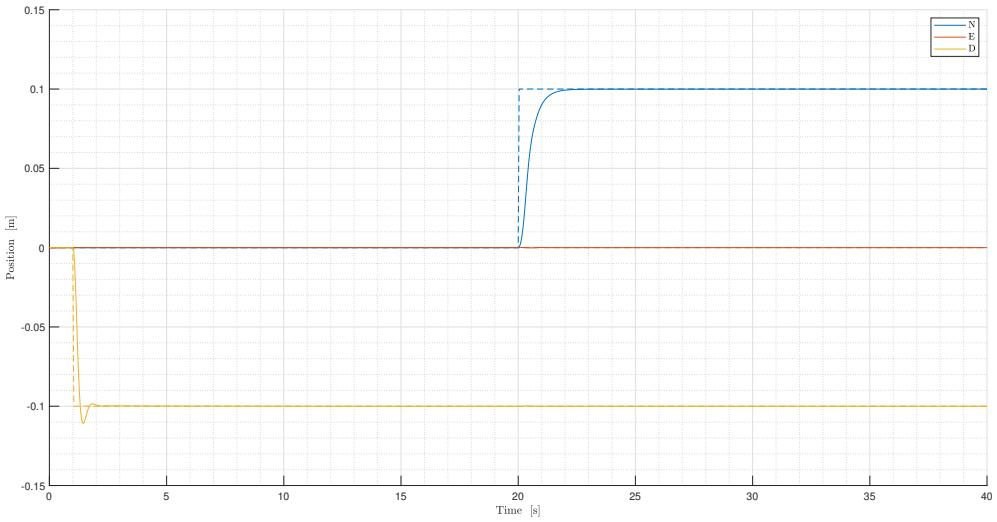

Figure 4.3: Time history of NED position (dashed lines are the desired values)

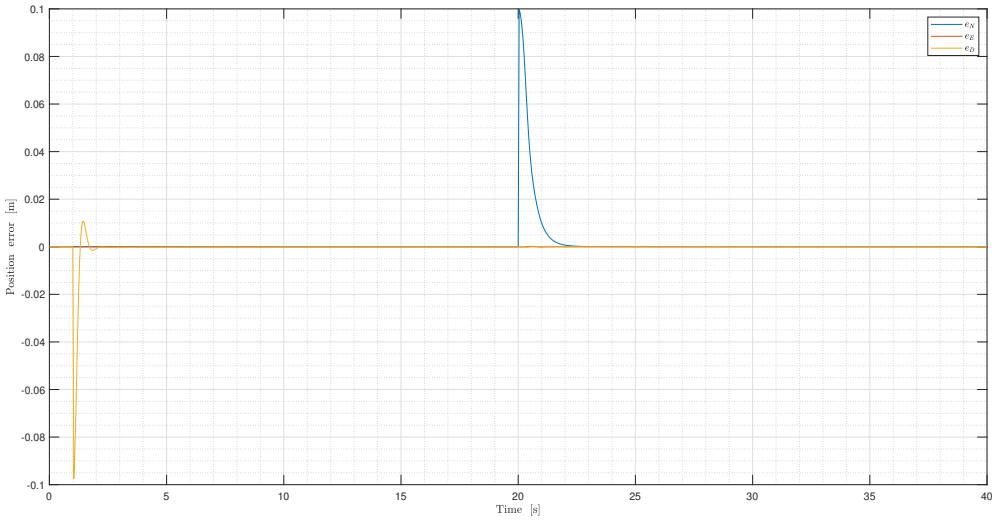

Figure 4.4: Tracking error of NED position

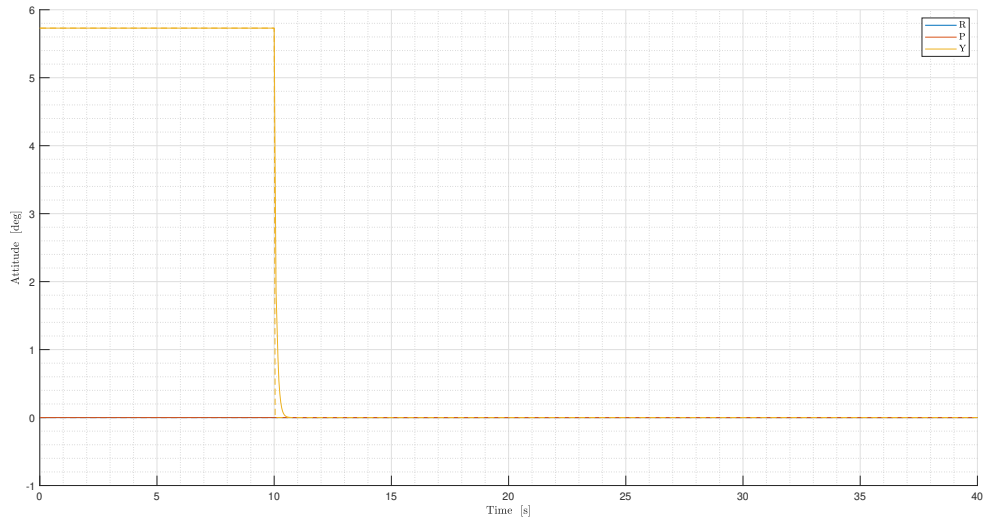

Figure 4.5: Time history of roll, pitch and yaw angle (dashed lines are the desired values)

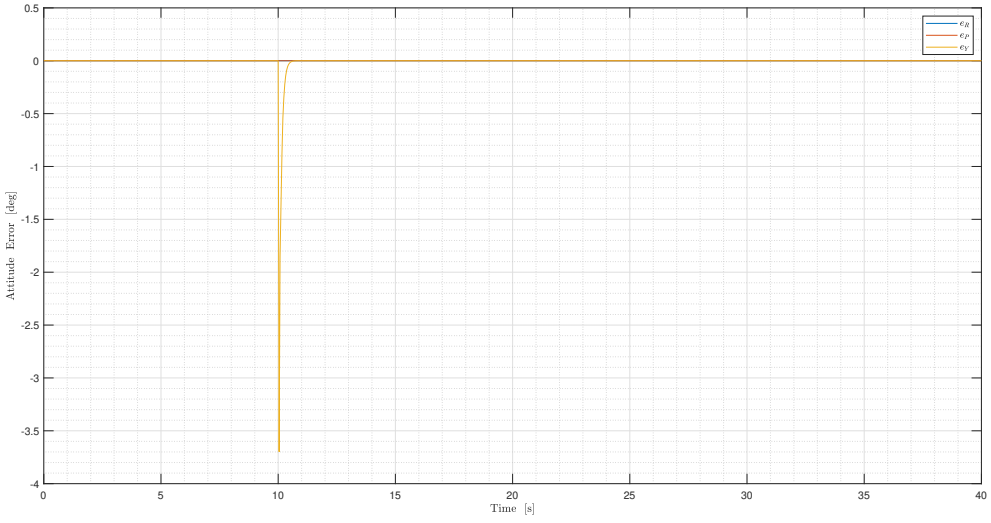

Figure 4.6: Tracking error of attitude

4.3. Simulations out of design conditions

Once verified that the nonlinear control system implemented works as expected near equilibrium point, simulations far from hovering condition have been carried out.
A first simulation has been done considering a step of 2 m on the desired longitudinal position and a smooth step of -3 m on the desired heave in order to achieve a high altitude not too aggressively.

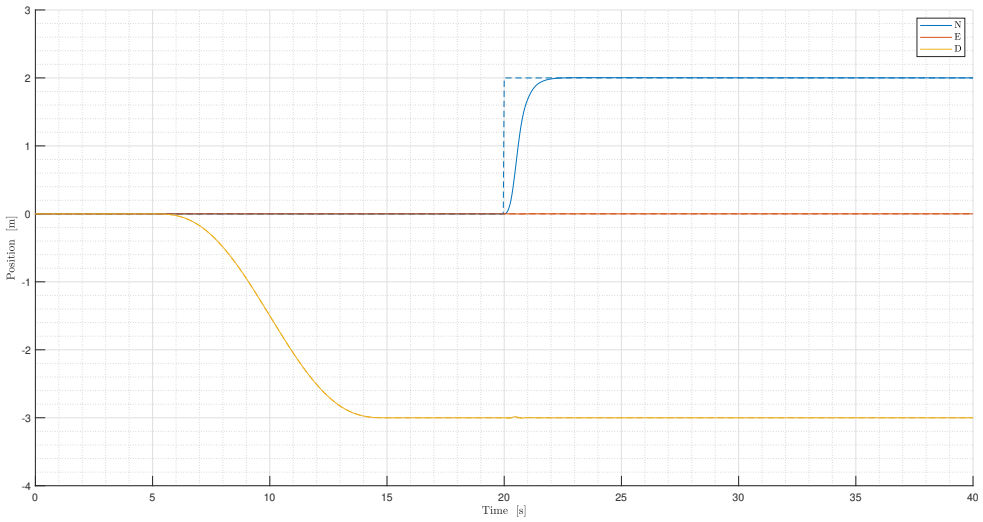

Figure 4.7: Time history of NED position (dashed lines are the desired values)

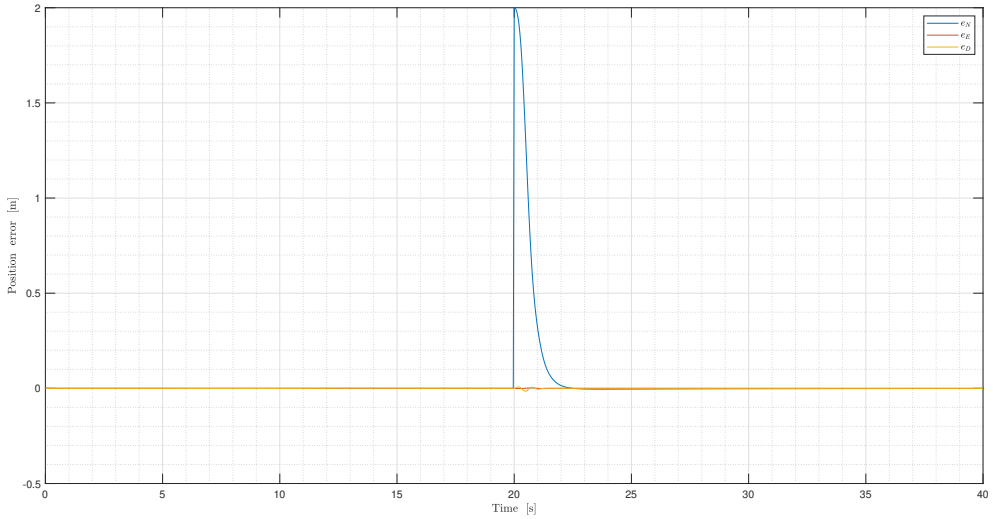

Figure 4.8: Tracking error of NED position

As illustrated in Fig. 4.7, the system responses very well also out of design condition showing the same local desired performances and stability. Moreover, even if the rotors reach saturation, the longitudinal position response follows well the desired trajectory validating the good performances of the anti-windup system implemented.
A second simulation is carried out in order to show the difference between the linear baseline controller and the nonlinear controller when a constant horizontal wind of magnitude 10 m/s is applied throughout the simulation time; in Fig. 4.9, the longitudinal position response reaches a peak of only 0.033 m, much smaller than the peak of 0.78 m shown in Fig. 3.21. This result ensures the stability of the system developed in presence of external perturbations.

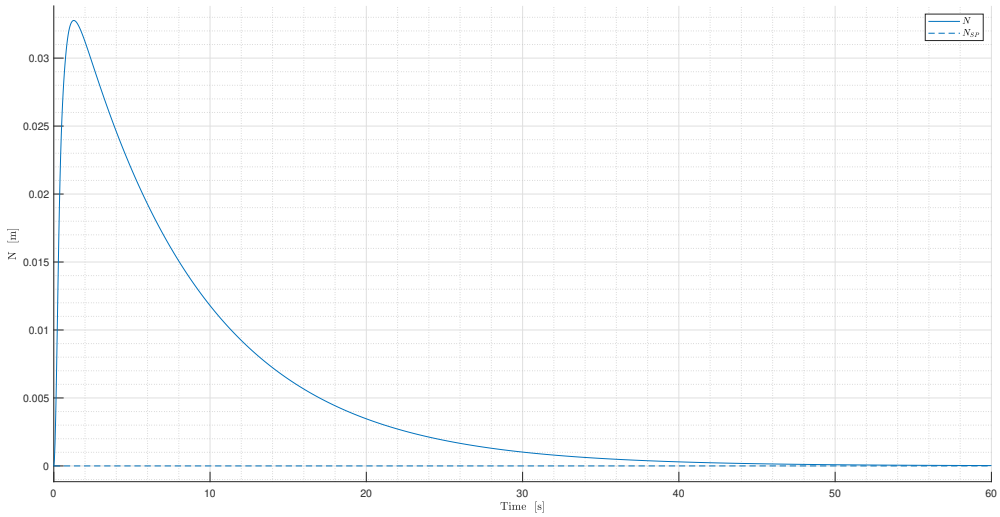

Figure 4.9: Step response of longitudinal position to a constant wind of magnitude 10 m/s along the x axis

The simulation in Fig. 4.12 replicates a flight test performed by Ingenuity inside the JPL 25-ft Space Simulator; the system stays on the ground for about 20 s before reaching the desired altitude of 3 m at a rate of 1 m/s. Then, it stays in hover for 30 s before going back to the ground with the same rate of ascent. As shown in Fig. 4.13, the error is very small (in the order of 10^{-3} m during climb and descent phases). The test has been carried out in absence of wind.

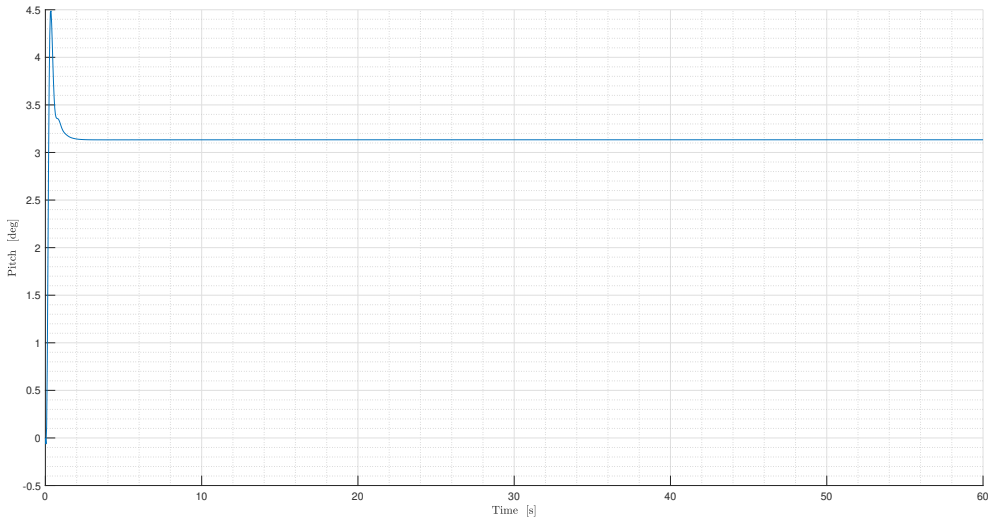

Figure 4.10: Pitch response to a constant wind of magnitude 10 m/s along the x axis

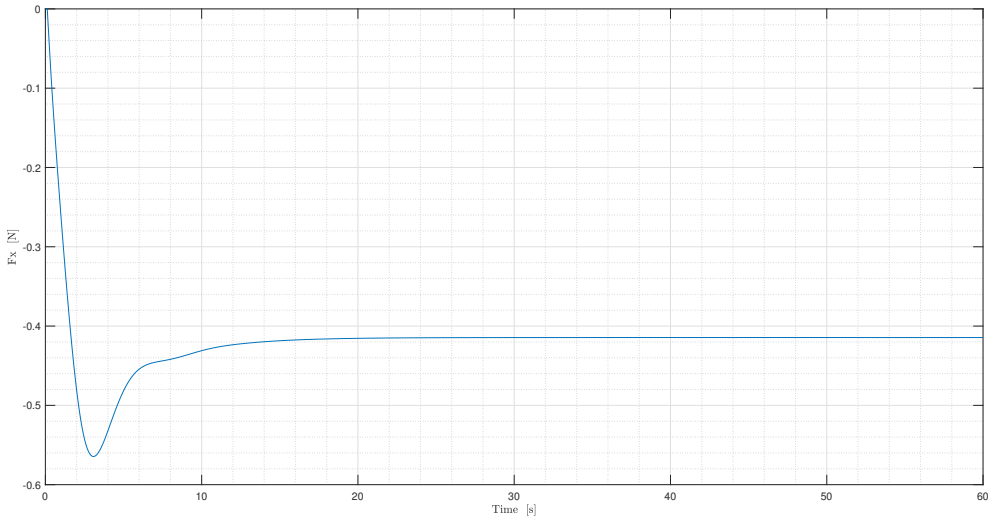

Figure 4.11: Force to be applied along x axis in order to compensate the presence of wind

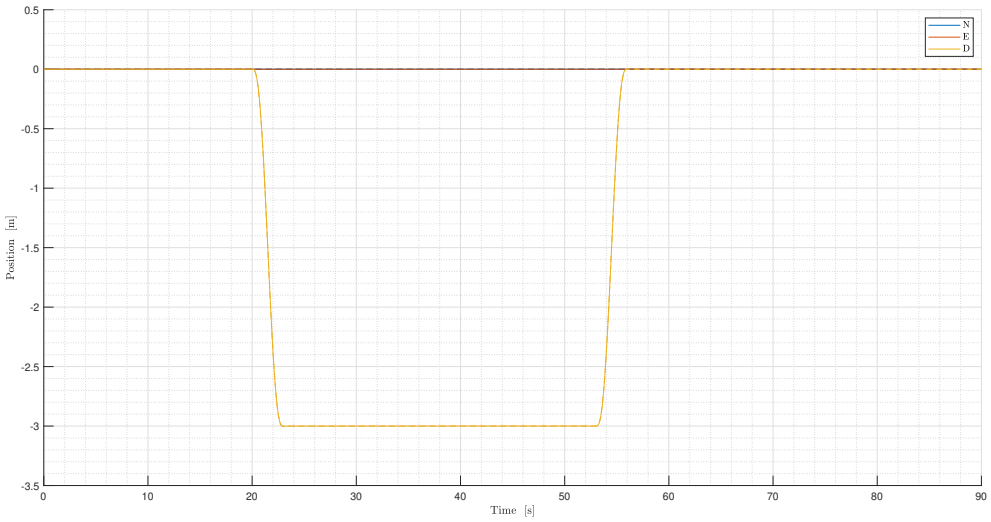

Figure 4.12: Time history of NED position during climb and descent operation

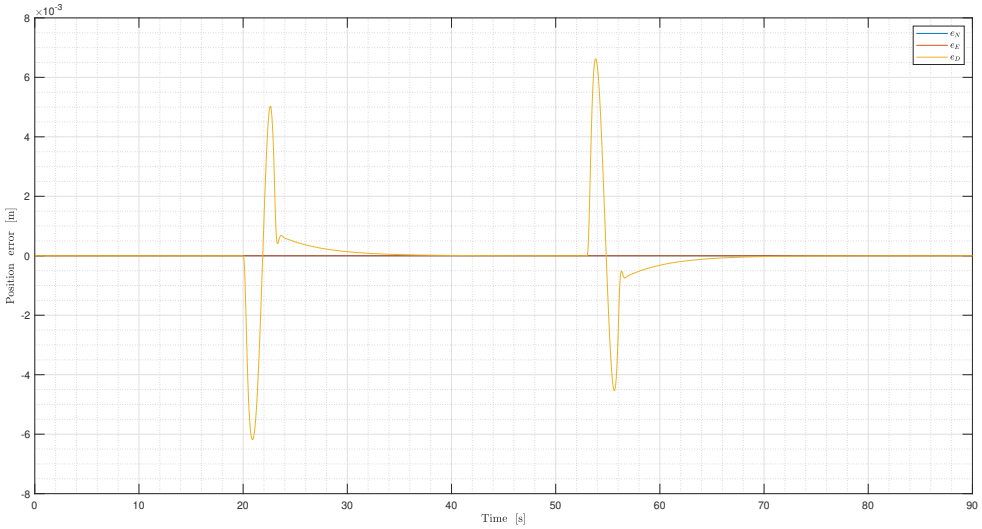

Figure 4.13: Tracking error of NED position during climb and descent operation

A final simulation has been run in order to reproduce a typical Ingenuity's operation on Mars similar to the one illustrated in Fig. 1.13. The UAV after 5 s on the ground reaches the altitude of 3 m at a rate of 1 m/s. At constant height, the system translates laterally until it reaches the cartesian coordinates $(0, 20, 3)$ m. Then, it moves along longitudinal axis for 10 m before going back to initial point following the same specular flight path. The operation takes 90 s, maximum flight time in which the batteries provide energy. Longitudinal and lateral translations occur at the same rate of ascent (1 m/s), velocity needed to take clear images of the ground.
In Fig. 4.16, a 3D representation of the trajectory followed by the Mars helicopter is plotted in cartesian coordinates. The red point indicates the initial and final position of the UAV and the arrows specify the direction of the path.

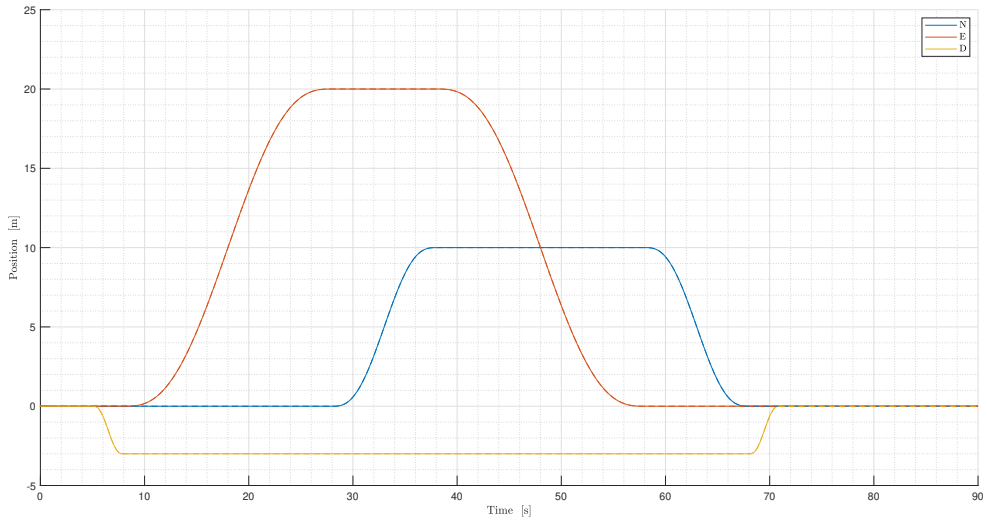

Figure 4.14: Time history of NED position during Mars operation

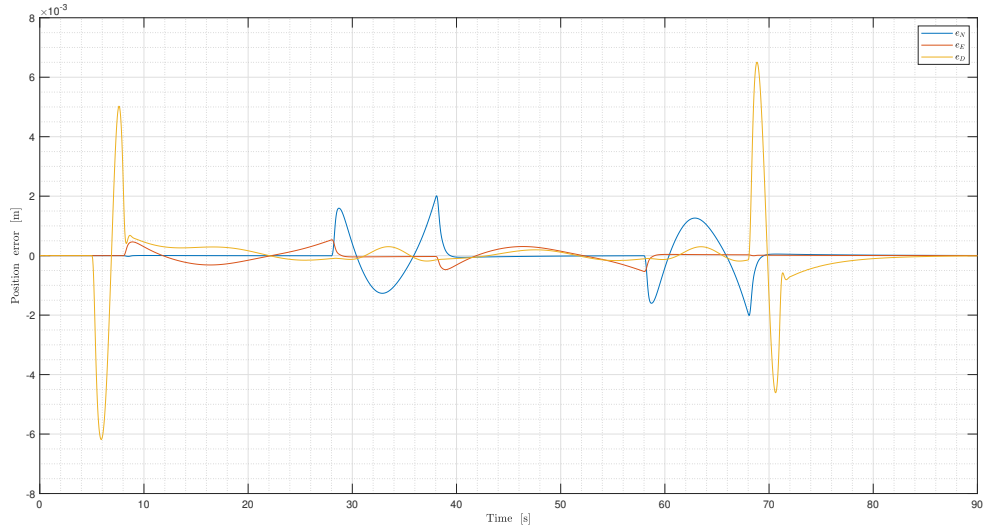

Figure 4.15: Tracking error of NED position during Mars operation

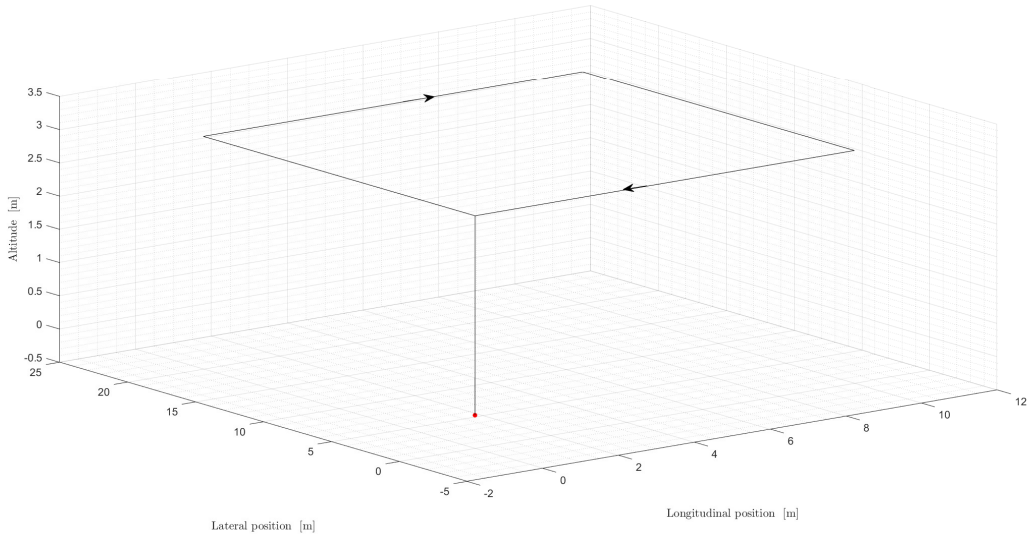

Figure 4.16: 3D plot of the flight path followed by the helicopter

The previous test has been carried out also in the presence of a three-second horizontal gust of magnitude 10 m/s applied at time $t = 42$ s. The results, illustrated in Figs. 4.17 and 4.18, show a small peak of displacement along the x axis due to wind, validating the robustness of the designed nonlinear control law even in the presence of external disturbances.

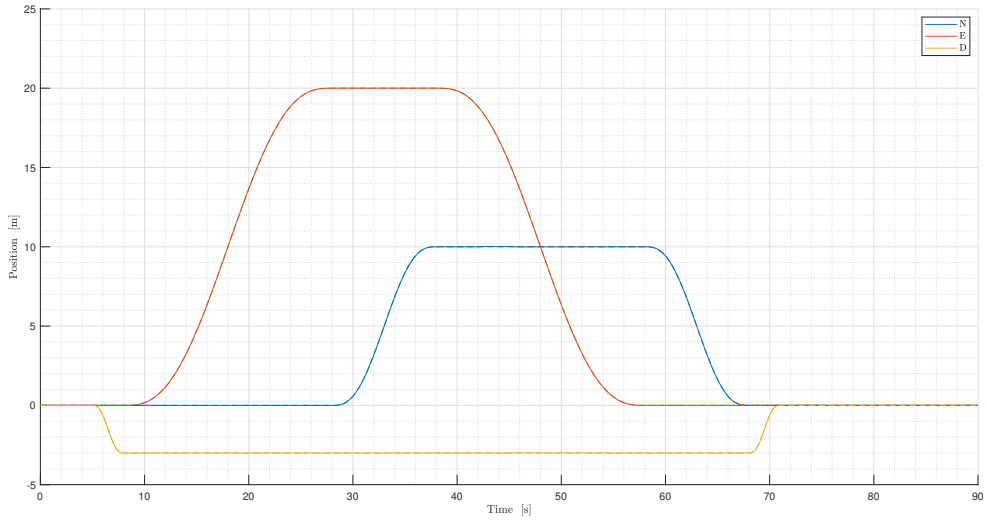

Figure 4.17: Time history of NED position during Mars operation in presence of a horizontal gust

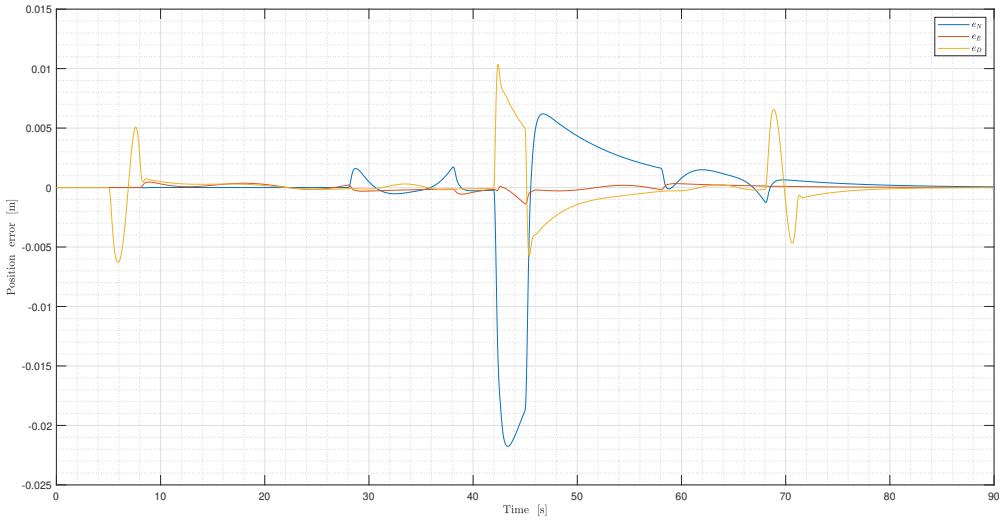

Figure 4.18: Tracking error of NED position during Mars operation in presence of a horizontal gust

In order to highlight the differences between the nonlinear controller and the baseline controller, the same previous maneuver has been carried out using the linear controller. The results are shown in Figs. 4.19 and 4.20.

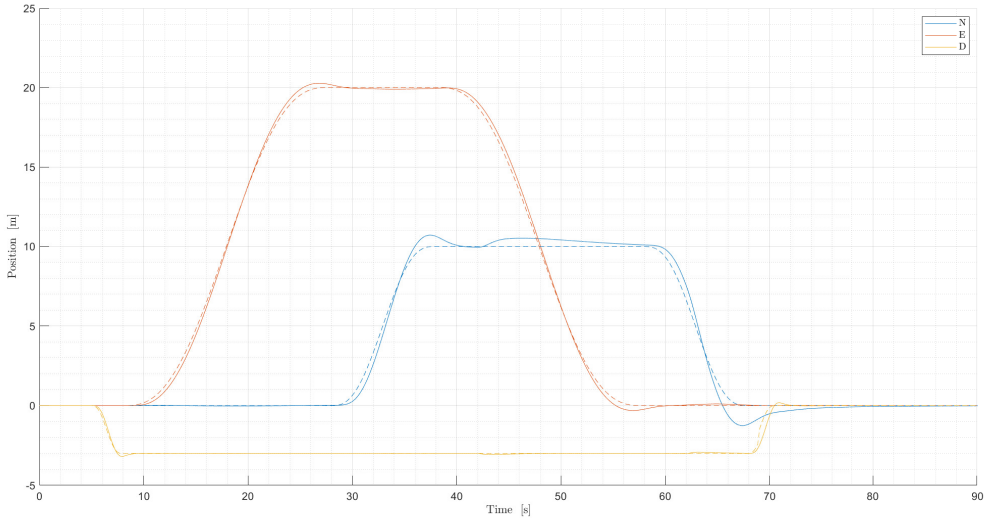

Figure 4.19: Time history of NED position during Mars operation in presence of a horizontal gust and using the linear controller

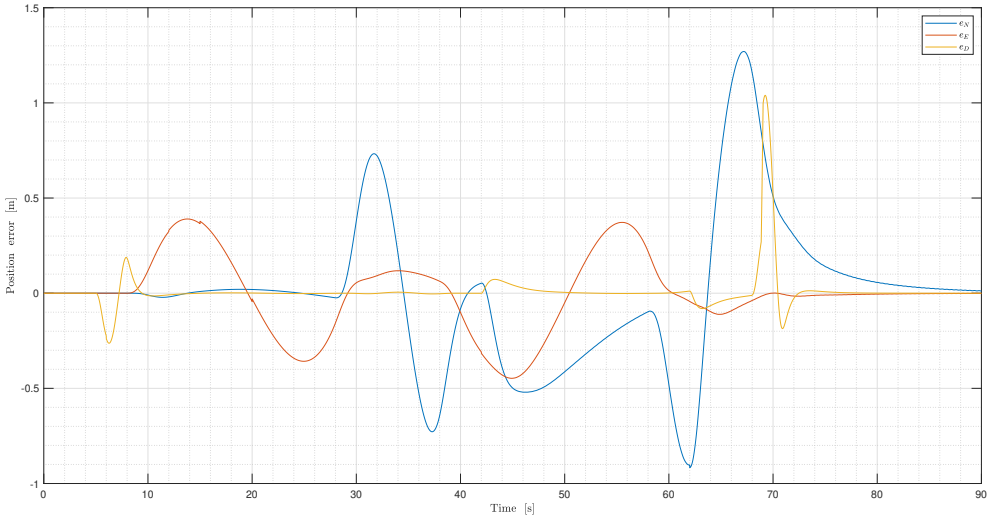

Figure 4.20: Tracking error of NED position during Mars operation in presence of a horizontal gust using the linear controller

5 | Conclusions

In the presented thesis, a nonlinear dynamic model of the Mars helicopter has been derived for simulation purposes and for the preliminary validation of nonlinear control laws. While simple, the parameters of the nonlinear model could be tuned to achieve a behavior very similar to the demonstrator vehicle of the Mars Helicopter in near hovering conditions, by exploiting identification experiments reported in the literature. The analysis and the open loop simulations conducted have tested the correct working of our model showing a similar behavior to the that of Ingenuity demonstrator.
In the second part of the thesis, the control system has been developed starting with the implementation of a linear controller obtained by replicating the architecture proposed in literature for Ingenuity and following with the development of the proposed nonlinear controller based on additional simplifications of the nonlinear model. Both controllers have been tuned properly checking their performances through linear stability analysis as Nichols charts and MIMO disk margins.
The numerical simulations carried out have shown good results of the baseline controller when the system operates near hovering condition, but deteriorated performance far from it. The implementation of a nonlinear control law has improved the system performance far from hovering and has made the UAV capable of following more complex trajectories.
As future work, a more accurate model of the Mars Helicopter could be developed including the higher-order terms discarded in the rotor dynamics and incorporating a detailed inflow evaluation for both rotors taking in account a radial distribution of the blade pitch angle and of the inflow.
The control system developed could be tested for aggressive maneuvers verifying its stability and robustness under these conditions. The cyclic control could be applied also on the upper rotor, as in the real system, leading to a improvement of control authority and to a reduction of cross-axis coupling. Moreover, a comparison between results obtained with the proposed nonlinear controller and with other nonlinear control laws could be carried out in order to select the most suitable controller for our model.

Bibliography

[1] D. B. A.R.S. Bramwell, G. Done. *Bramwell's Helicopter Dynamic, 2nd edition*. Butterworth-Heinemann, Oxford, 2001.

[2] B. Balaram, T. Canham, C. Duncan, H. F. Grip, W. Johnson, J. Maki, A. Quon, R. Stern, and D. Zhu. Mars helicopter technology demonstrator. In *2018 AIAA Atmospheric Flight Mechanics Conference*, page 0023, 2018.

[3] B.Mettler. *Identification Modeling and Characteristics of Miniature Rotocraft*. Kluwer, Norwell, 2002.

[4] B. M. C. Fei Wang, Jinqiang Cui and T. H. Lee. Flight Dynamics Modeling of Coaxial Rotorcraft UAVs. *Handbook of Unmanned Aerial Vehicles*, pages 1217–1256, 2015.

[5] H. F. Grip, D. P. Scharf, C. Malpica, W. Johnson, M. Mandic, G. Singh, and L. A. Young. Guidance and control for a mars helicopter. In *2018 AIAA Guidance, Navigation, and Control Conference*, page 1849, 2018.

[6] W. M. C. S. D. M. M. Y. L. A. B. M. B. S. M. M. Grip, H.F.; Johnson and J. Lam. Modeling and Identification of Hover Flight Dynamics for NASA's Mars Helicopter. *Journal of Guidance, Control, and Dynamics, Volume 43, Number 2*, February 2020.

[7] M. S. J. Gordon Leishman. Figure of Merit Definition for Coaxial Rotors. *Alfred Gessow Rotorcraft Center, Department of Aerospace Engineering Glenn L. Martin Institute of Technology University of Maryland, College Park, MD*, July 2008.

[8] H. K. Khalil and L. Praly. High-gain observers in nonlinear feedback control. *International Journal of Robust and Nonlinear Control*, 24(6):993–1015, 2014.

[9] A. Koehl, H. Rafaralahy, M. Boutayeb, and B. Martinez. Aerodynamic modelling and experimental identification of a coaxial-rotor uav. *Journal of Intelligent & Robotic Systems*, 68(1):53–68, 2012.

[10] J. W. Koning, W. J. F. and B. G. Allan. Generation of Mars Helicopter Rotor Model for Comprehensive Analyses. *Proceedings of the American Helicopter Society*

Technical Conference on Aeromechanics Design for Transformative Vertical Flight, 2018.

[11] G. J. Leishman. *Principles of helicopter aerodynamics*. Cambridge university press, 2006.

[12] G. Marzagalli, Ghignoni and Invernizzi. Experimental validation of an anti-windup design trading off position and heading direction control performance for quadrotor uavs.

[13] E. Roussel, V. Gassmann, and E. Laroche. Accuracy–simplicity trade-off for small-scale helicopter models: A comparative study based on flight data. *Control Engineering Practice*, 73:56–65, 2018.

List of Figures

List of Tables

Acknowledgements

Vorrei ringraziare, innanzitutto, il mio relatore Davide per avermi sempre aiutato ed essere sempre stato disponibile in questi mesi; sono davvero contento di aver avuto una persona come lui a guidarmi nella stesura della tesi.
Un secondo sincero e sconfinato ringraziamento va a tutti i miei amici, che non starò qui a citare uno ad uno perché siete troppi, ma sappiate che vi voglio bene e che ognuno di voi occupa un posto speciale e unico nel mio cuore: chi è il mio fuoco, chi è la mia acqua, chi è il mio vento e chi è la mia terra, siete tutti elementi fondamentali della mia vita ed è sicuramente grazie al vostro sostegno, ai momenti spensierati passati assieme, alle discussioni esistenziali partorite alle due di notte che sono qui ora, più maturo di quello che ero anni fa e pronto ad affrontare ciò che mi riserba il futuro, il quale spero di vivere al vostro fianco.
Un ringraziamento speciale va ai miei compagni di università, che già annovero tra i miei amici, ma che vorrei ringraziare in particolare per avermi aiutato negli anni tra progetti ed esami e per aver condiviso con me quel cammino tortuoso, pieno di insidie e privo di grosse soddisfazioni, che è stato studiare al Politecnico.
Il ringraziamento più grande va alla mia famiglia. In particolare, ai miei genitori, che mi hanno nutrito e curato trasformando un seme acerbo in un fiore: se è difficile dare al mondo una nuova vita, lo è ancora di più prendersene cura e aiutarla a sbocciare; so che a volte do per scontato tutto ciò che fate per me e l'amore che mi date, ma d'altronde un fiore è veramente consapevole del nutrimento che, giorno dopo giorno, la terra gli dà? Io penso di no, ma spero in futuro di poter diventare io stesso terra per potermi prendere cura di voi, rinnovati fiori, e ripagarvi di tutto quanto.
Un ringraziamento va anche ai miei nonni che, come i miei genitori, si sono sempre presi cura di me senza riserve, viziandomi e riempiendomi di tutto l'amore possibile. Non dimenticherò mai i momenti passati assieme, le espressioni dialettali trasmessomi, come la celebre "*Magnà magnòccom, l'è a lavorà che barbòttom!*", e tutti gli aneddoti da voi raccontati e che sono stati fonti di grandi insegnamenti. Tutti dovrebbero avere dei nonni come voi.
Un caloroso ringraziamento a mio fratello e ai miei cugini, da sempre compagni di crescita

e d'avventura: quante vacanze e quanti giochi che abbiamo fatto insieme, dimenticandosi dello scorrere del tempo e volando sulle ali della fantasia verso mondi immaginari bellissimi e in cui sentirsi come a casa, d'inverno, davanti al camino acceso e a una cioccolata calda. Infine, vorrei ringraziare le stelle, che ricerco sempre nelle notti estive e che contemplo a lungo immaginandomi come possa essere la vita là fuori, oltre la sottile atmosfera che circonda il nostro pianeta. Vi prometto stelle, che un giorno vi raggiungerò e danzeremo insieme nell' infinità del tutto, ma, per ora, siate la mia umile guida nelle notti più buie.